ASTRONOMY & ASTROPHYSICS
SUPPLEMENT SERIES

NOVEMBER II 1991, PAGE 61

Astron. Astrophys. Suppl. Ser. **91**, 61-128 (1991)

A study of southern extreme IRAS galaxies.
I. Optical observations *

A.C. van den Broek[1], W. van Driel[1], T. de Jong[1], J. Lub[2], M.H.K. de Grijp[2] and P. Goudfrooij[1]

[1] Astronomical Institute "Anton Pannekoek", University of Amsterdam, Kruislaan 403, NL-1098 SJ Amsterdam, The Netherlands
[2] Sterrewacht Leiden, Postbus 9513, NL-2300 RA, The Netherlands

Received October 4, 1990; accepted April 3, 1991

Abstract. — In order to study the processes that (strongly) enhance the star formation rate in some galaxies we have selected 62 galaxies from the IRAS point source catalogue with far-infrared to blue luminosity ratios (L_{FIR}/L_B^0) of three or larger. These galaxies form a subset of a far-infrared complete sample of 254 sources in two fields covering in total 1500 square degrees of the southern sky ($10^h \leq \alpha \leq 14^h$ and $-40° \leq \delta \leq -20°$; $20^h \leq \alpha \leq 22^h$ and $-40° \leq \delta \leq -20°$). The sources in the far-infrared complete sample all have flux densities larger than 1 and 2.5 Jy at 60 and 100 μm, respectively, to ensure completeness. Furthermore, in order to select mainly galaxies, for all sources the flux densities at 60 and 100 μm are larger than at 12 and 25 μm. We initially used $B-$band magnitudes estimated from ESO/SRC and POSS sky survey plates to estimate L_{FIR}/L_B ratios for all galaxies in the far-infrared complete sample, and we selected only those galaxies for the optical observations that have $L_{FIR}/L_B^0 \geq 4.3$, thus obtaining a sample of 62 galaxies. Comparison of the estimated with the observed, corrected CCD B-band magnitudes later revealed that the actual L_{FIR}/L_B^0 selection criterium is less sharp and corresponds to $L_{FIR}/L_B^0 \gtrsim 3$. For these 62 sources we also obtained far-infrared co-added flux-densities, so that 100%, 95%, and 70% of the sources are detected at 60 and 100, 25 and 12 μm, respectively. Due to the L_{FIR}/L_B selection criterion and the correlation between L_{FIR}/L_B and the S_{100}/S_{60} flux density ratio the subsample of 62 galaxies consists only of warm sources with $\log(S_{100}/S_{60}) \leq 0.4$. The optical observations comprise long-slit CCD spectra in the 4800-7300 Å wavelength range, broad-band B, V and R, and narrow-band Hα CCD images. In this paper we present the optical observations and show spectra, and broad-band, colour and continuum-subtracted Hα CCD images for more than 50 galaxies. The spectra are mostly HII-types although some 25% are AGN-types. The broad-band images show, among other things, that our sample predominantly consists of barred spirals and distorded interacting system, while the Hα images show in most cases small compact sources. From the spectra we derived redshifts, line-ratios, equivalent widths, and extinction determinations from the Hβ/Hα line ratios. We also derived integrated magnitudes, colours, Hα fluxes, diameters and luminosities of the galaxies from the CCD images. We determined average luminosity profiles of all early-type galaxies and all possible merger candidates in our sample, and we found that all these galaxies have exponential disks except two objects that follow a de Vaucouleurs $r^{1/4}$ law: a merger candidate, and an elliptical galaxy in a close interacting pair (the latter is not an IRAS galaxy, however).

Key words: galaxies: general — galaxies: structure of — galaxies: redshifts — galaxies: active.

1. Introduction.

This paper is the first in a series presenting the results of a study of the optical, far-infrared, radio continuum, and CO-line properties of a far-infrared complete sample of galaxies with high far-infrared to blue luminosity ratios, hereafter referred to as extreme IRAS galaxies, in two southern fields. This sample of extreme IRAS galaxies has been defined according to strict selection criteria (see Sect. 2), in order to allow a statistical analysis of the results, and is therefore well-suited for a study of the processes that enhance star formation in galaxies.

In this first paper we present the optical observations of a far-infrared complete subsample of about 50 of the most extreme IRAS galaxies (far-infrared to blue luminosity ratio $L_{FIR}/L_B^0 \gtrsim 3.0$). The optical data consist of long-slit CCD spectra, broad-band B, V, R, and narrow-band Hα CCD images, from which we derive redshifts, line ratios, equivalent widths, magnitudes, diameters and information on morphologies and colour distributions.

Send offprint requests to: W. van Driel.
* Based on observations collected at the European Southern Observatory, La Silla, Chile.

In future papers we will present VLA 6 cm continuum observations (van Driel *et al.* 1991), CO($1 \rightarrow 0$) line spectra (van Driel & van den Broek 1991) and an overview and discussion of the combined observational data (van den Broek 1991).

In recent years extensive studies have been published of two other large far-infrared complete galaxy samples: (1) the so-called minisurvey sample consisting of about 80 galaxies detected in the IRAS minisurvey (Soifer *et al.* 1984, Carico *et al.* 1986, Eales *et al.* 1988, Moorwood *et al.* 1986, 1987), and (2) the so-called Bright Galaxy Sample (Soifer *et al.* 1987a) comprising about 300 galaxies with 60 μm flux densities greater than 5.4 Jy, of which the most far-infrared luminous have been studied in detail (see Carico *et al.* 1988, Mirabel & Sanders 1988, Sanders *et al.* 1986, 1988).

Since we selected galaxies with high L_{FIR}/L_B ratios, our sample is intermediate between the minisurvey sample and the luminous subsample of the Bright Galaxy Sample. The minisurvey sample galaxies have on average less extreme L_{FIR}/L_B ratios and hence a lower star formation activity. On the other hand, our sample contains galaxies with moderate optical luminosities and high far-infrared excesses, rather than exclusively infrared ultra-luminous objects, like those studied from the Bright Galaxy Sample, in which not only star formation, but also nuclear activity appears to enhance the far-infrared emission.

Distance are determined from velocities, calculated according to the conventional optical definition ($V = c\Delta\lambda/\lambda_0$) and corrected for the galactic rotation of the sun using $\Delta v = 300\sin(l)\cos(b)$. A Hubble constant $H_0 = 75$ km s^{-1} Mpc^{-1} is used and no relativistic corrections are applied.

The paper is organized as follows. In section 2 we define the selection criteria and describe the sample and in section 3 we present co-added IRAS flux densities. In section 4 we discuss the observations and the data reduction and in section 5 we present the results. In section 6 we discuss the L_{FIR}/L_B selection criterion.

2. Sample definition.

In order to select a far-infrared complete sample of galaxies optimized for observations at the European Southern Observatory (ESO) in Chile, we whose two fields in the southern sky between declinations of −20° and −40° and between right ascensions of $10^h - 14^h$ (Field I) and $20^h - 22^h$ (Field II). Most of this area is at galactic latitudes larger than 20°, thus avoiding confusion with galactic infrared sources.

We selected all sources in these fields from the IRAS Point Source Catalogue (IPSC 1985) with 60 and 100 μm flux densities larger than 1 and 2.5 Jy, respectively, in order to avoid spurious detections and to ensure the completeness of the sample (see e.g. Soifer *et al.* 1987b). Then to select the galaxies from this large sample of infrared sources we required that the flux densities at 60 and 100 μm would both be larger than those at 12 and 25 μm. This resulted in a sample of 199 sources in Field I and 55 sources in Field II.

The identification of the optical counterparts on ESO/SRC and Palomar Observatory Sky Survey plates was in general straightforward. For almost all sources we found one or more obvious candidate galaxies within the error ellipse of the IRAS position. After inspection of the plates we excluded 10 sources, of which eight were of a galactic origin: one planetary nebula, one cirrus-like source, three star-forming complexes and three stars. These eight sources have far-infrared colours different from those of galaxies. Of the two remaining sources one has galaxy-like colours and as brightest possible optical counterpart a star of blue magnitude ~ 13, probably too bright to be an uncatalogued quasar. The other lies in the disk of the bright nearby galaxy NGC 5236(M83).

The remaining 244 sources (191 in Field I, and 53 in Field II) are associated with galaxies and nearly all have high-quality detections. Only 7 sources at 60 μm and 3 sources at 100 μm have intermediate-quality detections. Only the sources associated with NGC 5236 and NGC 5068 are extended according to the IRAS Small Scale Structure Catalog (Helou & Walker 1986, see also Rice *et al.* 1988), whose flux density we adopted. Of the 244 sources about 30% are detected at 25 μm, and a few at 12 μm. Later, we could greatly improve the detection rates for the finally selected sources using co-added IRAS flux densities (see Sect. 3).

Note, that the number density of sources differs by a factor of two between Field I and Field II. Since both fields together cover 2% of the total sky we estimate that a total of about 10,000 galaxies would satisfy our flux density criteria. This is in reasonable agreement with the earlier estimate (Soifer *et al.* 1987b) that a total of about 25,000 galaxies are detected in the IRAS survey.

We calculated L_{FIR}/L_B luminosity ratios using the relation

$$\log\left(L_{FIR}/L_B^0\right) = \log(FIR) + 0.4B_0 + 7.52 \qquad (1)$$

where FIR, the far-infrared flux between 40 and 120 μm, is calculated from the 60 and 100 μm flux densities, S_{60} and S_{100}, using the relation (Lonsdale *et al.* 1985)

$$FIR = 1.26 \times 10^{-14}\,(2.58\,S_{60} + S_{100}) \;\left[\mathrm{Wm}^{-2}\right] \qquad (2)$$

where S_{60} and S_{100} are in Jansky. The integrated $B-$band flux defined as $\nu_B S_B$ is calculated form the $B-$band magnitude using the calibration of Johnson (1966) and it has been corrected for galactic extinction according to the relation

$$B_0 = B - 0.2(\sin|b|)^{-1} \;\;[\mathrm{mag}] \qquad (3)$$

where b is the galactic latitude.

1991A&AS...91...61V

We estimated the $B-$band magnitudes from the logarithm of the apparent galaxy diameters using a linear relation (see Fig. 1). This relation has a slope of -5, since the average surface brightness of galaxies is about constant and independent of distance, and it has been calibrated using catalogued B magnitudes for about 30% of the sources (see Lonsdale *et al.* 1985). We measured diameters from ESO/SRC Sky Survey plates, if available, and otherwise from Palomar Observatory Sky Survey plates. The relation is expressed by

$$B = -5 \log D + (23.1 \pm 0.7) \ \text{[mag]} \tag{4}$$

where D is the diameter in arcseconds; the uncertainty reflects the scatter in the data. We used this relation to determine magnitudes for all 244 sources, including those with published magnitudes. When two galaxies can be associated with a far-infrared source, we derived a L_{FIR}/L_B ratio using the average magnitude of both galaxies. However, in the case of a dwarf companion, we used the magnitude of the main galaxy. Close interacting pairs, for which we could not measure the diameter of the individual galaxies, were treated as a single galaxy.

In section 6 we will compare the magnitudes estimated to those measured directly from CCD-images and we discuss the effect of the errors in the magnitudes on the L_{FIR}/L_B selection criterion.

To end up with a sample of manageable size we selected all objects with an estimated $L_{FIR}L_B^0 > 4.3$ (which in fact corresponds to $L_{FIR}/L_B^0 \gtrsim 3$, see Sect. 6), yielding 42 sources in Field I and 16 sources in Field II.

Throughout this paper we will refer to the above mentioned far-infrared complete sample of 244 sources as the "far-infrared complete sample", and to the 58 sources selected for observations as the "extreme subsample". Furthermore, 4 sources selected from IRAS Circular no. 14 (1984) which do not satisfy the selection criteria, but had been already observed earlier, are presented in this paper as "miscellaneous" sources.

We completed the observation of virtually all 42 sources of the extreme subsample in Field I, but due to unfavorable weather conditions only 5 out of the 16 sources of the extreme subsample in Field II could be observed.

2.1. SELECTION EFFECTS.

In Figure 2a we present the far-infrared flux FIR versus the far-infrared S_{100}/S_{60} colour for the far-infrared complete sample and in Figure 2.2b for the extreme subsample. From a comparison of both Figures it is clear that the sources in the extreme subsample have smaller S_{100}/S_{60} ratios, consistent with the correlation between L_{FIR}/L_B and S_{100}/S_{60} (de Jong *et al.* 1984).

In both Figures the falling and rising curve represent the lower limit of the 100 and 60 μm flux densities, respectively. The 60 μm limit does not constrain the extreme subsample at all, since it only contains relatively warm sources with $\log(S_{100}/S_{60}) < 0.4$. The non-zero slope of the 100 μm limit implies that the source selection is not independent of the far-infrared colour, since for $FIR < 10^{-13}$ W m^{-2} only the cooler sources have been selected. However, this latter selection effect will not significantly influence our statistical analysis (see van den Broek 1991).

3. Co-added IRAS fluxes

To improve the rather poor detection rates at 12 and 25 μm (see Sect. 2) using the IPSC, we obtained co-added flux densities for all 58 sources of the extreme subsample as well as for the four miscellaneous sources from the Infrared Processing and Analysis Center (IPAC) in Pasadena. Individual IRAS scans at each galaxy position were averaged in the co-adding process to produce median average and noise-weighted average intensity-position plots. The IRAS beam templates were then fitted to the data (see IRAS Explanatory Supplement 1985) to give an amplitude (flux density) and rms noise in all four IRAS bands. After our inspection of the intensity-position plots we conclude that the median average of the IRAS scans gives the best results. We only accepted a detected flux density when the signal-to-noise ratio was larger than 3 and the correlation coefficient of the template-fit was better than 0.85.

The co-added flux densities at 60 and 100 μm agree within 5% with the IPSC data. The detection rate at 12 μm and 25 μm is greatly improved with respect to the IPSC data, since there are now detections for nearly all selected sources at 25 μm and for about 65% of the sources at 12 μm.

The total error σ_T in the co-added IRAS flux densities is given by

$$\sigma_T \sim \left(\sigma^2 + \epsilon^2 S^2\right)^{\frac{1}{2}} \tag{5}$$

where σ is the rms noise and S is the flux density. The last term in Eq. (5), ϵS, represents the systematic error in the absolute flux density calibration, with ϵ = 0.02, 0.05, 0.05, and 0.10 for 12, 25, 60, and 100 μm, respectively (IRAS Explanatory Supplement 1985). This implies that the errors are mainly due to noise at 12 and 25 μm and to systematic errors at 60 μm and 100 μm. Typical errors are ±0.03, 0.05, 0.20, and 0.65 Jy at 12, 25, 60, and 100 μm, respectively.

4. Optical observations and data reduction

4.1. SPECTRA

Long-slit CCD spectra were obtained with the ESO 3.6 m and 2.2 m telescopes in 1985-1989 (see Tab. 1), using a Boller and Chivens spectrograph with a dispersion of 172 Å mm^{-1} and an RCA CCD detector, giving a wavelength coverage of 4800-7300 Å and a resolution of about 7 Å. The slit of the spectrometer has a width of 1$''$.5 and it was always placed across the nucleus, so that the spectra are in general dominated by emission from the nuclear regions of the galaxies. An Image Dissector Scanner (IDS) detector (aperture 4$''$ × 4$''$) giving a wavelength coverage of 4800-8000 Å and a resolution of about 11 Å was used on 16/17 April 1985 only. Integration times were typically 20 minutes, except for the weak source No. 22 where the total integration time was 110 minutes. Wavelength and flux calibration as well as bias subtraction were carried out in a standard way with the MIDAS image processing system, using the white dwarfs W485, Kopff 27 and Feige 56 as standard stars.

We determined redshift and line fluxes MIDAS and an automatic line-searching and -fitting program (de Grijp, private communication) We considered only lines with signal-to-noise ratios exceeding 2.5.

Some spectra show a velocity gradient across the galaxy, but the resolution of 7 Å, corresponding to a velocity resolution of ~ 300 km s^{-1}, is too poor to derive rotation velocities.

4.2. CCD IMAGES

Broad-band B, V, R, and narrow-band Hα images were obtained with the ESO 1.5 m Danish telescope using standard ESO CCD detectors and filters (see Tab. 2 and Fig. 3) in 1985-1989. Note, that the Cousins and Johnson $B-$ and $V-$band filters are practically identical. We used a set of comparable Hα filters, each with a FWHM of about 80 Å, and with central wavelengths corresponding to the redshifts of the observed objects. Of each object the B, V, R, and Hα-band images were made sequentially in time as much as possible, although some Hα-band observations were made at other dates (see Tab. 5). Integration times were typically 20 minutes for the $B-$ and Hα-band and 10 minutes for the $V-$ and $R-$band.

The pixel size of the images is 0$'$.47 × 0$'$.47, yielding a total field of 2$'$.4 × 4$'$.0 ($\alpha \times \delta$). CCD#1 needed pre-flashing in order to prevent deformation of the images of low count levels during read-out, and for the high-resolution CCD#15 we rebinned the frames to the same pixel size as the other CCD's. The sensitivity of CCD#15 varied by a factor of 2 over the columns at low count levels and since flatfielding can only partly remove this effect, its residual defect can still be seen, especially in colour images; the observations made with this chip also show many isolated pixels containing a high value, so-called cosmics, which are however mainly due to radio-activity inside the chip itself.

Since for the calibration and colour corrections we used standard stars from Graham (1982) and Landolt (1983), the calibrated magnitudes are expressed in the Cousins system, even when the observations were made in the Gunn-r band. Standard bias-subtraction and flatfielding were carried out with MIDAS, and corrections for atmospheric extinction were done using standard values for La Silla (0.25, 013, 0.05 and 0.05 mag airmass^{-1} for B, V, R and Hα, respectively, see Rufener 1986).

From the Hα images we subtracted the continuum using the R-band images and we determined the ratio of the total transmission between the $R-$band and the Hα filters by means of standard star observations. Only in run J86 (see Tab. 2) we used neighbouring Hα-filters for continuum subtraction. For the absolute flux calibration of the Hα images and fluxes we used a flux density calibration for the Cousins-R band (Bessel 1979), a FWHM of the Hα filters of 80 Å and the measured transmission ratio between the Hα and $R-$band filters. In general the data allow surface photometry to be performed down to a level of 25.5 mag arcsec^{-2} in $B-$band plots. From the images we derived integrated magnitudes in the $B-$, $V-$ and $R-$band, and integrated fluxes in the Hα-band using circular apertures. The uncertainty in the $B-$, $V-$, and $R-$band magnitudes of 0.03 – 0.05 is mainly due to the uncertainty in the sky-background subtraction and the uncertainty in the logarithm of the Hα fluxes of about 0.1 is due to the uncertainty in the continuum subtraction.

5. Results

Data for the extreme subsample as well as for the four miscellaneous sources are presented in Table 3 where we list our own sequence number for each object and, if available, an E-designation from the ESO/Uppsala Survey (Lauberts 1982), and NGC number, and an AM-designation from the Atlas of Southern Peculiar Galaxies (Arp & Madore 1987). Also given are positions of the IRAS sources, co-added IRAS flux densities, and optical positions of candidate IRAS galaxies for the observed sources, the latter measured from Palomar Sky Survey prints with an accuracy of about one arcsecond, or somewhat larger for objects without a distinct nucleus. When more possible optical counterparts are given, an asterix denotes which galaxy probably is the IRAS galaxy, since it is detected at radio wavelengths (van Driel *et al.* 1991), following the far-infrared/radio correlation (de Jong *et al.* 1985).

Note, that we have divided the Table in three parts: in Tables 3a, b and c we present the 42 sources in Field I, the 16 sources in Field II, and the four miscellaneous sources, respectively. All other tables are divided in the same way .

5.1. SPECTRA

The spectra are shown in Figure 10 and the results obtained from the spectra are summarized in Table 4. Listed are the ratios between the $H\beta$ (λ4861 Å), [OIII](λ5007 Å), Hα(λ6563 Å), [OI](λ6300 Å), [NII](λ6583 Å) and the combined [SII](λ6716 + 6731 Å) emission lines, the extinction in the B-band derived from the Hα/Hβ line ratio, the equivalent width of the blended NaID(λ5890, 5896 Å) absorption lines, and uncertainties, as well as reddening-corrected values for the line ratios.

For the reddening correction we used the Hα/Hβ decrement, assuming an unreddened Hα/Hβ line ratio of 2.85 for HII galaxies and 3.1 for active galaxies (see Veilleux & Osterbrock 1987), and using a standard reddening curve parameterized by Miller & Mathews (1972) as

$$A_\lambda = 0.74\,\lambda^{-1} - 0.34 \text{ [mag]} \qquad (6)$$

for the wavelength region of interest, following Veilleux & Osterbrock (1987), where λ is expressed in μm. In Table 4 we also present redshifts with a typical uncertainty of 0.0005 (150 km s^{-1}), the FWHM of emission lines, and a global classification of the spectra into HII-region-, LINER-, Seyfert I- and Seyfert II- types, made using diagnostic diagrams (see Fig. 4) between reddening-corrected line ratios of emission lines (cf. Veilleux & Osterbrock 1987). We will use AGN- type spectra as a generic description of LINER- and Seyfert-type spectra.

For about a quarter of the sources redshifts are available in the literature. These redshifts are in general in good agreement with our data. The references with the numbers of the associated sources in brackets are: Bergvall and Olofsson 1986 (2, 19), Da Costa *et al.* 1989 (57, 58), Da Costa *et al.* 1986 (29), Fairall *et al.* 1989 (11, 15, 17, 27, 30, 62), Fairall 1981 (24, 25), Fricke & Kollatschny 1989 (24), Kollatschny & Fricke 1983 (10), Menzies *et al.* 1989 (11, 57, 61), Rowan-Robinson *et al.* 1989 (1, 15, 58) and Winkler 1988 (7).

Note, that we do not present the IDS spectra (see Sect. 4), since they are not of the same quality as the CCD spectra and they do not add new information, except for the distant source No. 41 where the Hα and [NII] lines are outside the wavelength range covered by the CCD.

5.2. IMAGES

In Table 5 we present photometric properties derived from the CCD-images. In column 3 we indicate the observing runs (cf. Tab. 2); when the Hα observations were done during another run, this is denoted between brackets. The total integrated B_T^0 magnitudes, colours and Hα + [NII] fluxes in columns 4 to 7 have been corrected for galactic extinction using $E(B-V)$ values (column 2) from Burstein & Heiles (1982), which are more precise than those from Equation (3), and using $A_B : A_{H\alpha} : E(V-R) : (B-V)$ =4:2.3:0.6:1. Note, that the Hα flux includes the contribution of the [NII] lines. Note also, that in one case (No. 22), no Hα image is available. We give therefore an Hα + [NII] flux estimated from the Hα + [NII] equivalent width obtained from the spectrum and the Cousins-R magnitude of No 22. In column 8 we give the optical diameter D_{25} of the major axis at the 25 mag arcsec^{-2} isophote level in the $B-$band and in column 9, if possible, the minor-to-major axis ratio (b/a). In column 10 we give a global morphological classification. Note, that in general we use the revised Hubble classification as illustrated by Sandage (1961), and Sandage & Tammann (1981), and that we identify intermediately barred objects as SAB..; following de Vaucouleurs *et al.* (1976).

We classified the non-isolated galaxies in our sample as close interacting pairs (CIP), interacting pairs (IP), or pairs (P); furthermore, we tentatively identified a number of merger candidates (M) as well. The optical criteria we used for this division were as follows. Close interacting pair: an interacting pair with such small separation, that on the deep CCD images a common envelope is seen around them. Interacting pair: two nearby galaxies with clear signs of interaction, such as bridges or tails and/or a distorted morphology. Pair: two comparable sized galaxies with a separation of several diameters, without obvious signs of interaction. Group: a number of galaxies of comparable size are seen in the vicinity of the IRAS galaxy. Merger candidate: a "single" distorted galaxy, often with two distinct peaks in its inner light distribution, both in the radio continuum and (especially) in Hα.

For some sources optical photoelectric photometry is available in the literature. However due to the small aperture sizes used a direct comparison to our observations is not possible. The references with the numbers of the associated sources in brackets are: Bergvall & Olofsson 1986 (2, 19), Hamuy & Maza 1987 (24,58), Peterson 1985 (61), Winkler 1988 (7).

In Table 6 we present total luminosities and absolute optical diameters, as well as L_{FIR}/L_B^0 ratios and far-infrared colours. Note, that radio data (van Driel *et al.* 1991) have been used to determine which member of a pair of galaxies is the probable IRAS source. Note also, that in three pairs (sources Nos. 12, 20 and 33) radio emission is clearly detected in both members of a pair, which probably both have enhanced far-infrared emission, this in contrast with the assumptions made in the selection procedure (see Sect. 2). However, all three systems still satisfy the L_{FIR}/L_B selection criterion, even when we add the $B-$band fluxes for each pair and then calculate the L_{FIR}/L_B^0 ratio for the entire system (see Tab 6). In these cases also the far-infrared luminosity and the far-infrared colours are given for the entire system, but the optical luminosities and the diameters are given for each member separately.

In Fig. 11-67 we present images of the observed galaxies, generally a $B-$ band image (top), a colour image, mostly $B-R$, (middle), and an Hα image (bottom). Note, that east is to the right and north is up. In making the colour images we used only those parts of the galaxies which have a signal-to-noise ratio of three or better in both bands. In all images the plotted contours have been slightly smoothed.

5.3. LUMINOSITY PROFILES

We have determined average luminosity profiles from the red CCD images of a number of galaxies, where the determination of such a profile can provide essential information about the morphological classification and the dynamical state of the galaxy, i.e. (1.) galaxies for which the classification as either S0 or elliptical was not clear from an inspection of the CCD image and (2.) all possible merger candidates. We expect to find either an exponential disk and a bulge for the S0- type galaxies, or a de Vaucouleurs' $r^{1/4}$ law for an elliptical or a "classical" merger candidate; in one case (No. 11) did we actually find a clear de Vaucouleurs' profile, while the other case (No. 41S) is less clear.

We derived the profiles with the interactive GIPSY image processing system, using eye-estimates for the position of the galaxy centre, the axial ratio of the isophotes and the position angle of the morphological major axis. We will show only the results for the blue compact dwarf galaxy No. 2, for the merger candidate No 11 and for the close interacting galaxy pair No. 41 N + S; all other luminosity profiles will be discussed briefly in Sect. 5.4. *Source No. 2:* The CCD image (Fig. 11) shows two bright regions. Since the Eastern region lies in the centre of symmetry of the galaxy, we used this position for the determination of two independent profiles (marked as E and W in Fig. 5) for each half of the galaxy. The eastern profile clearly shows the influence of the other prominent star forming region, but it does not extend out to large radii, since the image lies close to the edge of the CCD chip. The profile of the west side can quite well be represented in the outer regions by an exponential disk with a scale length of $8''$ (=0.24 kpc) and a red central surface brightness of 18.4 mag $(\mathrm{arcsec})^{-2}$, while the presence of a bulge is clearly visible in the inner regions. Note, that around $r = 0\farcm5$ three points were taken out, due to a bright foreground star.

This result does not support the claim of Kunth *et al.* (1985), who fitted an $r^{1/4}$ law to their profile of this galaxy. This discrepancy is due to the fact Kunth *et al.* used a limited range of radii, where a de Vaucouleur's law may seem to give an adequate fit, but our superior data show this to be spurious, indicating that this object is a dwarf disk galaxy and not a relaxed merger system.

Source No. 11: Also this galaxy shows two equally bright star formation regions near its centre of symmetry, but only in the Hα and radio continuum images; in continuum light it shows a central peak in its brightness distribution, which we assumed to be the centre of the galaxy. Due to instrumental problems with the R−band image, we derived a luminosity profile (Fig. 6) in the V band. This galaxies shows quite some variation in the axial ratio and position angle of its isophotes, which sometimes have a "boxy" appearance, and we used the parameters of the isophotes at intermediate brightness levels for all radii. As Figure 6 clearly shows, this galaxy is the only merger candidate in our sample that roughly follows a de Vaucouleurs' law, like a "classical" merger (see e.g. Schweitzer 1990, Lutz 1991a, 1991b).

Source No. 41: We can not separate the far-infrared emission of the two galaxies in this close interacting pair, but only No. 41N is detected in the Hα and radio continuum images, indicating that only this galaxy is undergoing a starburst (see also Sect. 5.4). The presence of a tail to the south of the pair is a clear sign of their interaction. We made luminosity profiles of the northern half of No. 41N and of the southern half of No. 41S, in order to avoid contamination by the nearby companion galaxies (see Fig. 7). The luminosity profile of No. 41N clearly shows an exponential disk with a scale length of $1\farcs24$ (= 3.1 kpc), and a red central surface brightness of 18.4 mag $(\mathrm{arcsec})^{-2}$. The luminosity profile of No. 41S globally follows a de Vaucouleurs' $r^{1/4}$−law, but it shows a break at the radius where we expect the contribution from the tail to become noticeable. The classification of No. 41S as an elliptical galaxy would be consistent with its quiescent nature, its very red colours, $(B-V)_{\mathrm{T}}^{0} = 1.29$ mag and with the absence of emission lines in its spectrum.

5.4. NOTES ON INDIVIDUAL GALAXIES

No. 1, M?/CIP. Distorted galaxy with tails and two bright regions in the blue. The least bright region in the blue dominates the Hα emission.

No. 2, pec. Blue compact dwarf galaxy with two bright spots, of which the eastern is very blue. The spectrum shows very strong [OIII] emission lines in an HII-type spectrum. (See also Sect. 5.3)

No. 3, S0. Early-type galaxy with strong nucleus. The bright north-eastern emission is probably a star. The Hα is confined to the nucleus, which shows an AGN-type spectrum. The luminosity profile clearly shows a disk and bulge, confirming its classification as a lenticular.

No. 4, SBb(s). Hα emission is also observed in the bar.

No. 5, CIP. This system shows tails and strong compact Hα emission is observed to the west of the nucleus of the brighter galaxy. The radio emission coincides with the Hα.

No. 6, SBab(s). Hα emission is concentrated in the nucleus, which shows an AGN-type spectrum.

No. 7, SBb(s). Hα emission is also observed in the bar.

No. 8, S0pec. Blue compact dwarf galaxy with Hα emission extended over most of the disk. The R−band and Hα images are affected by a guide probe in the light path making the Hα and R−band fluxes less certain. The luminosity profile clearly shows an exponential disk; the presence of a bulge can not be established, since the deformation of the innermost contours disturbs the luminosity profile.

No. 9, SBbc. Hα emission is also observed in the bar.

No. 10, SBb(s). Barred spiral with blue nucleus. Some Hα emission is present in the bar, but most of the emission is from the active nucleus with Seyfert I-type spectrum. In Table 5 we give the FWHM of the permitted lines.

No. 11, M. Distorted system with two nuclei in Hα showing tails, boxy isophotes and possibly shells. The R–band and Hα images are severely affected by a guide probe in the light path, which makes the Hα and R–band fluxes very uncertain. Only the highest contour levels can therefore be shown in the Hα image. (see also Sect. 5.3)

No. 12, IP, NW: Irr, SE: S?. Pair of interacting galaxies showing a bridge and consisting of a highly inclined galaxy and a spiral with Hα emission concentrated in the nucleus, which shows an AGN-type spectrum.

No. 13, pec(r). Distorded galaxy showing a ring-like structure in the blue and a more double structure in Hα. The CCD images show at a distance of about 1′ another (background?) galaxy, for which no redshift information is available.

No. 14, SABa(s)pec. Highly inclined, probably barred spiral galaxy. Red nucleus showing concentrated Hα emission and an AGN-type spectrum.

No. 15, SBb. Barred galaxy with weak anomalous spiral arms. Hα emission shows a patchy ring of spots around the center. Not visible in the image is the larger low surface brightness disk. Note the absence of [OIII] emission lines in the spectrum.

No. 16, S0?pec. Spot to the east is probably a star. The nucleus shows concentrated Hα emission and an AGN-type spectrum. The luminosity profile clearly shows a disk, cf. Source No. 8.

No. 17, CIP. Close interacting system showing tails. The southern, inclined galaxy shows two bright regions of which the northern red region emits most of the Hα emission and shows an LINER-type spectrum. The Hα emission of the northern galaxy is concentrated in the centre and it shows an HII-type spectrum. To the south-east an overexposed star is seen. Radio data indicates that the southern galaxy is the IRAS source.

No. 18, Sbpec. Small inclined galaxy. Hα emission is extended over the complete inner region.

No. 19, pec. Blue compact dwarf galaxy with clear nucleus. Other regions also seen in the Hα emission are large blue HII complexes. The luminosity profile clearly shows a disk, but no evidence for a bulge.

No. 20, IP, W: S?pec, E:S?pec. Interacting pair showing a bridge. Both galaxies are distorded. The active western galaxy has an SII-type spectrum superimposed on an underlying post-starburst spectrum, clearly showing the MgIb (λ5180 Å) and TiO(λ6200 Å) absorption features. The Hα emission shows an elongated structure pendicular to the major axis; probably a polar gas disk. The Hα emission of the eastern galaxy shows a strong nucleus and a second bright region. Radio emission is found in both galaxies.

No. 21, IP, SW: S?, NE: pec. Interacting pair showing a bridge. Both galaxies are rather red and the southern galaxy shows a spectacular tail. The northern galaxy shows a blue and red nuclear region and is far more luminous in the radio than can be expected from the far-infrared flux density. Both galaxies show AGN-type spectra.

No. 22, SO?. Very small ($D_{25} = 2.8$ kpc), red, dwarf galaxy without much structure. The object south of the galaxy is a star. Note the prominent TiO(λ6200Å) absorption band and the strong NaID(λ5890 Å) absorption line. No Hα image is available. The luminosity profile clearly shows an exponential disk with a scalelength of 0.44 kpc, but no bulge.

No. 23, CIP, N: SBc(s)pec, S: pec. Interaction between a large barred spiral (north) and a dwarf galaxy (south). Hα emission is seen in the nucleus as well in spots in the bar of the northern spiral. The dwarf galaxy also clearly shows Hα emission. Very weak interaction tails to the west and east are present although not visible in the images. radio data indicates that the main galaxy is the IRAS source.

No. 24, P, SW: SBc(rs), NE: SBc(r). The south-western galaxy, which coincides with the IRAS source shows many spots visible in the Hα emission, presumably HII regions. Its nucleus shows an Seyfert II-type spectrum. The north-eastern galaxy shows an ring of HII regions.

No. 25, Sb. Small spiral with Hα emission spread out over a large part of the disk. A second galaxy, which has probably the same redshift, is found at a distance of about 2′ on the CCD images.

No. 26, SB0/apec. Hα emission is also observed in the bar. The luminosity profile clearly shows a disk and a bulge.

No. 27, SAB0/a. Red barred spiral with compact Hα emission in the centre. The spectrum shows the MgIb (λ5180 Å) and TiO (λ6200 Å) absorption features.

No. 28, M?/CIP. Red distorted galaxy. Probably a highly inclined merger of which an interaction tail can be seen to be north-east. The Hα emission is concentrated in the nucleus, which shows an AGN-type spectrum. The luminosity profile clearly shows an exponential disk, the presence of a bulge can not be established, due to the disturbed innermost contours.

No. 29, SBb. Hα emission is also observed in the bar. The MgIb(λ5180 Å) absorption line is present in the spectrum.

No. 30, CIP. In the north-western galaxy the Hα emission shows a ring of HII regions around the nucleus, of which those to the east are very prominent but those to the west are inconspicuous in the blue, due to dust absorption. The south-eastern galaxy shows compact Hα emission. Very weak interaction tails to the north and south are present although not visible in the images shown here. Radio emission is found in both galaxies.

No. 31, S0. Small blue early-type galaxy with concentrated nuclear Hα emission showing an HII-type spectrum. The luminosity profile clearly shows a disk and a prominent bulge.

No. 32, Spec. Red highly inclined galaxy with a relatively blue nucleus. Hα emission confined to the inner region.

No. 33, I?P,S: S0/a, N: Sbpec. Pair of spiral galaxies of which the northern is blue and the southern is red. Both show Hα emission. Radio emission is found in both galaxies.

No. 34, CIP?. Peculiar system with cigar-like structure to the north-west. Hα emission is mostly concentrated in the nucleus.

No. 35, SB0/a:. Hα emission is also observed in the bar. The luminosity profile clearly shows a disk and perhaps a weak bulge.

No. 36, M?/CIP. Blue distorted system with extended low-level emission in the northern part of the disk. Extended Hα emission shows a double structure. The luminosity profile clearly shows a disk, but no bulge.

No. 37, SBcpec. Hα emission is also observed in the bar. On enlargements from deep ESO/SERC Sky Survey plates with a 10′ field of view, we find several other galaxies, indicating that this galaxy is a possible group member.

No. 38, CIP, E: S?pec, W: dwarf. Interaction of an highly inclined galaxy with a dwarf galaxy. Hα and radio continuum emission are only observed in the main galaxy.

No. 39, Scpec. Spiral showing a broad southern arm and Hα emission spread out over its disk. The MgIb (λ5180 Å) absorption line and TiO (λ6200 Å) absorption band are present in the spectrum.

No. 40, SBb:. Barred? spiral with extended Hα emission in its inner region. The small (background?) galaxy to the south is very red. On enlargements from deep ESO/SERC Sky Survey plates with a 10′ field of view, we find several other galaxies, indicating that this galaxy is a possible group member.

No. 41, CIP. Distant interacting double. The luminosity profile of No. 41N clearly shows a disk, but no bulge, and the luminosity profile of No. 41S follows a de Vaucouleurs' $r^{1/4}$–law, but it may be contaminated by a tail to the south of the galaxy (see also Sect. 5.3). So the southern galaxy is probably a very red elliptical with a clear tail. Only the northern galaxy shows Hα emission in the CCD image as well as radio continuum emission, indicating that probably all far-infrared emission originates in this object, implying a log (L_{FIR}/L_B^0) ratio of 2.05 (see Tab. 4), which is about as extreme as the prototype ultraluminous IRAS galaxy Arp 220. Note, that we obtained two spectra of this system: a single IDS spectrum taken with an aperture which includes both galaxies (see Sect. 5.1), which covers the wavelength region of the Hα line and CCD spectra of both objects, which do not extend out to be redshifted Hα line. We therefore can only measure a redshift and determine a spectral classification (AGN-type) for the whole system. However, since probably all emission lines originate in the northern object this information actually concerns this object only (see table 4).

No. 42, Sc:. Small highly inclined galaxy with extended Hα emission.

No. 43, I?P?. The red eastern galaxy shows irregular structure to the north. the nucleus shows concentrated Hα emission and an AGN-type spectrum. The TiO(λ6200 Å) absorption band is present in the spectrum. Radio emission is found in this source, but is absent in the western galaxy of which no spectrum is available so that we cannot decide whether this galaxy is a background galaxy or it is part of a double system.

No. 45, S0/apec. Peculiar early-type galaxy, for which only a blue-band image is available. The luminosity profile clearly shows a disk, but no bulge.

No. 46, pec. Peculiar galaxy, for which only a blue-band image is available.

No. 47, CIP. Triple system of which the most western object is an early-type galaxy. Radio emission is found in both the western and the north-eastern component, but only the last coincides with the IRAS position and forms a close interacting system, showing clear tails, with the third component. Furthermore the north-eastern galaxy shows compact Hα emission and an AGN-type spectrum.

No. 50, S0/apec. Peculiar early-type galaxy, for which only a blue-band image is available. The luminosity profile clearly shows a disk, but no bulge.

No. 51, SBa. Barred spiral, for which only a blue-band image is available.

No. 54, CIP. Distorted system showing tails and with double structure indicating a merging process.

No. 55, P, N: pec, S: ?. Pair of galaxies of which the northern galaxy shows most of the Hα emission and is also more blue than the southern galaxy. Radio data indicate that the northern galaxy is the IRAS source.

No. 57, CIP. Close interacting double with strong tails. The southern galaxy shows a blue band along the major axis. Hα emission is present in both components and the northern galaxy shows an AGN-type spectrum. Radio emission is found in both galaxies.

No. 58, SBbpec. Distorted galaxy with Seyfert II-type spectrum. Two blue areas are seen next to the nucleus. The very red spot to the south-west is possibly a foreground star. The Hα emission is extended and shows a kind of barred or spiral structure. Very red and small (background?) galaxy is observed to the north-west. Radio emission is only found in the main galaxy. The luminosity profile clearly shows a disk and a prominent bulge.

No. 59, M?. Blue irregular galaxy with extended Hα emission. The luminosity profile clearly shows a disk and a bulge.

No. 60, E/S0? pec. Early-type galaxy with concentrated Hα emission showing an AGN-type spectrum. The luminosity profile clearly shows a disk and a bulge.

No. 61, SABc(s?). Barred spiral galaxy with many blue HII regions clearly present in the Hα image. The MgIb (λ5180 Å) absorption line and TiO (λ6200 Å) absorption band are present in the spectrum.

No. 62, Spec. Highly inclined galaxy with very strong Hα emission in the nucleus.

6. The L_{FIR}/L_B selection criterion revisited

The final L_{FIR}/L_B^0 luminosity ratios for the extreme subsample (see Tab. 6) have been calculated using co-added

60 and 100 μm flux densities (see Sect. 3), more precise determinations of galactic extinction and $B-$band magnitudes determined from CCD observations (Sect. 5.2), so that we may expect that they are much more accurate than the originally estimated values used for the selection of our sample (Sect. 2). The co-added IRAS flux densities are in good agreement with originally used IPSC values (see Sect. 3). The galactic extinction corrections of Eq. (3) appear to overestimate the values given by Burstein & heiles (1982) by on average 0.15 mag in the $B-$band. However, the main difference is due to the improved accuracy of the $B-$band magnitudes. In Figure 8a we show the distribution of the errors in the originally adopted magnitudes. Apparently, the $B-$band magnitudes have originally been underestimated by about 0.6 magnitudes, while the error distribution has a dispersion of 0.6 mag. Both the spread and the offset affects the selection criterion. The distribution of the differences between the reddening corrected $\log\left(L_{FIR}/L_B^0\right)$ ratios taken from Section 2 and 5.2 are shown in Figure 8b. It can be approximated by a Gaussian distribution with a spread of ±0.24 and an average offset implies that the original selection criterion $L_{FIR}/L_B^0 > 4.3$ is actually $L_{FIR}/L_B^0 > 3.0$ and the spread in the distribution implies that the actual L_{FIR}/L_B selection criterion is less sharp. This is illustrated by Figure 9, where we show which fraction of the far-infrared complete sample is included in the extreme subsample as a function of the measured $\log\left(L_{FIR}/L_B^0\right)$. The curve in Figure 9 corresponds to the Gaussian fit in Figure 8b.

Therefore we conclude that we have selected all sources with $L_{FIR}/L_B^0 > 10$, but that the selection is progressively incomplete below this value with a completeness of 50% at $L_{FIR}/L_B^0 = 3.0$.

Acknowledgements.

We wish to thank M.A.T. Groenewegen and A.M. van Genderen for their help with the observations, and the Infrared Processing and Analysis Center in Pasadena for providing us with co-added flux densities.
We have made use of the NASA/IPAC Extragalactic Database (NED), which is operated by the Jet Propulsion Laboratory, California Institute of technology, under contract with the U.S. National Aeronautics and Space Administration.
A.C. van den Broek has been supported by the Netherlands Organization for the Advancement of research NWO/ ASTRON under contract no. 782-373-032.

References

Arp H.C., Madore B.F. 1987, A Catalogue of Southern peculiar galaxies and Associations (Cambridge Univ. Press)
Bessel M.S. 1979, PASP 91, 589
Bergvall N., Olofsson K. 1986, A&AS 64, 469
Burstein D., Heiles C. 1982, AJ 87, 1165
Carico D.P., Soifer B.T., Beichman C., Elias J.H., Matthews K., Neugebauer G. 1986, AJ 92, 1254
Carico D.P., Sanders D.B., Soifer B.T., Elias J.H., Matthews K., Neugebauer G. 1988, AJ 95, 356
Da Costa L.N., Pellegrini P.S., Willmer C., De Carvalha R., Maia M., Latham D.W., Geargy J.C. 1989, AJ 97, 315
Da Costa L.N., Numes M.A., Pellegrini P.S., Willmer C., Chincarini G.J.J. 1986, AJ 91, 6
de Jong T., Clegg P.E., Soifer B.T., Rowan-Rovinson M., Habing H.J., Houck J.R., Aumann H.H., Raimond E. 1984, ApJ 278, L67
de Jong T., Klein U., Wielebinski R., Wunderlich E. 1985, A&A 147, L6
de Vaucouleurs G., de Vaucouleurs A., Corwin H. 1976, Second Ref. Cat. of Bright Galaxies (Univ. of texas Press) (RC2)
Eales S.A., Wynn-Williams C.G., Beichman C.A. 1988, ApJ 328, 530
Fairall A.P., Vettolani G., Chincarini G. 1989, A&AS 78, 269
Fairall A.P. 1981, MNRAS 196, 417
Fricke K.J., Kollatschny W. 1989, A&AS 77, 75
Graham J.A. 1982, PASP 94, 244
Hamuy M., Maza J. 1987, A&AS 68, 383
IRAS Small Scale Structures Catalogue (ISSSC) 1986, Helou G., Walker D. (GPO, Washington DC)
IRAS Point Source Catalogue (IPSC) 1985, Joint IRAS Science Working Group (GPO, Washington DC)
IRAS Circular no. 14, 1984, A&A 137, C3
IRAS Explanatory Supplement., Joint IRAS Science Working Group (JISWG) (Jet Propuls. Lab., Pasadena).
Johnson H.L. 1966, ARA&A 4, 193
Kollatschny W., Fricke K.J. 1983, A&A 125, 276
Kunth D., Martin J.M., Maurogordatos S., Vigroux L. 1985, in Starforming Dwarf Galaxies and related Objects, Eds. D. Kunth, T.X. Thuan and J. Tran Thank Van (Editions Frontières, France)

Landolt A.U. 1983, AJ 88, 439
Lauberts A. 1982, The ESO/Uppsala Survey of the ESO(B) Atlas, European Southern Obs. (ESO), Munich
Lonsdale C.J., Helou G., Good J.C., Rice W. 1985, Cataloged Galaxies and Quasars Observed in the IRAS Survey (Jet Propuls. Lab., Pasadena)
Lutz D. 1991a, in Dynamics of Galaxies and their Molecular Cloud Distribution, IAU Symp. 146, Eds. F. Combes and F. Casoli (Springer, Heidelberg)
Lutz D. 1991b, A&A 245, 31
Menzies J.W., Coulson I.M., Sargent W.L.M. 1989, AJ 97, 1576
Miller J.S., Mathews W.G. 1972, ApJ 172, 593
Mirabel I.F., Sanders D.B. 1988, ApJ 335, 104
Moorwood A.F.M., Véron-Cetty M.-P., Glass I.S. 1986, A&A 160, 39
Moorwood A.F.M., Véron-Cetty M.-P., Glass I.S. 1987, A&A 184, 63
Peterson C.J. 1986, PASP 98, 1273
Rowan-Robinson M., Crawford J. 1989, MNRAS 238, 523
Rufener F. 1986, ESO mess 44, 32
Rice W., Lonsdale C.J., Soifer B.T., Neugerbauer G., Kopan E.L., lloyd L.A., de Jong T., Habing H.J. 1988, ApJS 68, 91
Sandage A.R. 1961, The Hubble Atlas of Galaxies, Carnegie Institute of Washington Publ. no. 618
Sandage A.R., Tammann G.A. 1981, A Revised Shapley-Ames catalogue of Bright Galaxies, Carnegie Inst. Of Washington (RSA)
Sanders D.B., Scoville N.Z., Young J.S., Soifer B.T., Schloerb F.P., Rice W.L., Danielson G.E. 1986, ApJ 305, L45
Sanders D.B., Soifer B.T., Elias J.H., Madore B.F., Matthews K., Neugebauer G., Scoville N.Z. 1988, ApJ 325, 74
Schweitzer F. 1990, in Dynamics and Interactions of Galaxies, Ed. R.H. Wielen, (Springer, Heidelberg) p.60
Soifer B.T., Rowan-Robinson M., Houck J.R., de Jong T., Neugebauer G., Aumann H.H., Beichman C.A., Boggess N., Clegg P.E., Emerson J.P., Gillett F.C., Habing H.J., Hauser M.G., Low F.J., Miley G., Young E. 1984, ApJ 278, L71
Soifer B.T., Sanders D.B., Madore B.F., Neugebauer G., Danielson G.E., Elias J.H., Lonsdale C.J., Rice W.L. 1987a, ApJ 320, 238
Soifer B.T., Houck J.R., neugebauer G. 1987b, ARA&A 25, 187
van den Broek A.C. 1991, A&A, submitted
van Driel W., van den Broek A.C., de Jong T. 1991, A&AS in press
van Driel W., van den Broek A.C. 1991, A&A in press
Veillieux S., Osterbrock D.E. 1987, ApJS 63, 295
Winkler H. 1988, MNRAS 234, 703

1991A&AS...91...61V

TABLE 1. *Spectra - observation dates, telescopes and detectors.*

Run	Dates		Telescopes	Detectors	Resolution	
					spatial ($'' \text{pixel}^{-1}$)	spectral (Å)
A85	16 Apr–17 Apr	1985	ESO 3.6m	IDS	—	11
A85	17 Apr–19 Apr	1985	ESO 3.6m	CCD	1.1	7
J86	12 Jun–14 Jun	1986	ESO 2.2m	CCD	1.1	7
J87	31 May–6 Jun	1987	ESO 2.2m	CCD	1.7	7
M89	8 May–9 May	1989	ESO 2.2m	CCD	1.7	7

TABLE 2. *Images - observations dates, detectors and filters.*

Run	Dates		Detector RCA CCD	Filters[a] B-band	V-band	R-band
F85	28 Feb–1 Mar	1985	ESO#1(512×320)	B_J	V_J	ESO#346
A85	11 Apr–16 Apr	1985	ESO#1(512×320)	B_J	V_J	ESO#346
J86	6 Jun–11 Jun	1986	ESO#1(512×320)	ESO#450	ESO#451	ESO#452
J87	2 Jun–6 Jun	1987	ESO#3(512×320)	ESO#450	ESO#451	ESO#346
M89	11 Mar–16 Mar	1989	ESO#15(1024×640)	ESO#450	ESO#451	ESO#346
May89	5 May–6 May	1989	ESO#5(512×320)		Hα only	

Note: a ESO#346: Gunn-r, ESO#452: Cousins-R, B_J and ESO#450: Johnson-B, V_J and ESO#451: Johnson-V

TABLE 3a. *IRAS positions, flux densities and optical positions-Field I.*

No.	Object[a]	R.A. (1950.0) Dec. IRAS						$S_{12\mu m}$	$S_{25\mu m}$	$S_{60\mu m}$	$S_{100\mu m}$	R.A. (1950.0) Dec. optical					
		h	m	s	°	′	″	(Jy)	(Jy)	(Jy)	(Jy)	h	m	s	°	′	″
1	E374-IG32 AM1003-333	10	03	54.8	-33	38	43	0.29	1.21	10.08	8.65	10	03	52.3	-33	38	29
2	E435- G41 NGC3125 AM1004-294	10	04	17.4	-29	41	30	0.19	0.73	4.87	6.66	10	04	18.0	-29	41	30
3	—	10	05	46.5	-33	43	25	—	0.44	2.68	3.56	10	05	46.6	-33	43	24
4	—	10	20	11.5	-36	01	54	0.11	0.12	1.44	3.47	10	20	11.4	-36	01	51
5W	E436-IG15 AM1021-282	10	21	56.6	-28	28	31	0.14	0.88	4.90	5.94	10	21	56.6	-28	28	40*
5E												10	21	57.9	-28	28	36*
6	E500- G34	10	22	10.0	-23	17	59	0.28	1.19	10.91	15.66	10	22	09.6	-23	17	57
7	E436- G26 AM1026-304	10	26	24.7	-30	46	56	0.19	0.54	2.50	3.32	10	26	24.8	-30	46	55
8	—	10	43	55.0	-28	09	37	0.19	0.13	1.49	2.76	10	43	55.0	-28	09	35
9	—	10	44	50.7	-28	39	25	—	0.37	2.10	3.72	10	44	50.7	-28	39	24
10	E438- G09	11	08	21.5	-28	13	41	0.28	0.62	3.18	4.49	11	08	22.2	-28	13	46
11	E503- G03 NGC3597 AM1112-232	11	12	14.4	-23	27	19	0.56	1.92	13.15	16.22	11	12	14.0	-23	27	19
12NW	E319-IG12	11	16	36.6	-39	43	58	0.13	0.28	2.38	4.35	11	16	35.5	-39	43	48*
12SE												11	16	37.7	-39	44	07*
13	—	11	35	40.6	-32	35	10	—	0.29	3.34	5.15	11	35	41.2	-32	35	11
14	E504- G13	11	40	49.8	-27	19	23	—	0.27	2.63	5.25	11	40	49.8	-27	19	22
15	E320- G30	11	50	40.2	-38	51	10	0.54	2.30	34.00	43.33	11	50	39.8	-38	51	07
16	—	12	03	08.5	-32	16	11	—	0.19	2.95	6.30	12	03	09.0	-32	16	15
17N	E440-IG58 AM1204-314	12	04	17.1	-31	40	19	0.22	0.74	7.57	12.52	12	04	17.0	-31	40	04
17S												12	04	17.2	-31	40	18*
18	E379- G30	12	06	23.9	-36	25	30	0.13	0.43	3.14	5.04	12	06	24.2	-36	25	30
19	E379-IG35 AM1211-341	12	11	02.5	-34	12	55	—	0.21	1.72	2.94	12	11	03.1	-34	12	58
20W	E505-IG30	12	14	22.6	-25	55	55	0.11	0.48	3.63	7.08	12	14	21.1	-25	55	53*
20E	E505-IG31 AM1214-255											12	14	23.9	-25	55	55*
21SW	E380-IG15 AM1217-354	12	17	20.6	-35	41	08	0.14	0.16	2.30	4.37	12	17	19.8	-35	41	28
21NE												12	17	21.0	-35	40	58*

Note: *; presumable IRAS galaxy, based on radio continuum detection

TABLE 3a. *(continued)*

No.	Object[a]	R.A. (1950.0) Dec. IRAS h	m	s	°	′	″	$S_{12\mu m}$ (Jy)	$S_{25\mu m}$ (Jy)	$S_{60\mu m}$ (Jy)	$S_{100\mu m}$ (Jy)	R.A. (1950.0) Dec. optical h	m	s	°	′	″
22	—	12	26	59.6	-39	50	49	—	0.23	2.69	2.92	12	26	59.6	-39	50	48
23S	E506- G15 AM1228-260	12	28	39.1	-26	00	42	0.20	0.64	4.32	6.82	12	28	38.8	-26	01	09
23N												12	28	38.9	-26	00	40*
24SW	E381- G08 IC3639 AM1238-362	12	38	10.2	-36	28	52	0.64	2.30	7.53	11.54	12	38	10.6	-36	28	54*
24NE	—											12	38	16.1	-36	27	28
25	E381- G15	12	41	30.1	-33	52	46	—	0.14	1.43	2.99	12	41	30.3	-33	52	44
26	E575- G10	12	48	56.8	-20	26	15	0.14	0.14	1.43	3.47	12	48	55.7	-20	26	11
27	E443- G17	12	55	02.6	-29	29	51	0.22	0.90	6.07	8.31	12	55	01.9	-29	29	47
28	E507- G70 AM1300-233	13	00	11.1	-23	39	14	0.12	0.78	13.48	14.50	13	00	10.7	-23	39	12
29	E443- G56	13	02	23.5	-31	55	28	0.17	0.31	1.92	4.45	13	02	23.4	-31	55	24
30NW	E382- G10 AM1304-333	13	04	22.5	-33	36	00	0.14	0.55	4.73	7.02	13	04	21.6	-33	35	51*
30SE												13	04	22.9	-33	36	01*
31	E508- G33	13	13	38.5	-26	17	51	0.09	0.37	2.37	3.49	13	13	38.8	-26	17	51
32	E382- G46	13	18	05.0	-34	34	39	—	0.29	2.82	4.26	13	18	05.0	-34	34	36
33S	—	13	18	07.4	-31	28	44	—	0.19	1.56	2.80	13	18	06.9	-31	28	51*
33N												13	18	07.7	-31	28	17*
34	AM1319-392	13	19	45.2	-39	28	24	0.13	0.46	2.71	3.07	13	19	44.0	-39	28	15
35	—	13	20	15.6	-29	38	54	—	0.28	1.70	2.59	13	20	17.9	-29	39	06
36	—	13	22	30.3	-26	14	11	—	0.39	2.45	2.88	13	22	30.7	-26	14	14
37	E576- G64	13	27	00.9	-20	55	31	0.14	0.28	2.50	3.74	13	27	01.3	-20	55	27
38W	—	13	28	34.8	-32	29	17	—	0.22	1.55	2.89	13	28	33.3	-32	29	07
38E												13	28	33.9	-32	29	08*
39	E509- G54 IC4280 AM1330-235	13	30	07.9	-23	57	04	0.41	0.68	6.28	11.71	13	30	08.0	-23	57	02
40	—	13	31	47.6	-33	12	08	0.14	0.29	2.13	3.24	13	31	48.1	-33	12	09
41S	—	13	45	28.8	-29	56	59	—	0.13	2.50	3.20	13	45	28.3	-29	57	06
41N												13	45	28.3	-29	56	59*
42	—	13	56	19.7	-33	58	51	—	0.19	1.79	3.06	13	56	20.0	-33	58	46

Note: *; presumable IRAS galaxy, based on radio continuum detection

TABLE 3b. *IRAS positions, flux densities and optical positions-Field II.*

No.	Object[a]	R.A. (1950.0) Dec. IRAS h	m	s	°	′	″	$S_{12\mu m}$ (Jy)	$S_{25\mu m}$ (Jy)	$S_{60\mu m}$ (Jy)	$S_{100\mu m}$ (Jy)	R.A. (1950.0) Dec. optical h	m	s	°	′	″
43W	—	20	01	04.4	-23	52	25	—	0.21	3.63	4.99	20	01	02.7	-23	52	17
43E												20	01	04.2	-23	52	25*
44	E527-IG07 AM2001-263	20	01	28.7	-26	34	14	—	0.21	2.03	4.26						
45	—	20	03	22.3	-28	03	19	0.13	0.23	1.75	2.69						
46	—	20	10	17.4	-24	54	12	0.11	—	1.70	3.55						
47W	E596-IG05 AM2010-215	20	10	28.5	-21	57	33	—	—	2.03	3.42	20	10	24.2	-21	57	34*
47SW												20	10	28.8	-21	57	43
47NE												20	10	29.8	-21	57	27*
48	E596- G27	20	20	22.2	-21	20	52	0.13	0.28	2.28	4.78						
49	E463-IG03 AM2030-303	20	30	52.4	-30	32	53	0.10	0.14	1.21	2.69						
50	—	20	34	34.9	-31	25	49	0.11	0.26	2.13	4.07						
51	—	20	40	49.8	-33	37	10	—	0.24	1.94	3.18						
52	E401- G14 E401- G15	20	47	15.6	-32	59	58	—	0.31	2.12	3.92						
53	—	20	51	01.3	-25	30	41	0.13	0.18	2.00	3.53						
54	—	21	01	16.5	-23	38	03	—	0.27	3.15	3.48						
55N	—	21	14	01.0	-39	37	20	0.09	0.12	1.76	3.39	21	13	58.0	-39	37	17*
55S												21	13	58.2	-39	37	39
56	AM2115-272	21	15	08.3	-27	28	42	0.18	0.29	1.86	3.06						
57S	E343-IG13 AM2133-384	21	33	05.6	-38	46	03	0.27	0.86	6.42	9.06	21	33	05.1	-38	46	10*
57N												21	33	05.5	-38	46	01*
58NW	—	21	45	19.7	-35	11	04	0.59	2.17	16.91	25.97	21	45	17.2	-35	10	30
58SE	E403- G32 IC5135 AM2145-351											21	45	19.8	-35	11	03*

Note: *; presumable IRAS galaxy, based on radio continuum detection

TABLE 3c. *IRAS positions, flux densities and optical positions-Miscellaneous.*

No.	Object[a]	R.A. (1950.0) Dec. IRAS						$S_{12\mu m}$	$S_{25\mu m}$	$S_{60\mu m}$	$S_{100\mu m}$	R.A. (1950.0) Dec. optical					
		h	m	s	°	′	″	(Jy)	(Jy)	(Jy)	(Jy)	h	m	s	°	′	″
59	E317- G36 AM1027-393	10	27	20.0	-39	35	05	0.18	0.42	3.94	6.41	10	27	20.3	-39	35	05
60	—	11	46	23.6	-33	04	02	—	0.12	1.01	2.09	11	46	23.0	-33	04	01
61	E574- G29	12	42	13.6	-20	09	10	0.21	0.42	2.76	6.78	12	42	13.5	-20	09	11
62	E507- G37 AM1250-271	12	50	29.3	-27	11	33	0.25	0.67	4.98	7.43	12	50	29.7	-27	11	35

Notes: *; presumable IRAS galaxy, based on radio continuum detection
a E-designation from Lauberts (1982); AM-designation from Arp and Madore (1987)

TABLE 4a. *Spectral parameters-Field I.*

No.	z	$\log\frac{[OIII]}{H\beta}$	$\log\frac{[NII]}{H\alpha}$	$\log\frac{[SII]}{H\alpha}$	$\log\frac{[OI]}{H\alpha}$	$\log\frac{H\alpha}{H\beta}$	A_B[a]	EW_{Na}[b]	FWHM[c]	Class[d]
					Uncertainty					
					Line ratios corrected for reddening					
1	0.0340	0.20	-0.27	-0.47	-1.48	1.31	7.3	3.0	300	HII
		±0.23	±0.02	±0.03	±0.28	±0.20	±1.7	±0.5		
		0.10	-0.28	-0.53	-1.38	0.45				
2	0.0037	0.72	-1.31	-0.95	<-1.96	0.64	1.7	<3.1	<150	HII
		0.01	0.08	0.03		0.02	0.2			
		0.70	-1.32	-0.97		0.45				
3	0.0336	-0.03	-0.03	-0.46	-1.51	1.25	6.8	5.3	300	L[f]
		0.36	0.02	0.04	0.43	0.25	2.1	0.5		
		-0.12	-0.04	-0.52	-1.41	0.49				
4	0.0343	0.05	-0.22	-0.57	<-1.48	1.48	8.8	5.2	300	HII
		0.54	0.02	0.05		0.40	3.5	0.4		
		-0.07	-0.23	-0.64		0.45				
5W*					not observed					
5E*	0.0269	0.36	-0.57	-0.91	-1.50	1.00	4.7	2.5	350	HII
		0.10	0.03	0.07	0.30	0.09	0.8	0.5		
		0.30	-0.57	-0.94	-1.44	0.45				
6	0.0126	0.47	-0.11	-0.46	-1.44	1.26	6.9	4.8	300	L[f]
		0.14	0.01	0.02	0.19	0.13	1.1	0.5		
		0.38	-0.12	-0.51	-1.35	0.49				
7	0.0137	-0.23	-0.19	-0.51	-1.64	1.03	4.9	1.7	300	HII
		0.12	0.01	0.02	0.25	0.06	0.6	0.4		
		-0.29	-0.19	-0.55	-1.57	0.45				
8	0.0123	-0.50	-0.46	-0.54	-1.83	0.88	3.6	1.4	300	HII
		0.08	0.01	0.01	0.24	0.02	0.2	0.4		
		-0.54	-0.47	-0.56	-1.78	0.45				
9	0.0342	-0.48	-0.23	-0.62	-1.70	1.06	5.2	1.6	200	HII
		0.23	0.01	0.02	0.31	0.07	0.6	0.3		
		-0.55	-0.24	-0.66	-1.62	0.45				
10	0.0238	-0.13	-0.74	-1.39	-2.20	0.90	3.8	<1.3	1250[g]	SI
		0.07	0.02	0.13	0.83	0.04	0.4			
		-0.18	-0.74	-1.42	-2.14	0.49				
11	0.0119	-0.20	-0.43	-0.64	-1.81	0.96	4.4	1.8	300	HII
		0.02	0.00	0.00	0.10	0.01	0.1	0.0		
		-0.25	-0.43	-0.67	-1.75	0.45				

TABLE 4a. *(continued)*

No.	z	log $\frac{[OIII]}{H\beta}$	log $\frac{[NII]}{H\alpha}$	log $\frac{[SII]}{H\alpha}$	log $\frac{[OI]}{H\alpha}$	log $\frac{H\alpha}{H\beta}$	$A_B{}^a$	$EW_{Na}{}^b$	FWHM^c	Class^d
				Uncertainty						
				Line ratios corrected for reddening						
12NW*	0.0349	0.25	-0.57	-0.50	-1.50	1.16	6.0	2.0	200	HII
		±0.19	±0.04	±0.03	±0.36	±0.16	±1.4	±1.1		
		0.17	-0.57	-0.55	-1.42	0.45				
12SE*	0.0357	0.80	-0.23	-0.38	-0.99	1.47	8.6	1.6	300	L/SII
		0.41	0.02	0.03	0.13	0.40	3.5	0.5		
		0.69	-0.23	-0.45	-0.87	0.49				
13	0.0305	-0.05	-0.39	-0.61	-1.47	1.02	4.9	1.4	500	HII
		0.19	0.03	0.05	0.35	0.12	1.1	0.6		
		-0.12	-0.39	-0.65	-1.41	0.45				
14	0.0325	—	0.03	<-0.96	<-0.96	>0.95	>4.2	3.2	350:	L/SII?
			0.06					0.5		
15	0.0100	-0.78	-0.30	-0.69	-1.77	1.01	4.7	6.4	300	HII
		0.40	0.01	0.03	0.37	0.06	0.6	0.3		
		-0.84	-0.31	-0.73	-1.71	0.45				
16	0.0390	>0.48	0.14	-0.30	<-0.89	>0.88	>3.7	5.3	350	L/SII
			0.06	0.12				0.9		
17N	0.0239	0.01	-0.44	-0.86	-1.12	0.80	3.0	1.5	300	HII
		0.12	0.04	0.10	0.18	0.09	0.8	0.7		
		-0.02	-0.45		-1.08	0.45				
17S*	0.0238	0.19	-0.22	-0.72	-0.96	1.16	6.0	<1.8	300	L^f
		0.29	0.03	0.09	0.15	0.25	2.1			
		0.11	-0.23	-0.77	-0.88	0.49				
18	0.0130	<-0.31	-0.38	-0.47	<-1.32	1.01	4.7	1.9	250	HII
			0.04	0.06		0.20	1.7	0.8		
			-0.38	-0.51		0.45				
19	0.0088	0.25	-0.70	-0.45	<-1.71	0.78	2.8	3.0	250	HII
		0.05	0.04	0.02		0.04	0.4	4.4		
		0.21	-0.71	-0.48		0.45				
20W*	0.0396	>0.96	0.22	-0.39	-0.95	>0.84	>3.3	6.5	600	SII
			0.06	0.15	0.50			0.5		
20E*	0.0397	-0.10	-0.32	-0.51	<-1.62	1.13	5.8	2.1	350	HII
		0.20	0.02	0.03		0.13	1.1	0.6		
		-0.17	-0.33	-0.56		0.45				
21SW	0.0576	0.96	0.24	0.03	<-0.99	1.05	5.1	3.3	500	SII
		±0.47	±0.04	±0.06		±0.46	±4.0	±0.7		
		0.90	0.23	-0.01		0.49				
21NE*	0.0577	0.09	-0.25	-0.24	-0.93	1.21	6.4	<3.4	300:	L
		0.70	0.06	0.07	0.28	0.55	4.7			
		0.01	-0.25	-0.29	-0.84	0.49				
22	0.0106	—	-0.24	<-0.59	<-0.59	>0.58	>1.1	2.0	200:	HII?
			0.20					0.5		
23S				not observed						
23N*	0.0194	<-0.17	-0.23	-0.75	<-1.31	1.13	5.8	5.5	<150	HII
			0.03	0.11		0.27	2.3	0.9		
			-0.24	-0.79		0.45				
24SW*	0.0112	0.98	-0.16	-0.43	-0.98	1.01	4.7	1.2	350	SII
		0.06	0.01	0.01	0.05	0.06	0.5	0.4		
		0.92	-0.17	-0.46	-0.92	0.49				
24NE	0.0113	-0.02	-0.55	-0.56	<-1.48	0.80	2.9	1.5	200	HII
		0.12	0.04	0.05		0.08	0.7	0.7		
		-0.06	-0.55	-0.59		0.45				
25	0.0205	-0.25	-0.45	-0.64	-1.64	1.03	4.9	2.6	300	HII
		0.24	0.03	0.05	0.48	0.12	1.0	0.6		
		-0.31	-0.45	-0.68	-1.57	0.45				
26	0.0215	>0.06	-0.31	-0.86	<-0.91	>0.90	>3.9	3.9	300:	HII
			0.11	0.35				1.0		
27	0.0100	<-0.39	-0.24	-0.51	-1.35	1.32	7.4	4.0	250	HII
			0.01	0.02	0.17	0.16	1.4	0.2		
			-0.25	-0.57	-1.25	0.45				
28	0.0221	—	-0.14	-0.31	-0.77	>1.22	>6.6	<1.7	300	L/SII
			0.04	0.05	0.14					
29	0.0312	—	-0.31	-0.50	< -1.18	>1.17	>6.1	3.1	350	HII?
			0.05	0.09				0.5		

TABLE 4a. *(continued)*

No.	z	log $\frac{[OIII]}{H\beta}$	log $\frac{[NII]}{H\alpha}$	log $\frac{[SII]}{H\alpha}$	log $\frac{[OI]}{H\alpha}$	log $\frac{H\alpha}{H\beta}$	A_B[a]	EW_{Na}[b]	FWHM[c]	Class[d]
				Uncertainty						
				Line ratios corrected for reddening						
30NW*	0.0302	<-0.39	-0.33	-0.57	<-1.15	1.02	4.8	2.5	<150	HII
			±0.06	±0.11		±0.30	±2.6	±0.7		
			-0.33	-0.61		0.45				
30SE*	0.0305	—	-0.34	-0.62	<-1.05	>1.04	>5.0	<3.8	300	HII?
			0.08	0.15						
31	0.0113	-0.03	-0.55	-0.47	-1.75	0.84	3.3	1.6	250	HII
		0.03	0.01	0.01	0.21	0.02	0.2	0.3		
		-0.08	-0.55	-0.49	-1.71	0.45				
32	0.0262	-0.05	-0.37	-0.82	<-1.26	1.06	5.1	2.7	200	HII
		0.38	0.05	0.15		0.25	2.2	1.0		
		-0.12	-0.38	-0.86		0.45				
33S*	0.0542	<-0.13	-0.20	-0.54	<-1.36	1.22	6.6	6.0	400	HII
			0.03	0.06		0.29	2.5	0.7		
			-0.21	-0.60		0.45				
33N*	0.0535	-0.29	-0.61	-0.60	<-1.23	0.84	3.3	<4.8	400	HII^f
		0.36	0.09	0.10		0.16	1.4			
		-0.33	-0.61	-0.63		0.45				
34	0.0328	0.17	-0.42	-0.49	-1.40	1.21	6.5	2.7	300	HII
		0.10	0.01	0.01	0.13	0.08	0.8	0.5		
		0.09	-0.43	-0.54	-1.30	0.45				
35	0.0340	0.12	-0.27	-0.48	-1.73	1.25	6.8	2.4	200	HII
		0.29	0.02	0.04	0.70	0.23	2.0	0.9		
		0.03	-0.28	-0.54	-1.63	0.45				
36	0.0620	-0.03	-0.49	-0.52	-1.52	0.86	3.5	3.4	300	HII
		0.13	0.03	0.04	0.40	0.09	0.8	1.8		
		-0.08	-0.50	-0.55	-1.47	0.45				
37	0.0185	—	-0.31	-0.48	<-1.22	>1.21	>6.4	3.2	300	HII?
			0.05	0.08				0.6		
38W				not observed						
38E*	0.0549	-0.04	-0.42	-0.42	-1.13	0.96	4.3	4.1	350	HII^f
		0.37	0.07	0.08	0.36	0.25	2.2	1.5		
		-0.10	-0.42	-0.45	-1.07	0.45				
39	0.0168	<-0.44	-0.45	-0.76	-1.52	1.20	6.4	4.0	200	HII
			±0.02	±0.05	±0.29	±0.14	±1.2	±0.3		
			-0.46	-0.81	-1.43	0.45				
40	0.0459	-0.01	-0.38	-0.53	-1.48	1.06	5.2	2.7	300	HII
		0.15	0.02	0.03	0.27	0.10	0.9	0.7		
		-0.08	-0.39	-0.57	-1.41	0.45				
41^e	0.1295	>0.24	-0.13	—	-1.24	>1.25	>6.8	2.7	<350:	L/SII?
			0.03		0.39			0.8		
41S	—	—	—	—	—	—	—	3.6	—	—
								0.8		
41N*	—	>0.39	—	—	—	—	—	<2.3	—	L/SII?
42	0.0129	—	-0.30	-0.54	<-1.13	> 1.12	>5.7	<2.5	300	HII?
			0.06	0.10						

TABLE 4b. *Spectral parameters-Field II.*

No.	z	log $\frac{[OIII]}{H\beta}$	log $\frac{[NII]}{H\alpha}$	log $\frac{[SII]}{H\alpha}$	log $\frac{[OI]}{H\alpha}$	log $\frac{H\alpha}{H\beta}$	A_B^a	EW$_{Na}^b$	FWHM^c	Class^d
					Uncertainty					
					Line ratios corrected for reddening					
43W					not observed					
43E*	0.0505	>0.73	0.31	-0.21	-0.80	>0.96	>4.3	5.6	350	SII
			0.04	0.09	0.27			0.7		
44	0.0354	-0.21	-0.28	-0.49	-1.37	0.98	4.5	2.8	200	HII
		0.39	0.04	0.07	0.51	0.21	1.8	0.6		
		-0.26	-0.29	-0.53	-1.31	0.45				
45	0.0470	-0.15	-0.23	-0.39	-1.50	0.84	3.4	3.5	300	HII^f
		0.13	0.02	0.03	0.35	0.07	0.7	0.5		
		-0.19	-0.23	-0.42	-1.46	0.45				
46					not observed					
47W*	0.0400	—	-0.25	<-0.76	<-0.76	>0.75	>2.6	3.1	350:	HII?
			0.14					0.7		
47SW	0.0402	—	-0.42	-0.29	<-0.85	>0.84	>3.3	<9.9	200:	HII?
			0.15	0.13						
47NE*	0.0402	0.14	-0.40	-0.47	-0.77	0.95	4.2	<3.2	200	L^f
		0.23	0.05	0.06	0.12	0.19	1.6			
		0.08	-0.41	-0.51	-0.71	0.49				
48	0.0261	>0.07	-0.48	<-1.14	-1.02	>1.13	>5.8	3.2	200	HII?
			0.09		0.30			1.4		
49					not observed					
50					not observed					
51					not observed					
52					not observed					
53					not observed					
54					not observed					
55N*	0.0580	-0.28	-0.35	-0.48	-1.53	0.91	3.9	2.9	350	HII
		0.17	0.02	0.03	0.34	0.08	0.7	1.0		
		-0.33	-0.35	-0.51	-1.48	0.45				
55S	0.0586	-0.29	-0.42	-0.48	<-1.26	1.04	5.0	2.4	200	HII
		0.52	0.06	0.07		0.24	2.1	1.2		
		-0.35	-0.42	-0.52		0.45				
56					not observed					
57S*	0.0188	<-0.16	-0.38	-0.55	-1.36	1.18	6.2	<1.4	200	HII
			0.04	0.06	0.42	0.28	2.4			
			-0.39	-0.60	-1.28	0.45				
57N*	0.0193	—	-0.28	-0.46	-0.75	>0.69	>2.1	<2.6	<150:	L/SII?
			0.17	0.25	0.45					
58NW					not observed					
58SE*	0.0159	0.81	-0.12	-0.59	-1.24	1.05	5.1	3.4	600	SII
		0.10	0.01	0.03	0.15	0.10	0.9	0.7		
		0.75	-0.12	-0.63	-1.17	0.49				

TABLE 4c. *Spectral parameters-Miscellaneous.*

No.	z	$\log \frac{[OIII]}{H\beta}$	$\log \frac{[NII]}{H\alpha}$	$\log \frac{[SII]}{H\alpha}$	$\log \frac{[OI]}{H\alpha}$	$\log \frac{H\alpha}{H\beta}$	A_B[a]	EW_{Na}[b]	FWHM[c]	Class[d]
					Uncertainty					
					Line ratios corrected for reddening					
59	0.0155	0.40	-0.58	-0.65	-1.81	0.84	3.3	0.6	<150	HII
		±0.03	±0.01	±0.02	±0.32	±0.03	±0.3	±0.3		
		0.35	-0.58	-0.68	-1.77	0.45				
60	0.0284	—	-0.09	<-0.99	-0.74	>0.98	>4.5	6.2	450:	SII/L?
			0.06		0.23			0.7		
61	0.0208	—	-0.41	<-0.97	<-0.97	>0.96	>4.3	3.0	<150:	HII?
			0.11					0.7		
62	0.0122	0.23	-0.65	-0.67	-1.81	0.72	2.3	<1.9	150	HII
		0.02	0.02	0.02	0.28	0.02	0.2			
		0.20	-0.65	-0.68	-1.78	0.45				

Notes:
a $A_B=8.5\log((H\alpha/H\beta)/\epsilon)$ with $\epsilon=2.85$ for HII galaxies and $\epsilon=3.1$ for active galaxies
b Equivalent width (Å) of the blended NaID lines at 5890Å and 5896Å
c Full Width Half Maximum in km s^{-1}
d L, SI/II and HII corresponds to LINER-, Seyfert I/II- and HII-type spectrum
e Combined spectrum of both galaxies (see also Sect. 5.4)
f Ambiguous
g Permitted lines only

TABLE 5a. *Optical paramleters-Field I.*

No.	E(B-V)	Obs.[a]	B_T^0	$(B-V)_T^0$	$(V-R)_T^0$	$\log(H\alpha)_T^0$ (Wm^{-2})	D_{25} (″)	b/a	class.
1	0.12	M89	14.57	0.48	0.42	-15.8	51	—	M?/CIP
2	0.06	M89	13.28	0.42	0.43	-14.4	62	0.82	*pec*
3	0.12	J86(M89)	15.80	0.89	0.55	-15.3	27	0.76	S0
4	0.06	M89	15.92	0.82	0.64	-15.9	34	0.53	SBb(s)
5[c]	0.06	F85	(14.11)[b]	—	0.66	-15.0	46:	—	CIP
6	0.06	J87	14.21	0.78	0.63	-15.4	71	0.56	SBab(s)
7	0.06	M89	14.72	0.55	0.53	-15.3	41	0.75	SBb(s)
8	0.06	M89	15.48	0.57	—	-15.4:	23	0.72	S0*pec*
9	0.06	M89	14.97:	0.53	0.47	-15.6:	37	0.90	SBbc
10	0.06	A85	14.28	0.57	0.49	-15.1	49	0.78	SBb(s)
11	0.06	M89	13.33	0.55	—	-14.6::	93	—	M
12[c]	0.12	A85(J86)	14.93	0.69	0.54	-15.5			IP
12NW[*]	0.12	A85(J86)	15.91	0.68	0.59	-15.7	39	0.31	
12SE[*]	0.12	A85(J86)	15.49	0.70	0.50	-15.9	23	0.92	
13	0.07	M89	14.88	0.62	0.55	-15.4	41	0.53	*pec*(r)
14	0.09	M89	15.86	0.83	0.53	-16.1	56	0.25	SABa(s)*pec*
15	0.10	A85	13.64	0.85	0.65	-14.9	79	0.73	SBb
16	0.08	J87	16.06	0.87	0.58	-16.0	29	0.85	S0?*pec*
17[c]	0.07	F85	14.48	0.60	0.50	-15.5	62	—	CIP
18	0.08	A85	14.90	0.84	0.61	-15.3	55	0.40	Sb*pec*
19	0.06	M89	13.76	0.32	0.39	-15.0	35	1.00	*pec*
20[c]	0.09	A85(J87)	14.56	0.72	0.49	-15.4			IP
20W[*]	0.09	A85(J87)	15.24	0.85	0.51	-16.0	38	—	
20E[*]	0.09	A85(J87)	15.38	0.55	0.47	-15.6	33	—	
21SW	0.08	A85(J86)	15.99	0.87	0.56	-16.0	32	—	IP
21NE[*]	0.08	A85(J86)	16.47	0.83	0.56	-16.2	23	—	

TABLE 5a. *(continued)*

No.	E(B-V)	Obs.^{a}	B_T^0	$(B-V)_T^0$	$(V-R)_T^0$	$\log(H\alpha)_T^0$ (Wm^{-2})	D_{25} ('')	b/a	class.
22	0.09	J86	17.71	0.88	0.56	-17.4:^{e}	14	0.94	S0?
23S	0.09	M89	17.07	0.52	0.44	-16.0	23	0.50	CIP
23N*	0.09	M89	14.30	0.62	0.50	-15.1	56	0.61	
24SW*	0.06	M89	12.86	0.49	0.50	-14.5	69	0.85	P
24NE	0.06	M89	13.94	0.47	0.47	-15.0	68	0.83	
25	0.08	M89	15.60	0.68	0.63	-15.6	32	0.54	Sb
26	0.04	M89	15.02	0.79	0.66	-15.3	55	0.55	SB0/a*pec*
27	0.09	A85	13.73	0.89	0.53	-15.1	91	0.56	SAB0/a
28	0.09	F85	14.78	0.94	0.58	-15.8	88	—	M?/CIP
29	0.08	M89	14.54	0.74	0.55	-15.4	64	0.58	SBb
30^c	0.06	A85(F85)	14.40	0.66	0.45	-15.8	57	—	CIP
30NW*	0.06	A85(F85)	15.13	0.61	0.48	-15.9			
30SE*	0.06	A85(F85)	16.11	0.80	0.59	-16.2			
31	0.07	J87	14.28	0.65	0.50	-15.3	43	0.76	S0
32	0.07	A85	15.67	0.86	0.58	-15.6	48	0.29	S*pec*
33^c	0.06	J86(J87)	15.60	0.61	0.55	-15.6			I?P
33S*	0.06	J86(J87)	16.87	0.88	0.64	-16.1	16	0.75	
33N*	0.06	J86(J87)	16.00	0.47	0.48	-15.8	26	0.58	
34	0.09	J86	15.79	0.66	0.53	-15.6	33	—	CIP?
35	0.06	M89	15.94:	0.66	0.53	-15.8:	27	0.61	SB0/a:
36	0.06	J86(J87)	16.24	0.58	0.41	-15.7	23	0.75	M?/CIP
37	0.06	M89	14.73	0.73	0.54	-15.6	44	0.84	SBc*pec*
38W	0.07	M89(M90)	18.91	0.62	0.45	—	6		CIP
38E*	0.07	M89(M90)	16.20	0.71	0.58	-15.7	34	0.40	
39	0.06	M89	13.27	0.63	0.56	-14.9	68	0.90	Sc*pec*
40	0.06	A85(J87)	15.60	0.71	0.56	-15.5	31	0.57	SBb:
41^c	0.07	A85(M90)	17.71	1.15	0.52	-17.1	19	—	CIP
41S	0.07	A85(M90)	19.12	1.29	0.63	—			
41N*	0.07	A85(M90)	18.62	0.94	0.51	-17.1			
42	0.07	M89	15.50	0.79	0.54	-15.6	46	0.32	Sc:

TABLE 5b. *Optical parameters-Field II.*

No.	E(B-V)	Obs.^{a}	B_T^0	$(B-V)_T^0$	$(V-R)_T^0$	$\log(H\alpha)_T^0$ (Wm^{-2})	D_{25} ('')	b/a	class.
43W	0.11	J87	17.63	0.76	0.53	—	12	0.71	I?P
43E*	0.11	J87	16.91	1.05	0.65	-16.2	21	0.69	
44					not observed				
45	0.12	J86	16.11	—	—	—	19	0.52	S0/a*pec*
46	0.12	J86	16.02:	—	—	—	23	0.72	*pec*
47W*	0.09	J87	15.90	0.94	0.63	-16.2	43	0.75	CIP
47SW	0.09	J87	16.57	0.55	0.50	-16.2	29	—	
47NE*	0.09	J87	16.66	0.59	0.48	-16.5	16	—	
48					not observed				
49					not observed				
50	0.05	J86	15.86	—	—	—	28	0.76	S0/a*pec*
51	0.04	J86	15.49:	—	—	—	34	0.75	SBa
52					not observed				
53					not observed				
54	0.05	J86	16.84	—	—	—	17	—	CIP
55N*	0.03	J87	16.68	0.65	0.55	-15.8	16	0.77	P
55S	0.03	J87	16.90	0.83	0.60	-16.1	19	0.63	
56					not observed				
57S^c	0.02	J87^d	14.71	0.69	0.52	-15.4	71	—	CIP
58NW	0.00	J87^d	17.03	1.45	0.68	—	26	0.38	SBb*pec*
58SE*	0.00	J87^d	13.06	0.69	0.53	-14.8	94	—	

TABLE 5c. *Optical parameters-Miscellaneous.*

No.	E(B-V)	Obs.^{a}	B_T^0	$(B-V)_T^0$	$(V-R)_T^0$	$\log(H\alpha)_T^0$ (Wm^{-2})	D_{25} ($''$)	b/a	class.
59	0.10	M89	13.19	0.30	0.39	-14.7	74	—	M?
60	0.09	A85(M89)	16.42	0.99	0.66	-16.0	26	0.62	E/SO?*pec*
61	0.03	A85	13.63	0.61	0.52	-15.3	64	0.75	SABc(s?)
62	0.08	A85	14.10	0.56	0.54	-14.8	68	0.34	S*pec*

Notes:
a Observing runs; see Table 1
b Since no B-band data is available, the V-band magnitude is given
c Total system
d Hα observations done on 5/6 May 1989
e Estimated, see Sect. 5.2
M: merger, P: pair, IP: interacting pair, CIP: closely interacting pair

TABLE 6a. *Derived global parameters-Field I.*

No.	D_{25} (kpc)	$L_{H\alpha+[NII]}$ ($L_\odot$) [log]	L_B^0 ($L_\odot$) [log]	L_{FIR}/L_B^0 [log]	L_{FIR} ($L_\odot$) [log]	S_{100}/S_{60} [log]	S_{60}/S_{25} [log]
1	32.5	7.9	10.39	0.98	11.38	-0.07	0.92
2	3.3	7.2	8.75	0.21	8.97	0.13	0.82
3	16.9	8.4	9.89	0.95	10.85	0.12	0.78
4	22.0	7.8	9.86	0.84	10.70	0.38	1.07
5^a	23.1	8.5	$(10.05)^b$	$(0.84)^b$	10.90	0.08	0.74
6	16.0	7.4	9.64	0.94	10.58	0.15	0.96
7	10.2	7.6	9.51	0.49	10.00	0.12	0.66
8	5.0	7.4	9.11	0.63	9.73	0.26	1.05
9	23.9	8.1	10.24	0.57	10.81	0.24	0.75
10	22.0	8.3	10.19	0.43	10.62	0.14	0.71
11	20.0	8.2	9.94	0.65	10.59	0.09	0.83
12NW*	26.0	8.1	9.89	0.60	10.89	0.26	0.92
12SE*	15.3	7.9	10.06				
13	23.6	8.2	10.18	0.71	10.88	0.18	1.06
14	34.6	7.6	9.84	1.04	10.88	0.30	0.98
15	14.0	7.7	9.65	1.19	10.89	0.10	1.16
16	21.6	7.9	9.92	1.18	11.11	0.32	1.19
17^a	27.5	7.9	10.12	0.91	11.03	0.21	1.00
18	13.0	7.6	9.39	0.70	10.09	0.20	0.86
19	5.4	7.5	9.49	-0.01	9.47	0.23	0.91
20W*	28.7	7.9	10.27	0.66	11.19	0.29	0.87
20E*	24.9	8.3	10.21				
21SW	35.3	8.2	10.30	—	—	—	—
21NE*	25.4	8.0	10.11	1.21	11.32	0.27	1.15

TABLE 6a. *(continued)*

No.	D_{25} (kpc)	$L_{H\alpha+[NII]}$ ($L_\odot$) [log]	L_B^0 ($L_\odot$) [log]	L_{FIR}/L_B^0 [log]	L_{FIR} ($L_\odot$) [log]	S_{100}/S_{60} [log]	S_{60}/S_{25} [log]
22	2.7	5.3:	8.08	1.69	9.77	0.03	1.06
23S	8.9	7.2	8.90	—	—	—	—
23N*	20.2	8.1	10.01	0.59	10.60	0.19	0.82
24SW*	14.0	8.2	10.08	0.25	10.33	0.18	0.51
24NE	13.9	7.7	9.65	—	—	—	—
25	12.1	7.7	9.53	0.68	10.22	0.32	1.00
26	22.2	8.0	9.82	0.48	10.30	0.38	1.00
27	16.4	7.5	9.63	0.49	10.12	0.13	0.82
28	36.6	7.6	9.94	1.22	11.16	0.03	1.23
29	38.0	8.3	10.34	0.41	10.74	0.36	0.79
30^a	32.8	7.8	10.37	0.66	11.03	0.17	0.93
31	8.9	7.5	9.53	0.31	9.84	0.16	0.80
32	23.5	7.9	9.73	0.95	10.68	0.17	0.98
33S*	16.5	8.1	9.89	0.66	11.09	0.25	0.91
33N*	26.8	8.4	10.24				
34	20.5	8.1	9.88	0.94	10.82	0.05	0.77
35	17.6	7.9	9.85	0.84	10.69	0.18	0.78
36	27.5	8.6	10.26	1.08	11.34	0.07	0.79
37	15.3	7.6	9.80	0.52	10.32	0.17	0.95
38W	6.3	—	9.09	—	—	—	—
38E*	35.5	8.5	10.17	0.93	11.11	0.27	0.84
39	21.4	8.2	10.30	0.37	10.67	0.27	0.96
40	26.9	8.5	10.26	0.80	11.05	0.18	0.86
41S	47.5	—	9.76	—	—	—	—
41N*		7.8	9.96	2.05	12.01	0.10	1.28
42	10.9	7.3	9.16	0.70	9.87	0.23	0.97

TABLE 6b. *Derived global parameters-Field II.*

No.	D_{25} (kpc)	$L_{H\alpha+[NII]}$ ($L_\odot$) [log]	L_B^0 ($L_\odot$) [log]	L_{FIR}/L_B^0 [log]	L_{FIR} ($L_\odot$) [log]	S_{100}/S_{60} [log]	S_{60}/S_{25} [log]
43W	—	—	—	—	—	—	—
43E*	20.3	7.9	9.83	1.54	11.37	0.13	1.23
44	—	—	—	—	—	0.32	0.99
45	17.8	—	10.09	0.92	11.01	0.18	0.88
46	—	—	—	0.92	—	0.31	—
47W*	33.8	7.7	10.04	—	—	—	—
47SW	22.8	7.7	9.77	—	—	—	—
47NE*	12.6	7.4	9.74	1.22	10.96	0.22	—
48	—	—	—	—	—	0.32	0.91
49	—	—	—	—	—	0.35	0.94
50	—	—	—	0.94	—	0.28	0.91
51	—	—	—	0.73	—	0.21	0.90
52	—	—	—	—	—	0.27	0.83
53	—	—	—	—	—	0.25	1.05
54	—	—	—	1.42	—	0.04	1.06
55N*	18.0	8.4	10.04	1.19	11.23	0.28	1.16
55S	21.4	8.1	9.95	—	—	—	—
56	—	—	—	—	—	0.22	0.81
57^a	26.4	7.9	9.86	0.91	10.77	0.14	0.87
58NW	—	—	—	—	—	—	—
58SE*	29.1	8.3	10.37	0.68	11.05	0.18	0.89

TABLE 6c. *Derived global parameters-Miscellaneous.*

No.	D_{25} (kpc)	$L_{H\alpha+[NII]}$ ($L_\odot$) [log]	L_B^0 ($L_\odot$) [log]	L_{FIR}/L_B^0 [log]	L_{FIR} ($L_\odot$) [log]	S_{100}/S_{60} [log]	S_{60}/S_{25} [log]
59	20.9	8.3	10.23	0.11	10.34	0.21	0.97
60	13.7	7.6	9.50	0.86	10.35	0.31	0.92
61	25.0	8.0	10.34	0.21	10.55	0.39	0.81
62	15.2	8.0	9.67	0.56	10.23	0.17	0.87

notes: a Total system
b Estimated using B-V=0.8

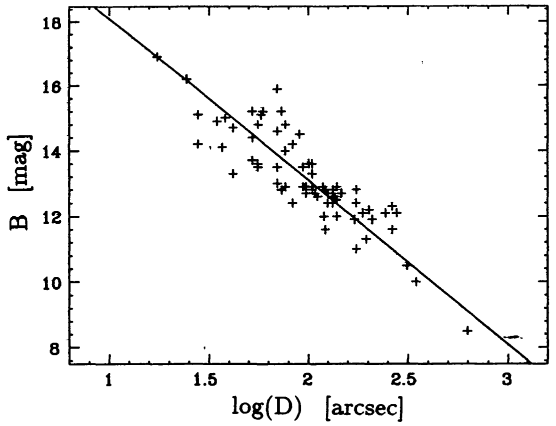

FIGURE 1. B–band magnitudes from Lonsdale *et al.* (1985) for galaxies in our far-infrared complete sample versus optical galaxy diameter in arcseconds, as measured from ESO/SRC and Palomar Observatory Sky Survey plates.

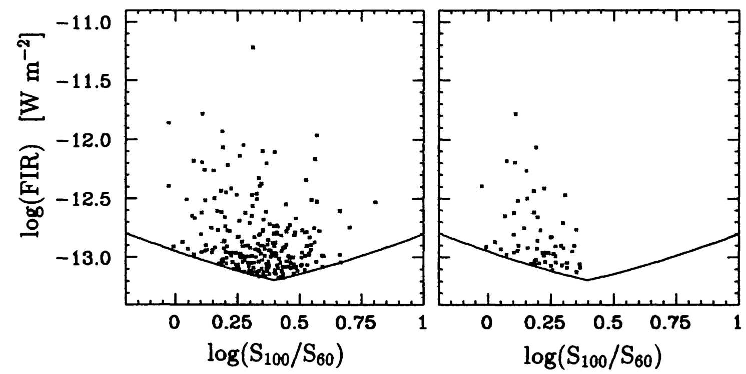

FIGURE 2. The far-infrared flux (FIR) versus the far-infrared colour S_{100}/S_{60} for a) (left) the far-infrared complete sample and b) (right) the extreme subsample. The falling and rising lower envelope curves represent the flux density limits at 100 and 60 μm, respectively.

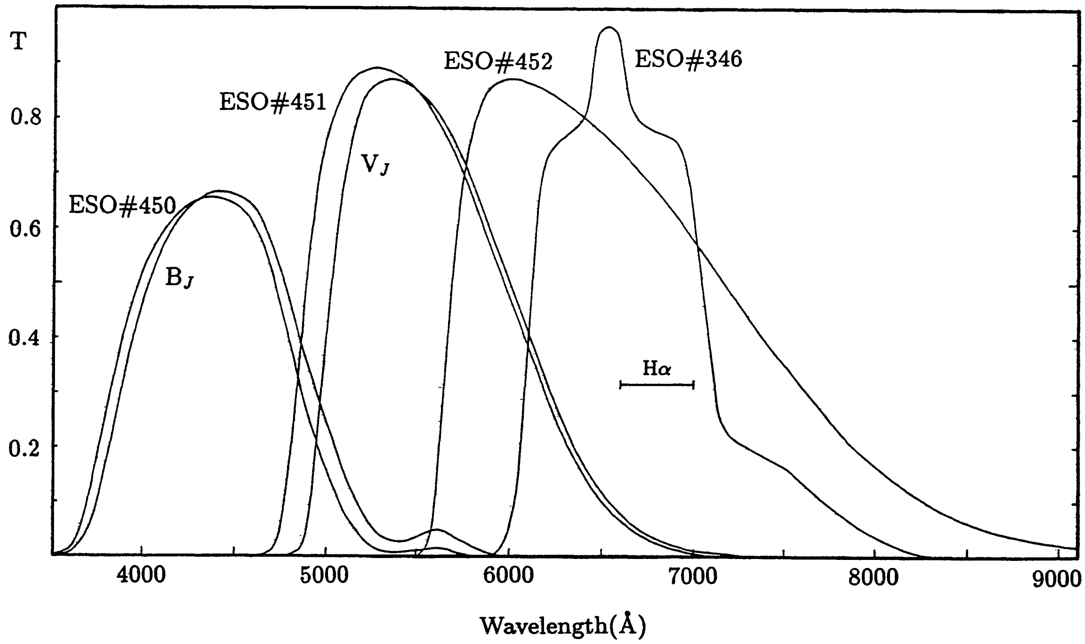

FIGURE 3. Transmission curves of filters used in the observations. The total wavelength range of the Hα filters (FWHM 80Å per filter) is also indicated.

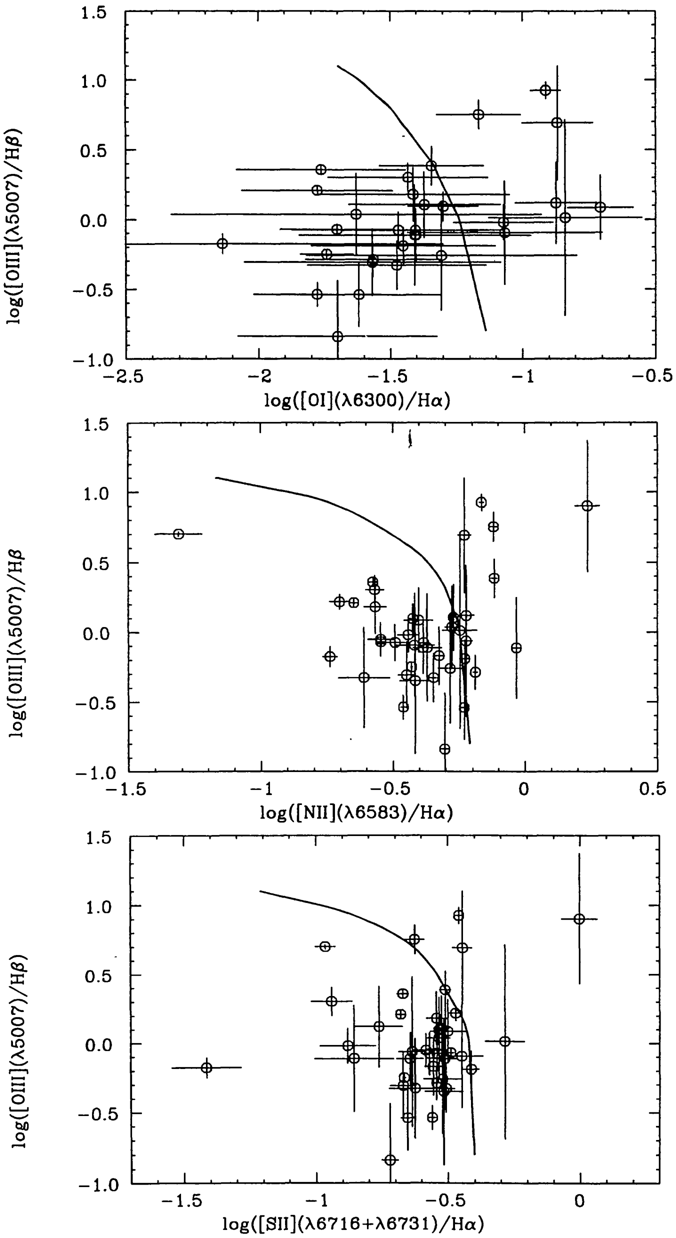

FIGURE 4. Diagnostic diagrams of reddening-corrected emission-line ratios. Uncertainties are indicated by horizontal and vertical bars. The drawn line separates HII-type galaxies (left) from active galaxies (right).

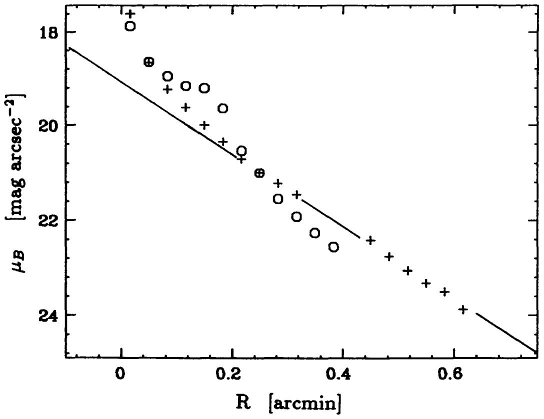

FIGURE 5. Average R−band luminosity profile for the western and eastern half of galaxy No. 2 (indicated as + and o, respectively) derived as described in the text. The line indicates and exponential disk fitted to the data.

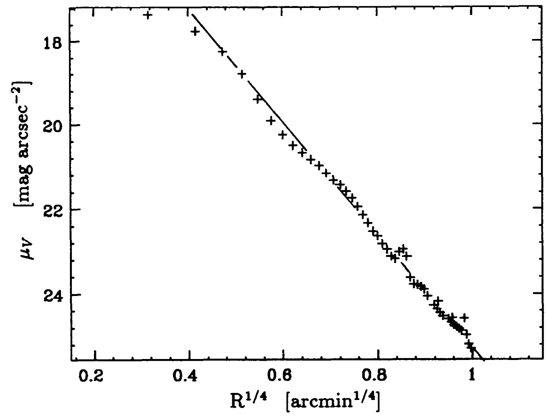

FIGURE 6. Average V−band luminosity profile of galaxy No. 11, derived as described in the text. The line indicate a de Vaucouleurs' $r^{1/4}$ law fitted to the data.

1991A&AS...91...61V

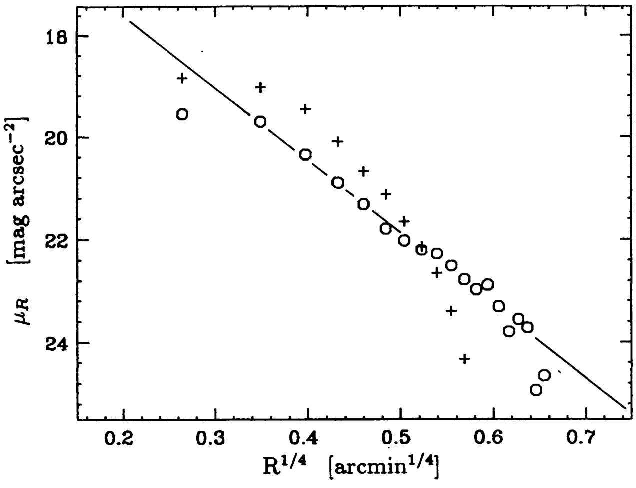

FIGURE 7. Average R–band luminosity profiles of the interacting galaxies No. 41N (+) and 41S (o), derived as described in the text. The dashed line indicates a de Vaucouleurs' $r^{1/4}$–law fitted to the data for No. 41S.

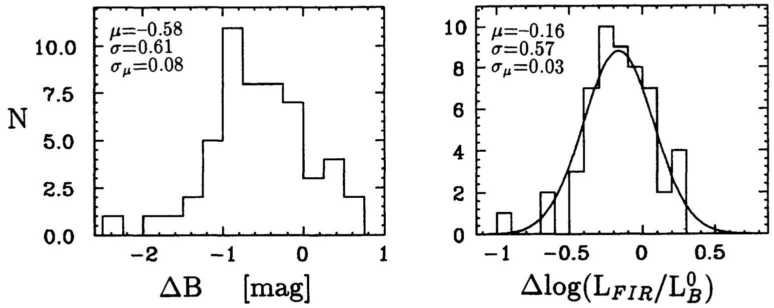

FIGURE 8. a) (left) the difference between the estimated and measured B–band magnitudes; neither have been corrected for galactic foreground extinction. b) (right) Differences between the estimated and measured reddening-corrected log (L_{FIR}/L^0_B) ratios as discussed in Section 2 and 6. A Gaussian curve has been fitted to the data.

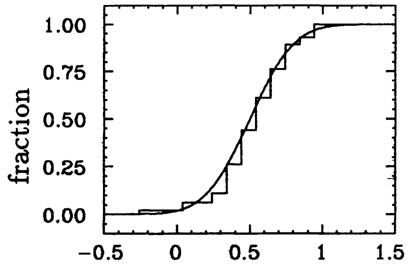

FIGURE 9. The fraction of the far-infrared complete sample which is included in the extreme subsample as a function of log (L_{FIR}/L^0_B), with L^0_B based on the CCD observations presented in Section 5. The smooth curve corresponds to the same Gaussian distribution shown in Figure 8b.

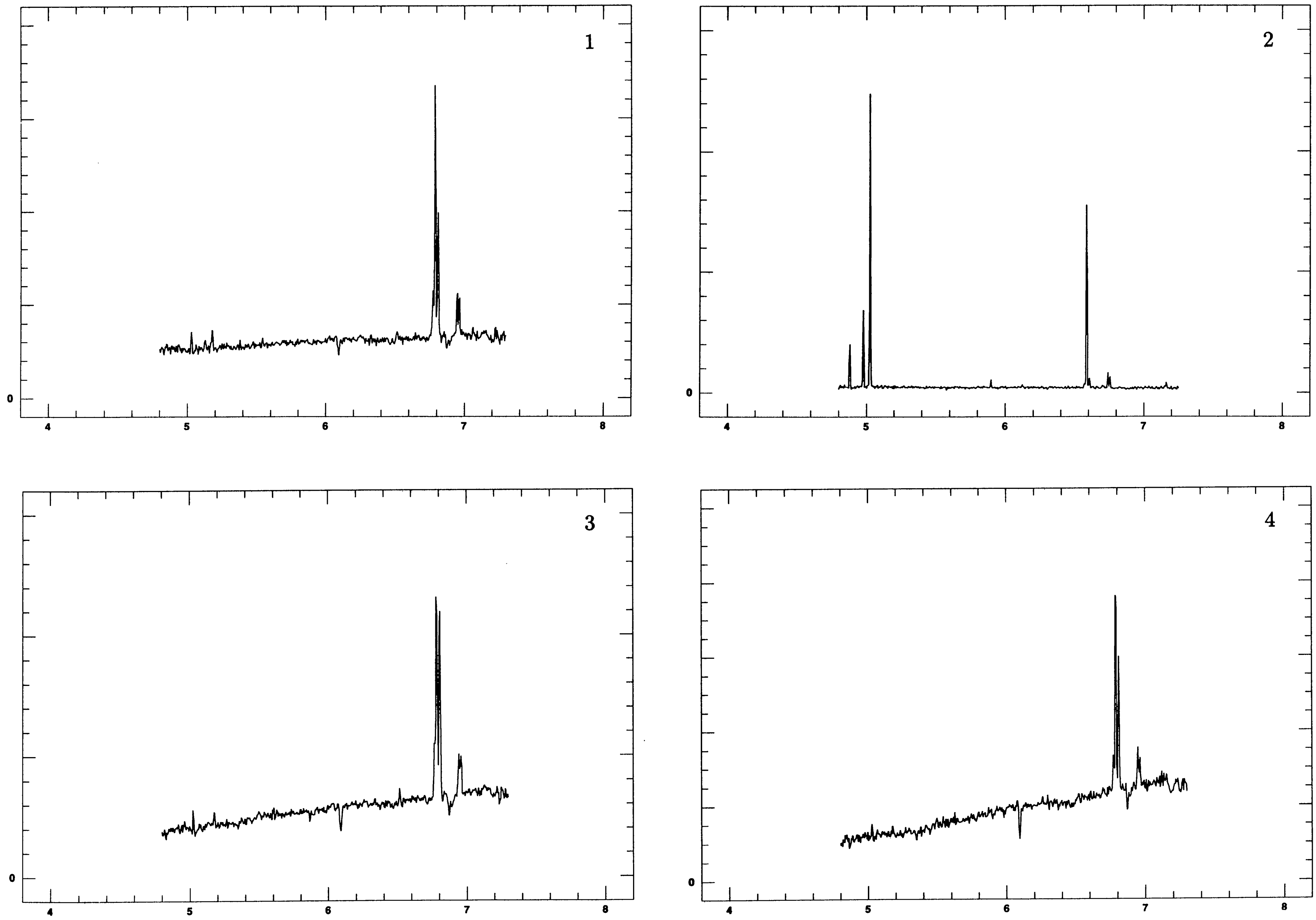

FIGURE 10. Spectra of sources in arbitrary linear intensity units; the zero-level has been indicated. The horizontal axis is wavelength indicated in units of 1000 Å. For source No.41 we show the spectra of the northern and southern galaxy separately, as well as a combined CCD-spectrum to which an IDS-spectrum of the entire system (N + S) has been added, increasing the wavelength range to 7600 Å. The galaxy identification number has been indicated in the upper right-hand corner of each spectrum.

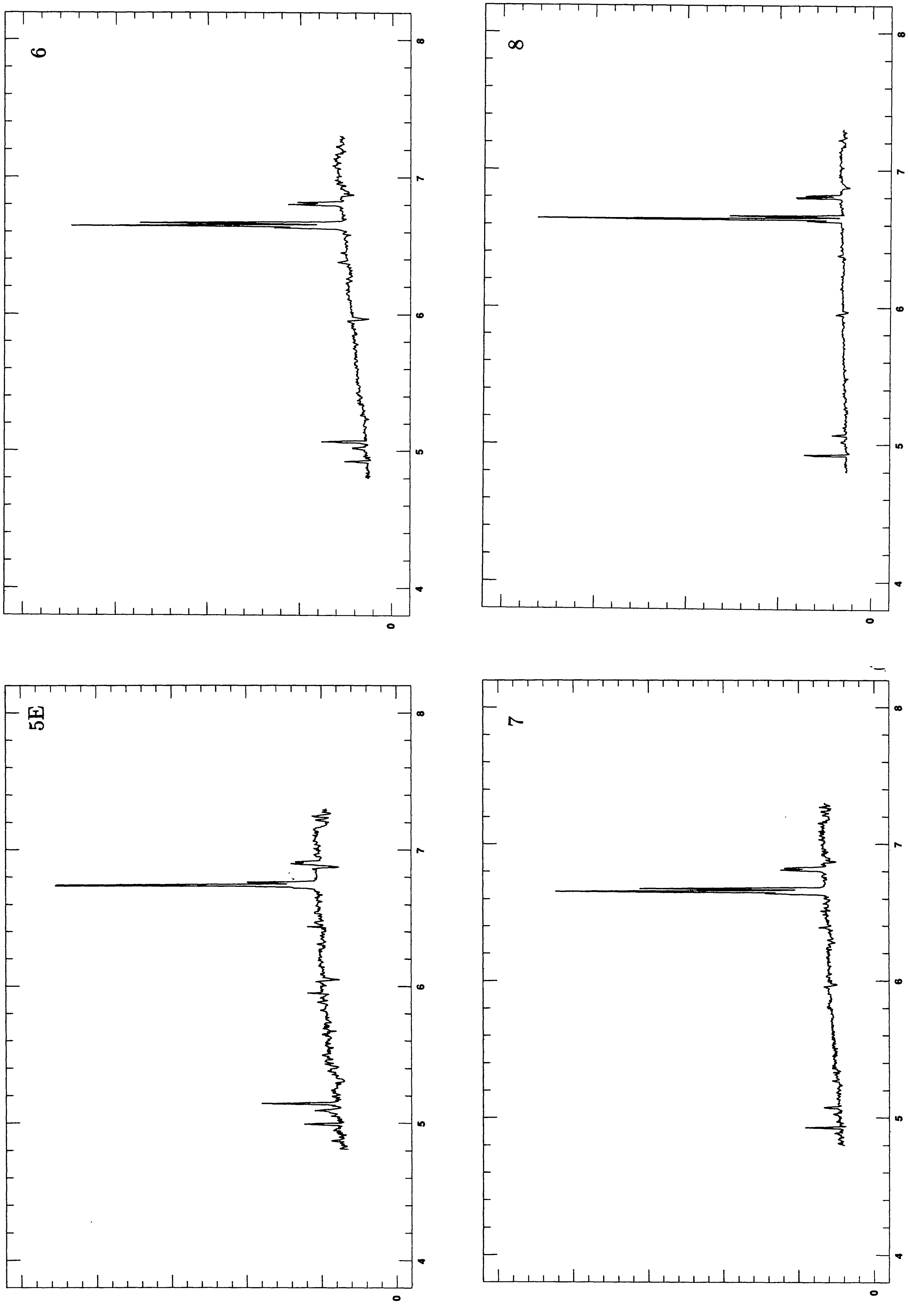

FIGURE 10. *(continued)*

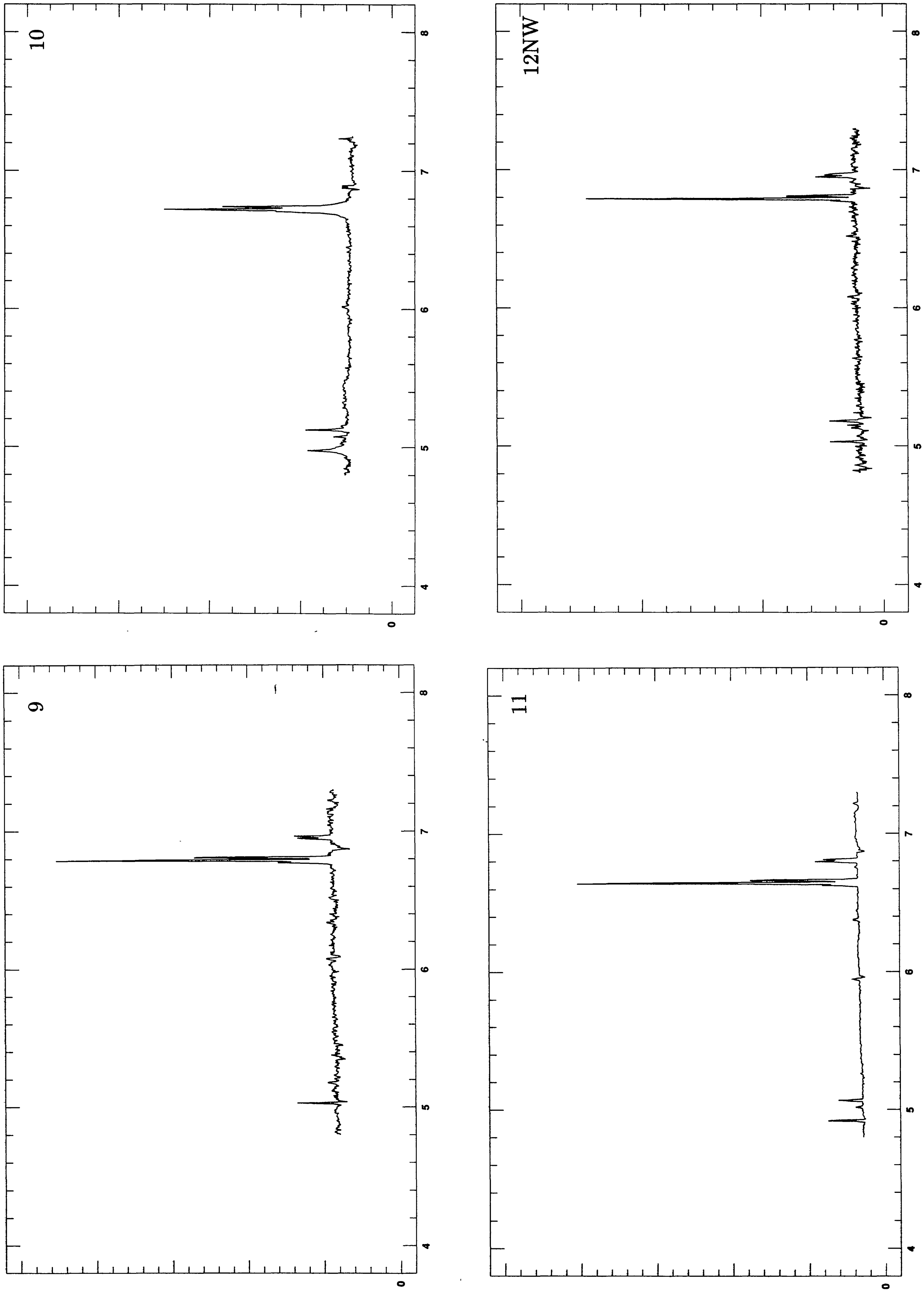

FIGURE 10. *(continued)*

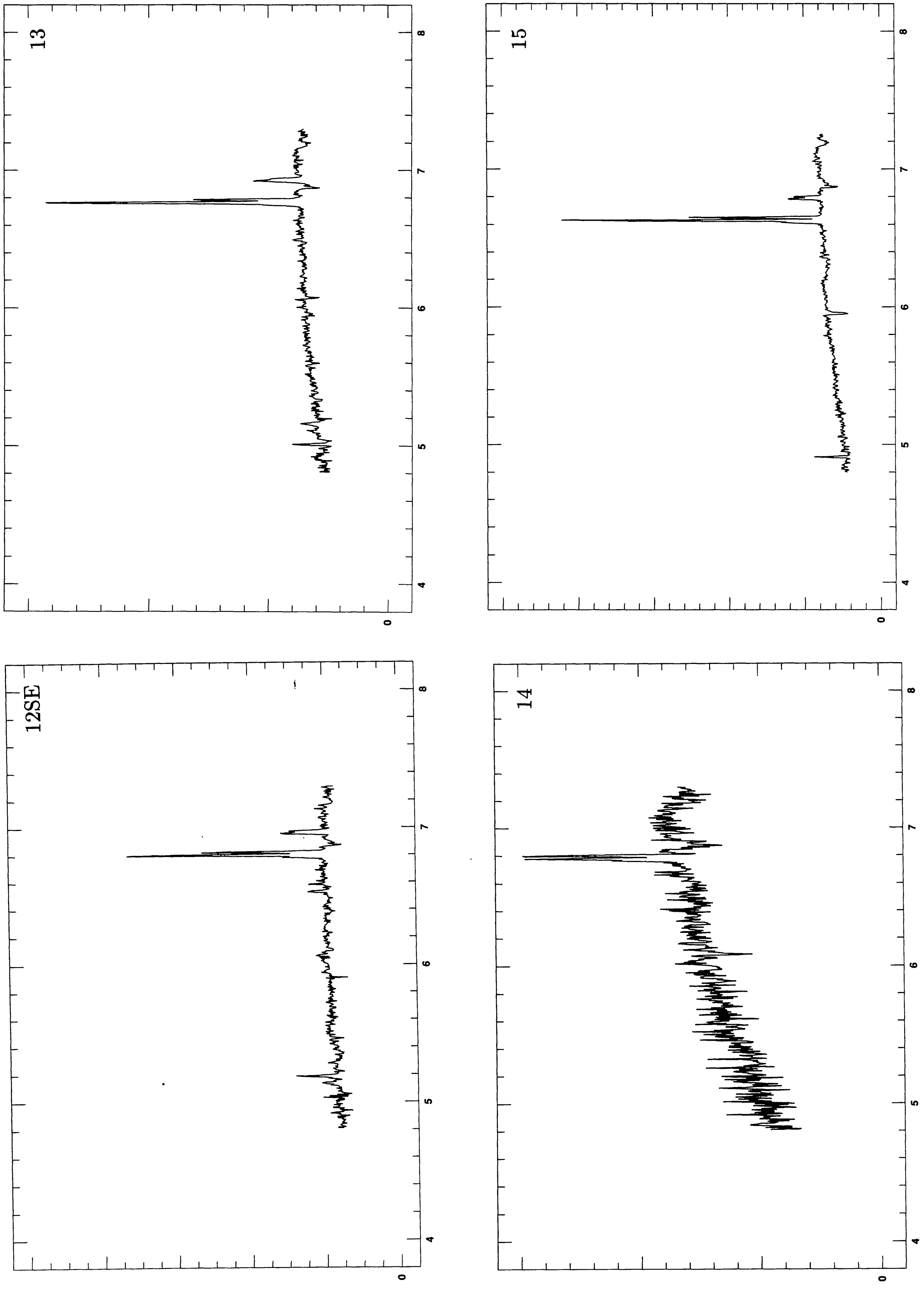

FIGURE 10. *(continued)*

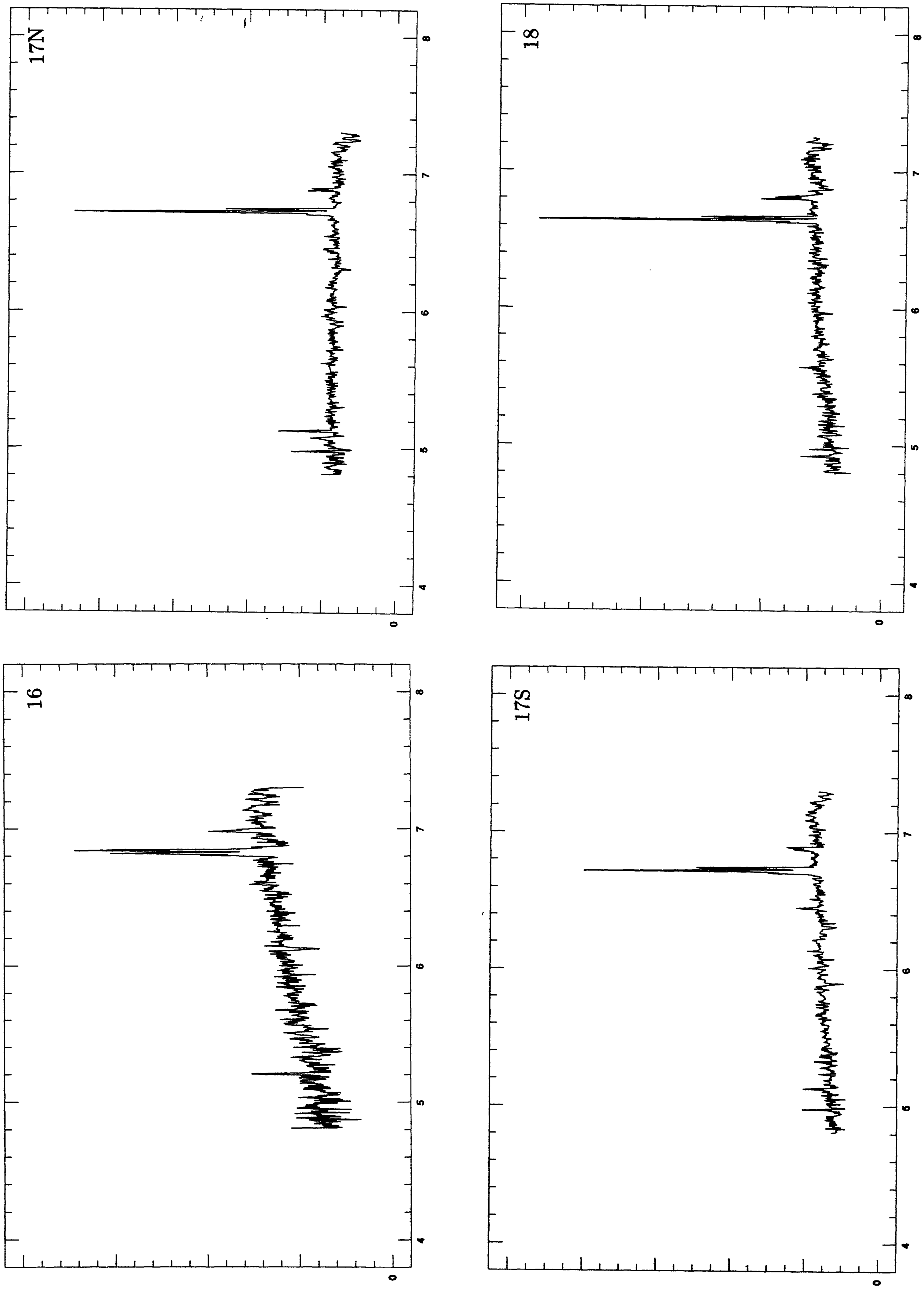

FIGURE 10. *(continued)*

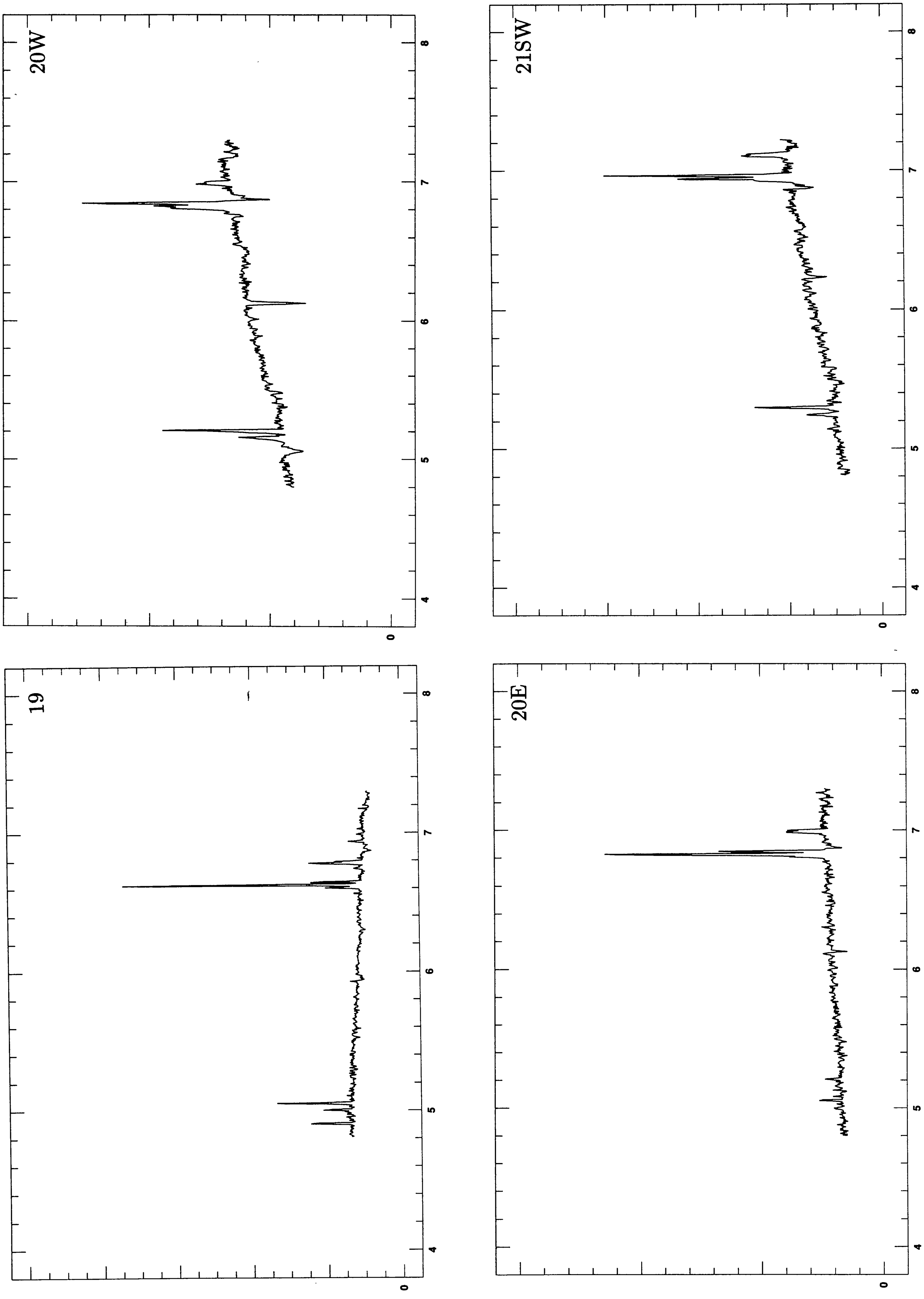

FIGURE 10. *(continued)*

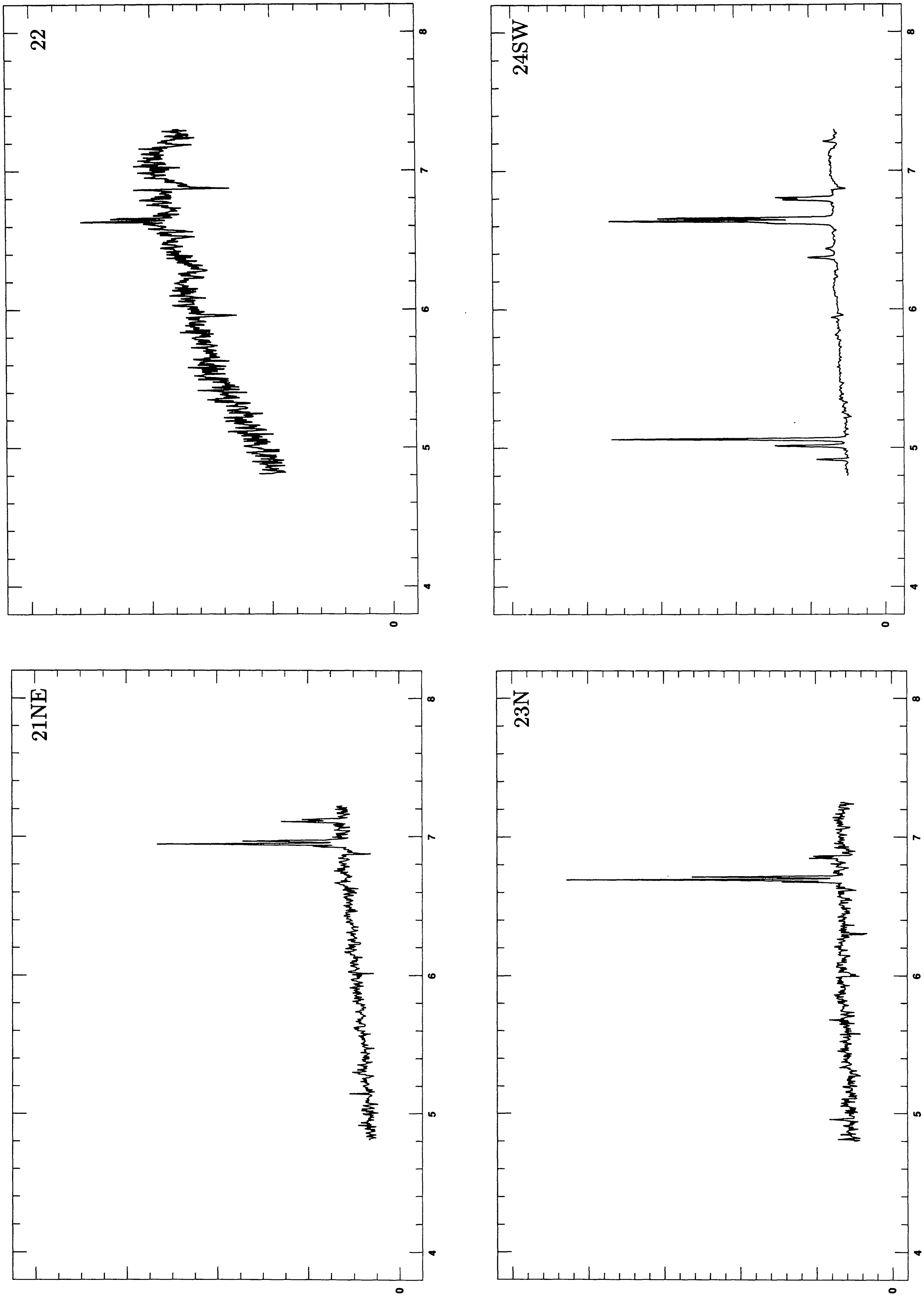

FIGURE 10. *(continued)*

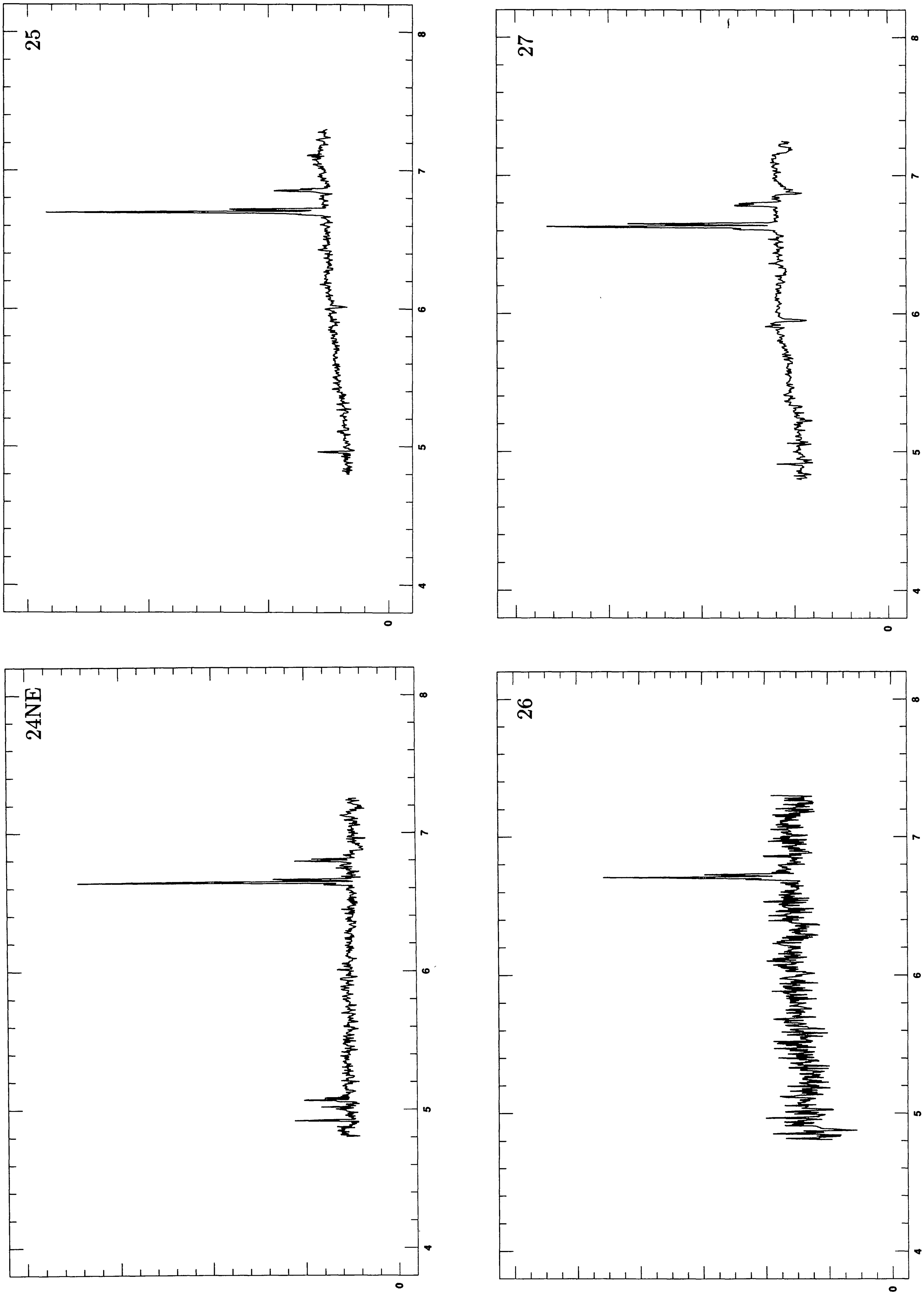

FIGURE 10. *(continued)*

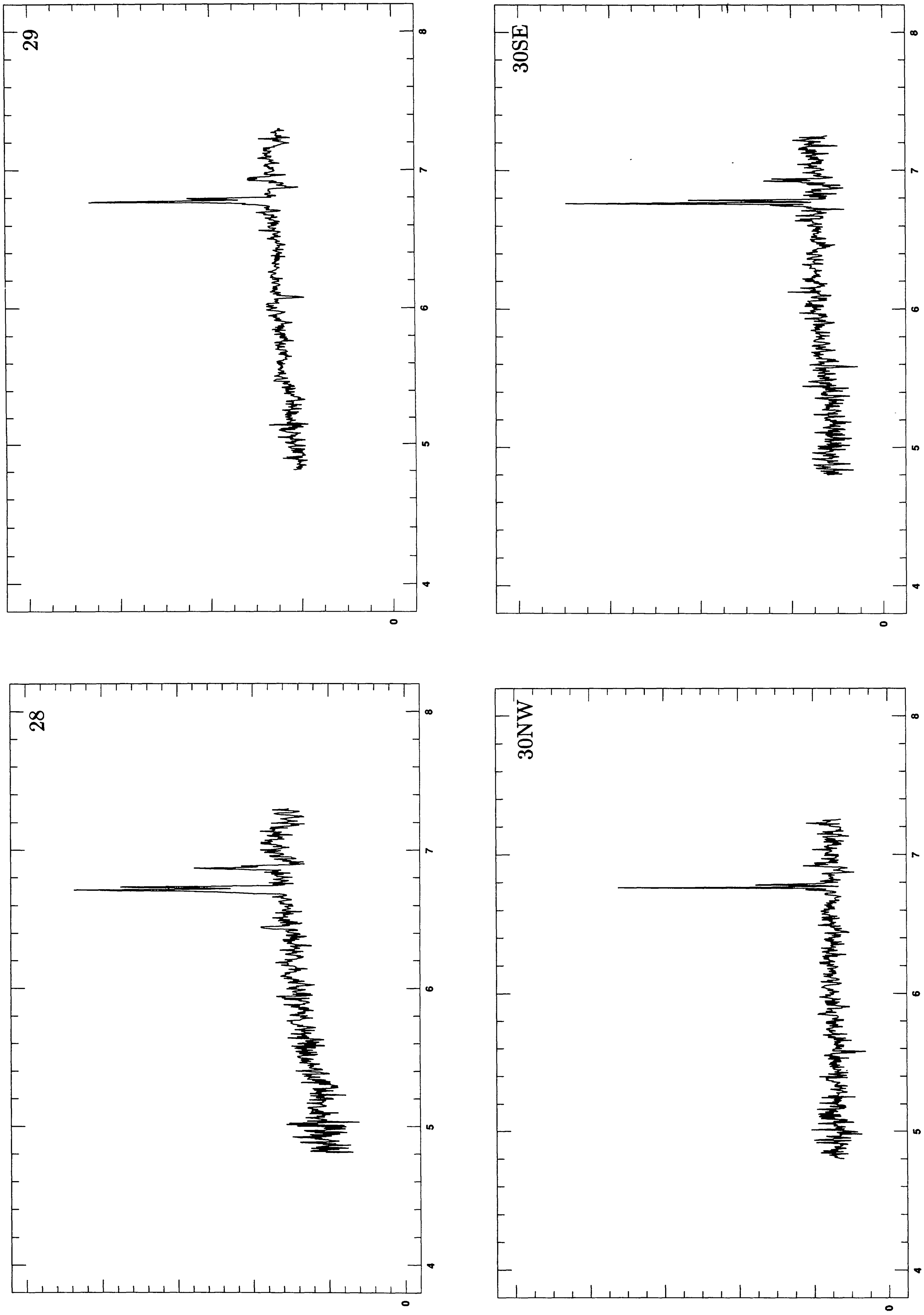

FIGURE 10. *(continued)*

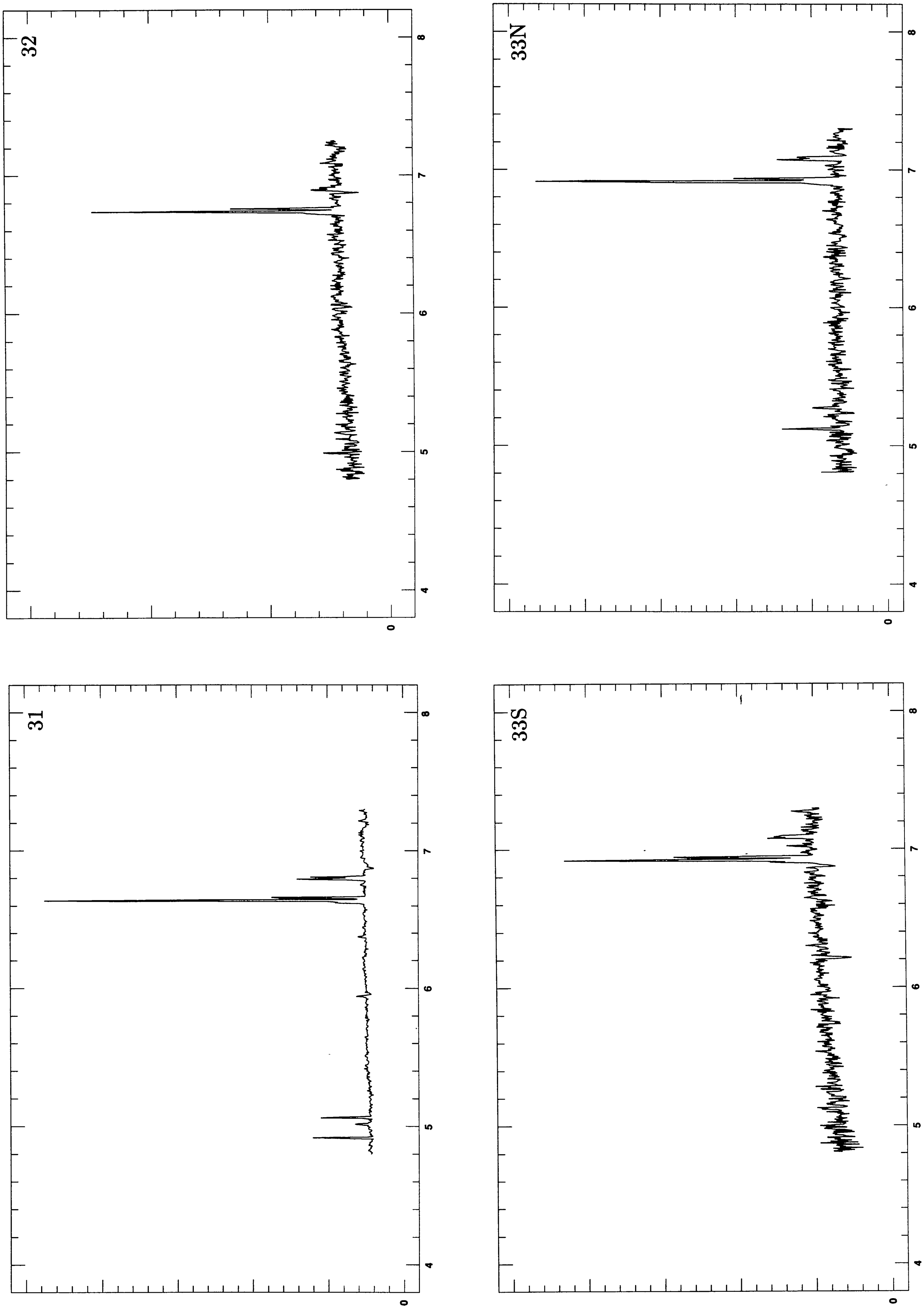

FIGURE 10. *(continued)*

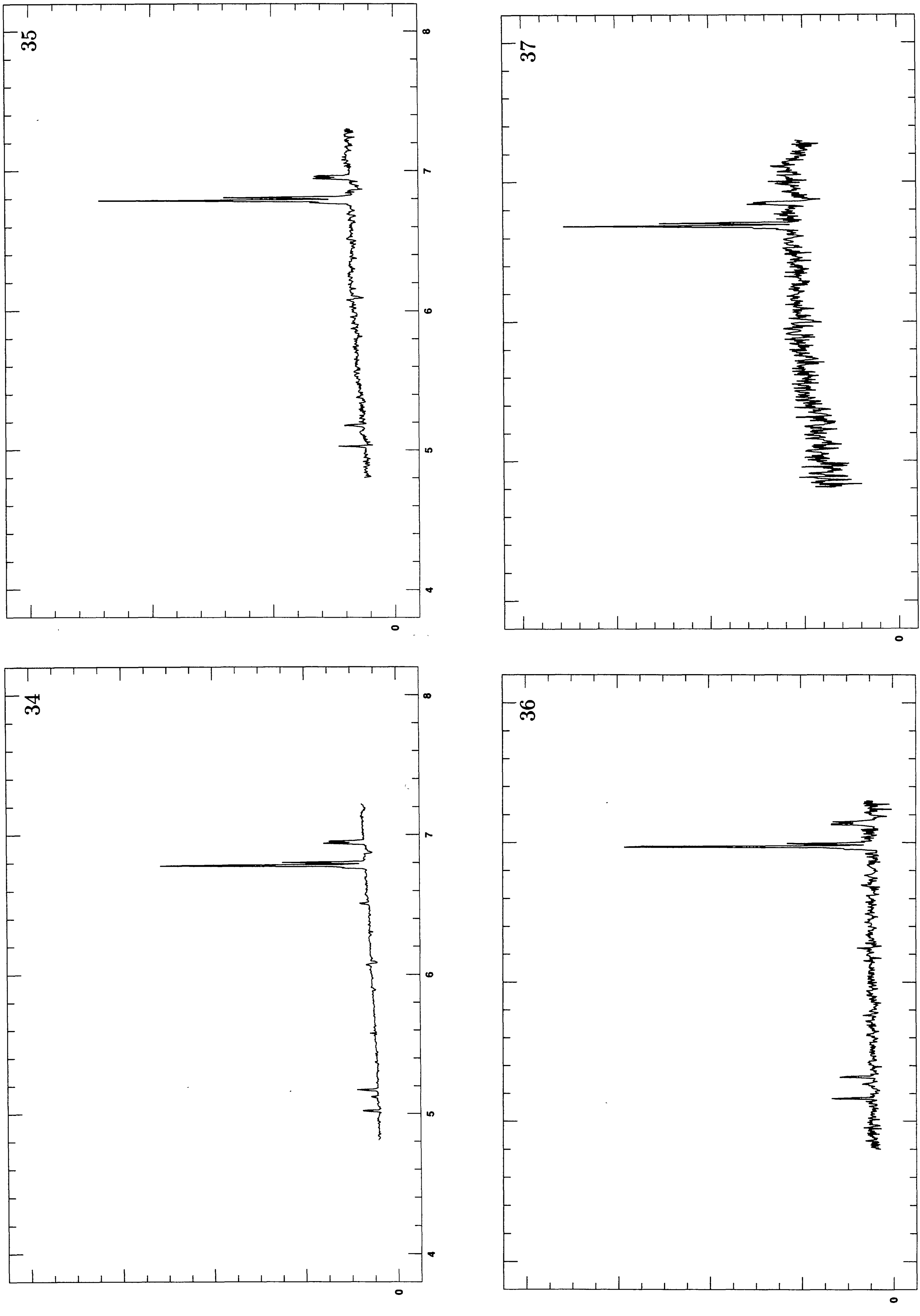

FIGURE 10. *(continued)*

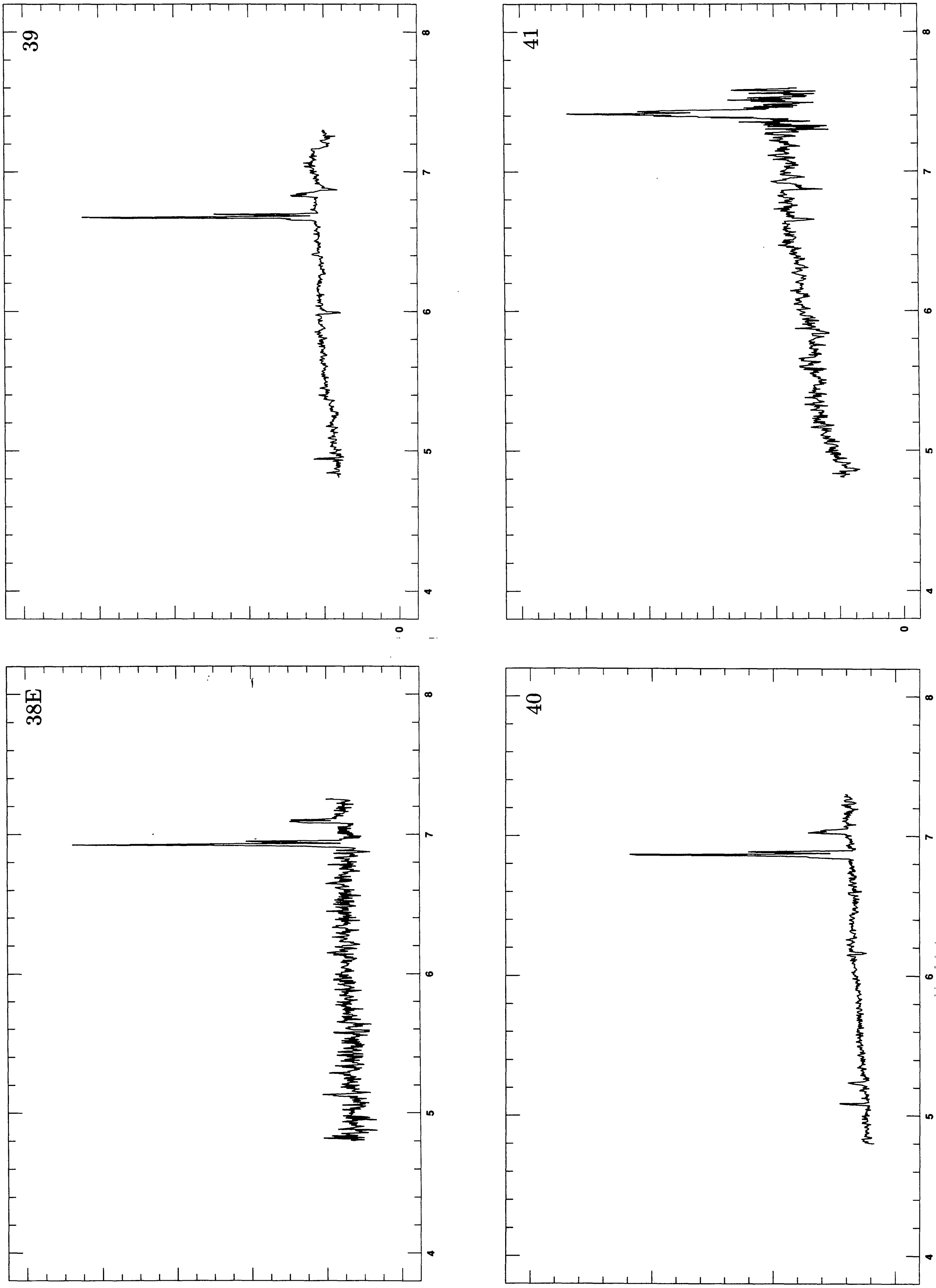

FIGURE 10. *(continued)*

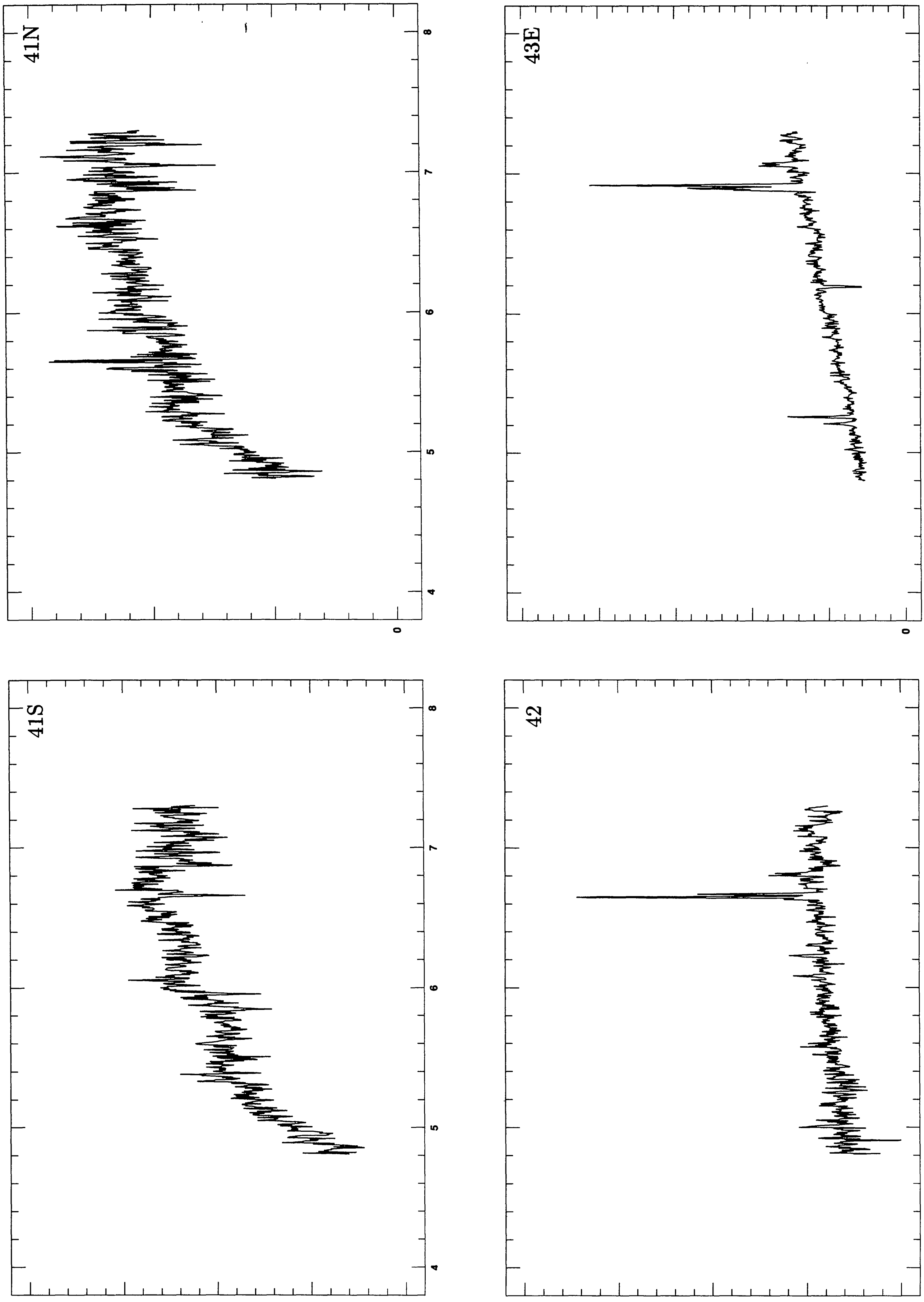

FIGURE 10. *(continued)*

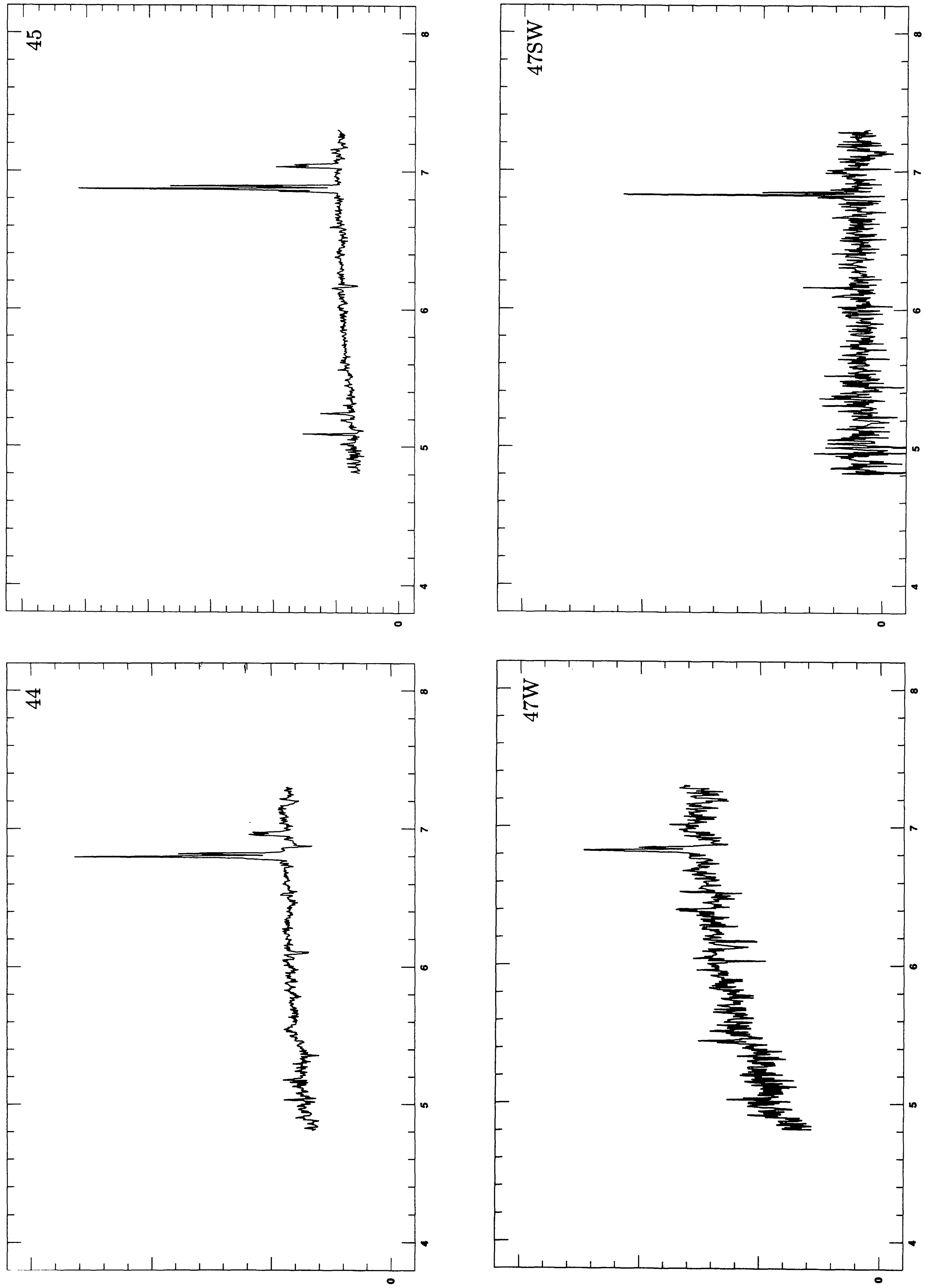

FIGURE 10. *(continued)*

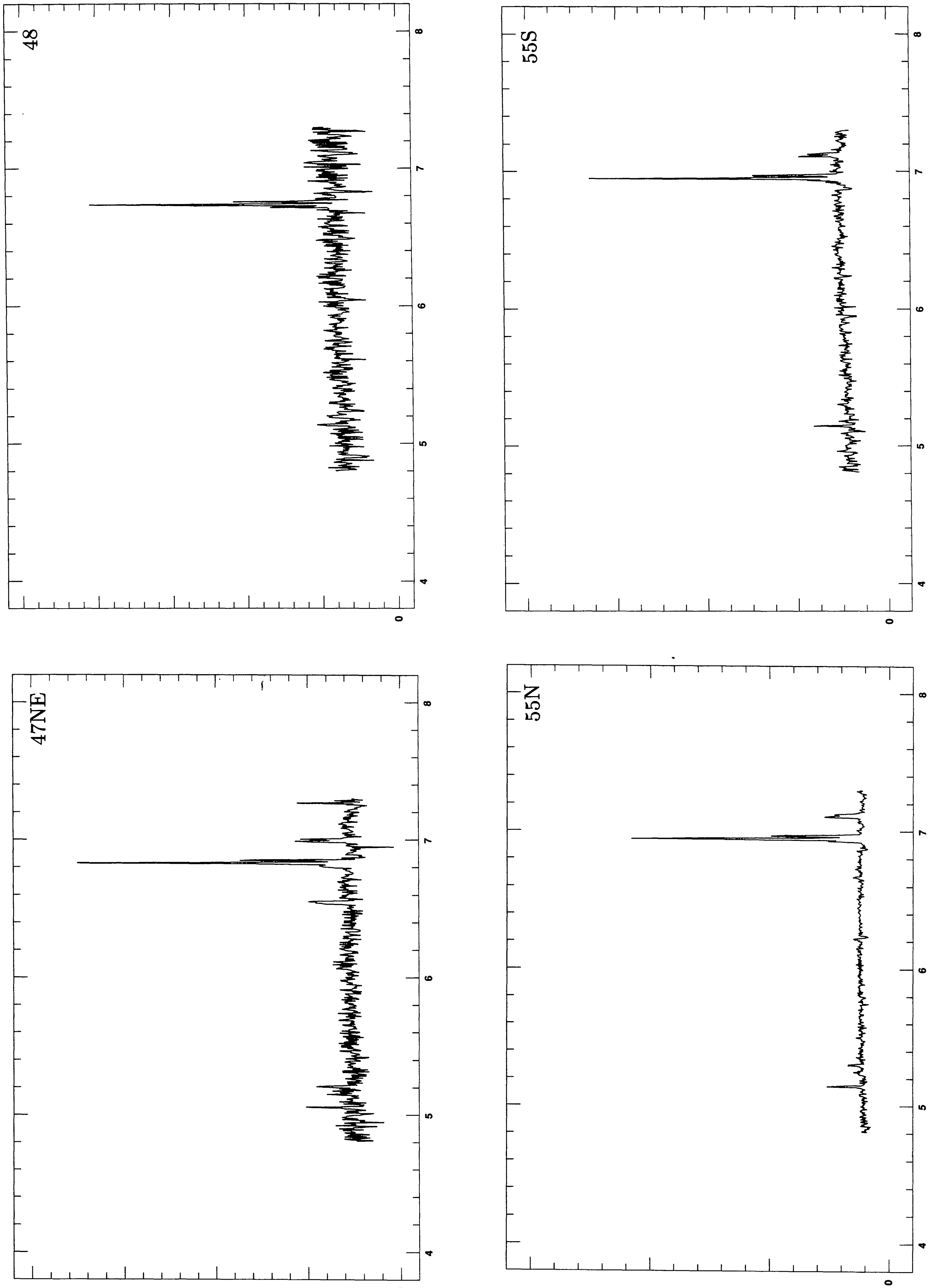

FIGURE 10. *(continued)*

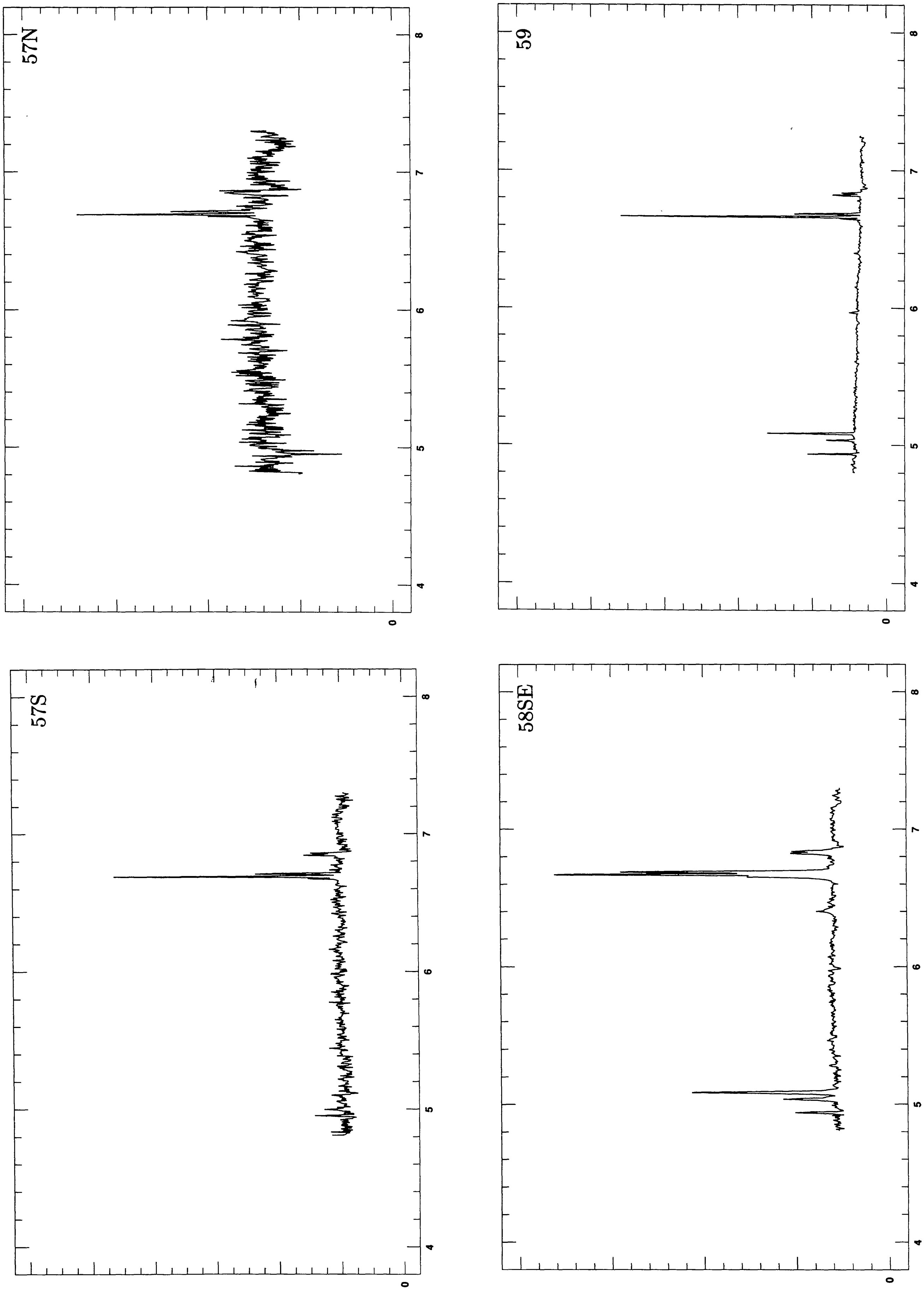

FIGURE 10. *(continued)*

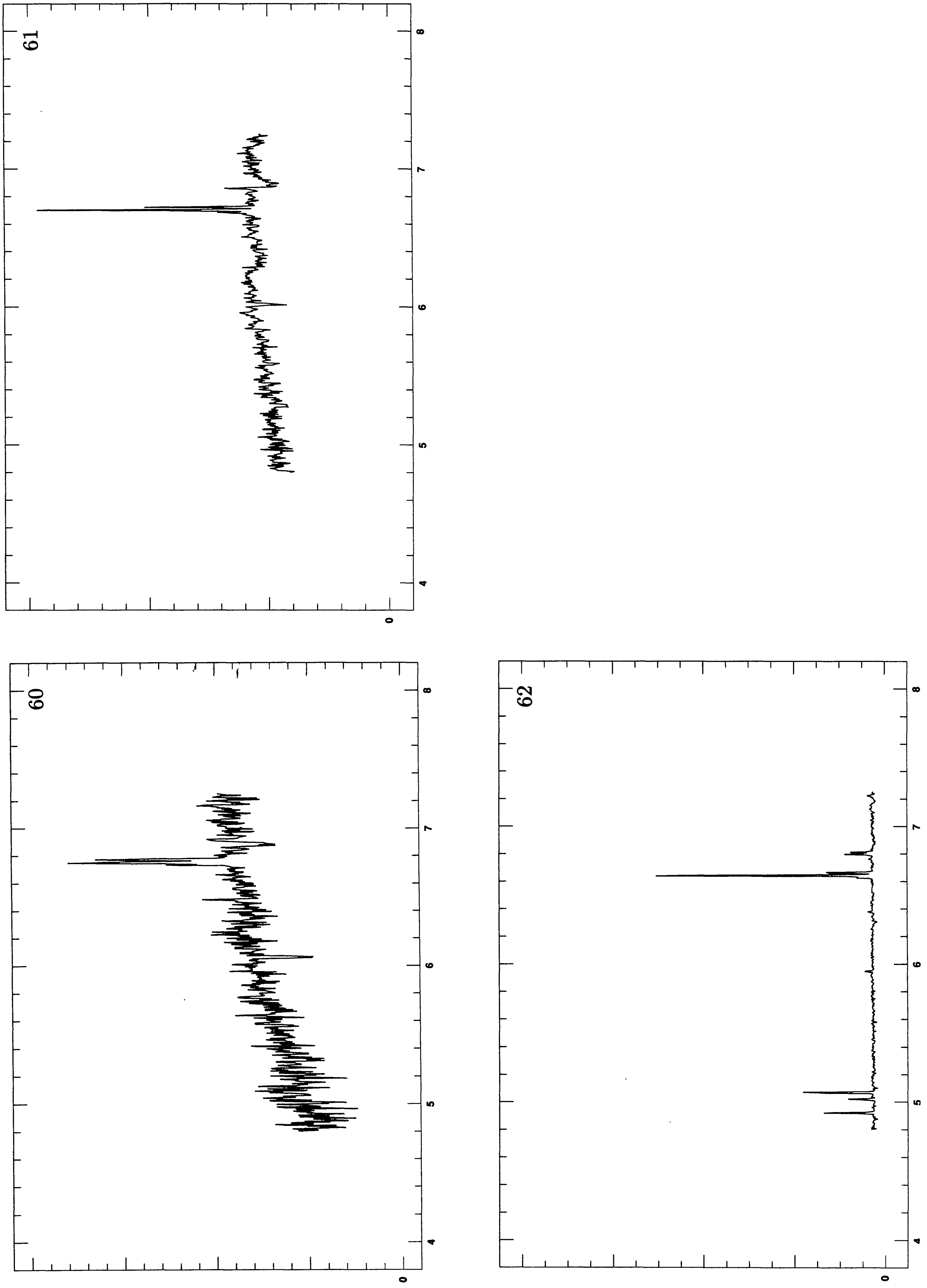

FIGURE 10. *(continued)*

FIGURE 11-67. CCD images of galaxies showing, unless otherwise indicated, for each galaxy a B−band image (top), a $B - R$ colour image (middle), and an Hα image corrected for continuum emission (bottom). For each galaxy the images are aligned and on the same scale, indicated in the colour image. Note, that the images are mirrored; north is up and east is to the right. The identification number of each source (cf. Tab. 3) is shown in the upper right-hand corner of the top panel. The gray scale goes from low intensity (white) to high intensity (black) in the upper and lower panels, and from blue (white) to red (black) in the colour images. The contour levels have been indicated separately in the captions for each image as: lowest level (step size) highest level. The values are not corrected for galactic foreground reddening, and they are expressed in mag arcsec^{-2}, except for the Hα images where they are expressed in log $\left(\mathrm{W\ arcsec}^{-2}\right)$.

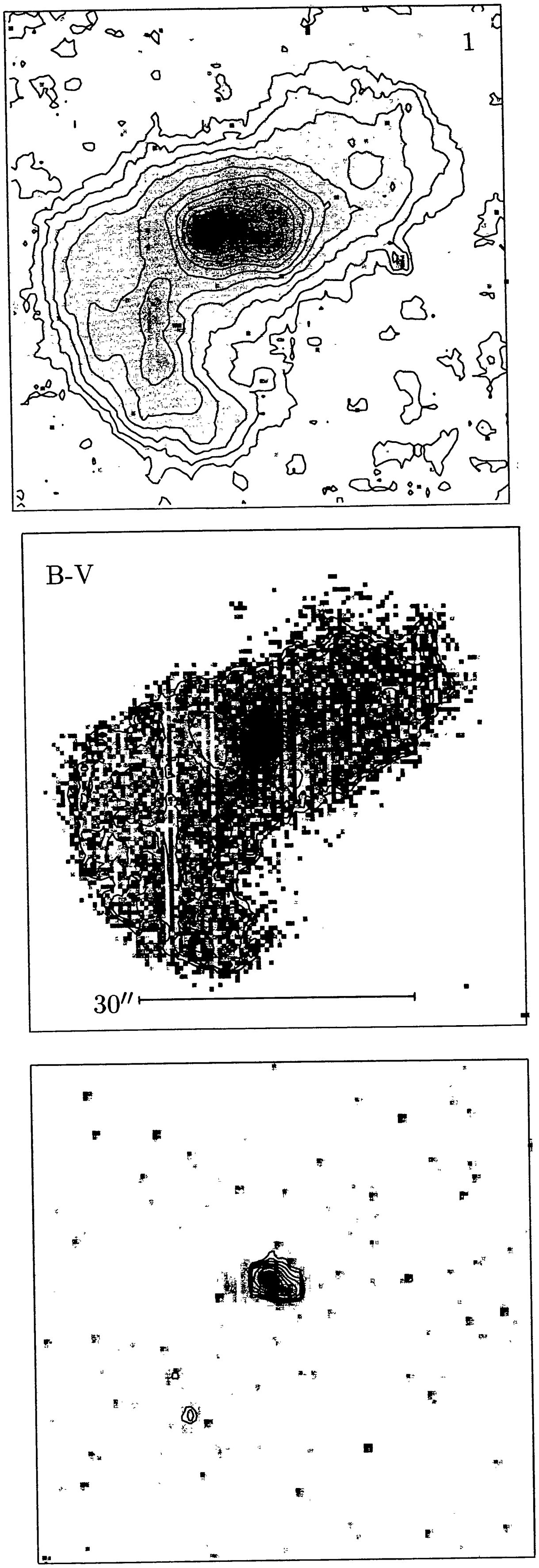

FIGURE 11. Field I: No. 1. B(top): 25.0(0.5)20.0; $B-V$ (middle): 0.5(0.1)0.8; Hα(bottom): $-18.5(0.2)-17.1$

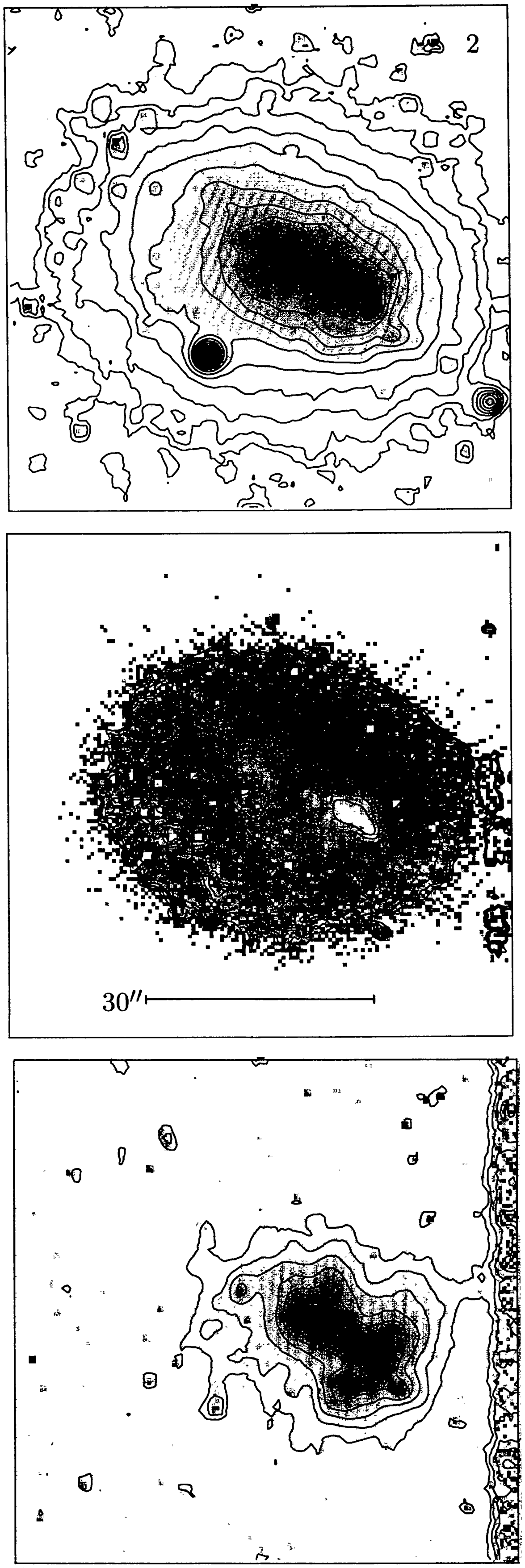

FIGURE 12. Field I: No. 2. B(top): 25.0(0.5)19.0; $B-R$(middle): 0.8(0.1)1.2; Hα(bottom): $-18.5(0.3)-16.4$

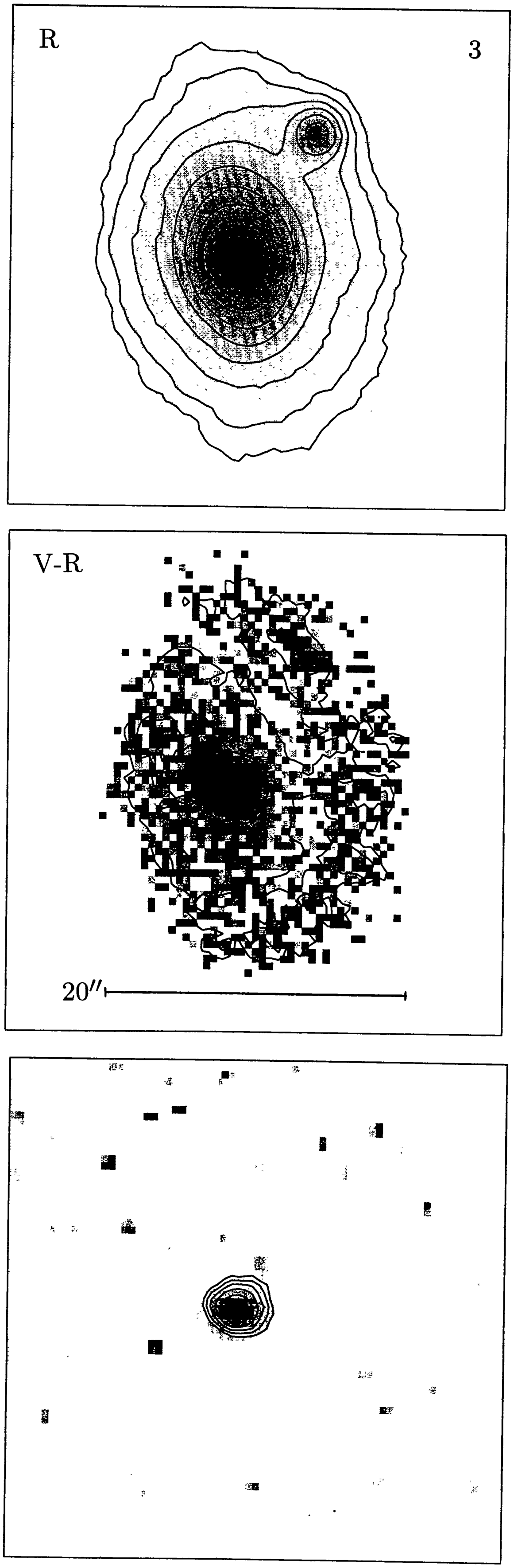

FIGURE 13. Field I: No. 2. B(top): 23.5(0.5)18.0; $V-R$(middle): 0.3(0.1)0.5; Hα(bottom): $-18.5(0.3)-17.0$

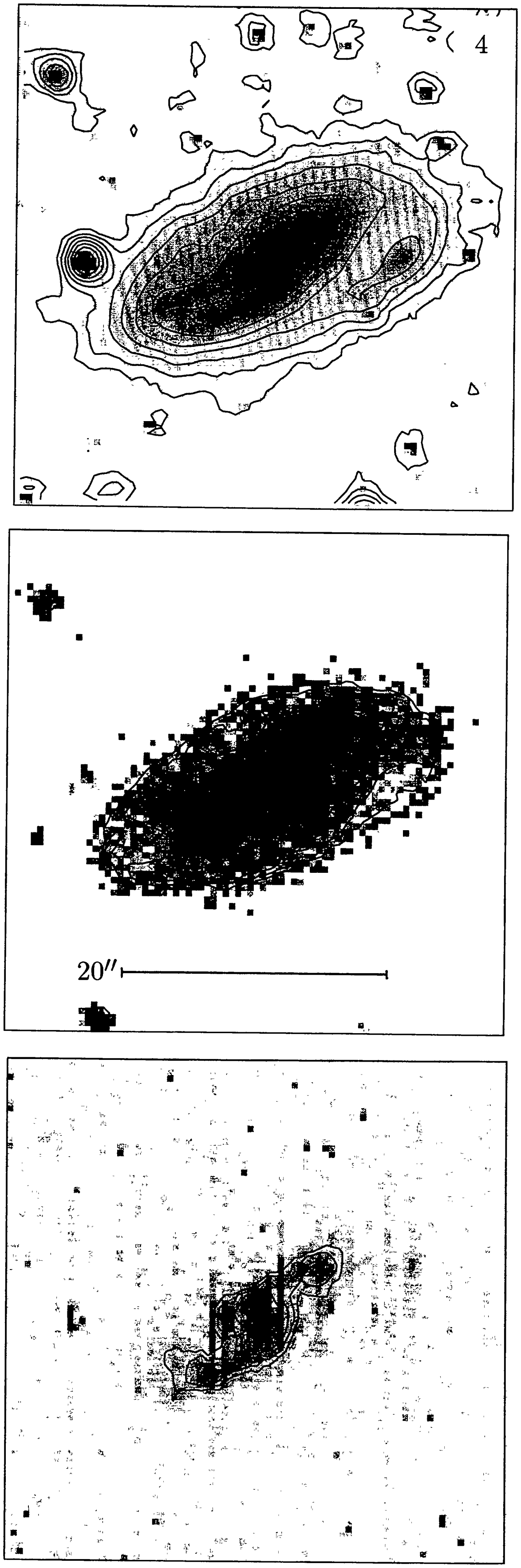

FIGURE 14. Field I: No. 4. B(top): 25.0(0.5)21.0; $B-R$(middle): 1.1(0.2)1.9; Hα(bottom): $-18.5(0.2)-17.7$

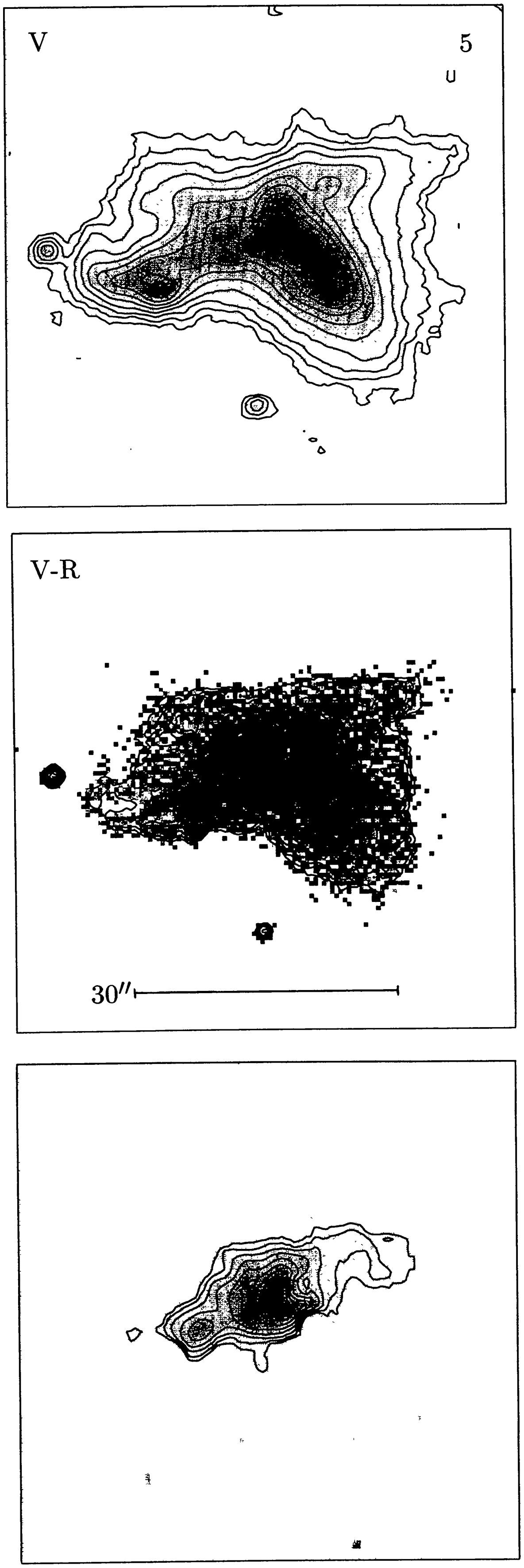

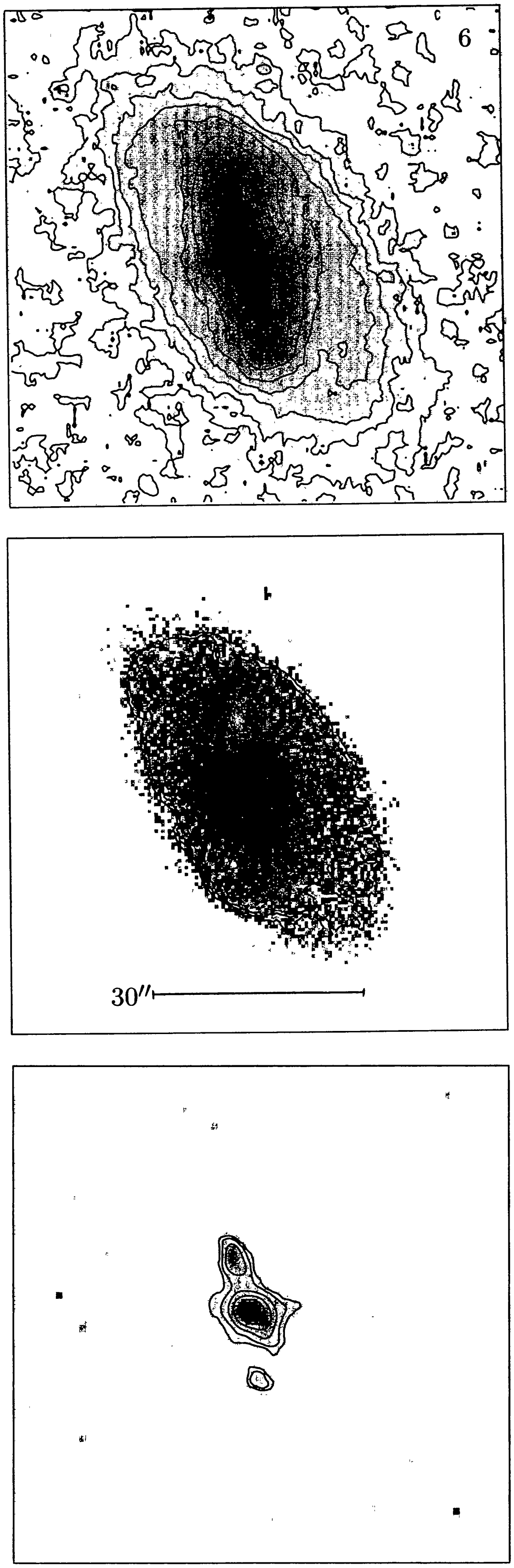

FIGURE 15. Field I: No. 5. V(top): 24.5(0.5)19.0; $V-R$(middle): 0.4(0.1)0.8; Hα(bottom): $-18.5(0.2)-16.9$

FIGURE 16. Field I: No. 6. B(top): 25.0(0.5)20.5; $B-R$(middle): 1.1(0.2)1.9; Hα(bottom): $-18.5(0.3)-17.0$

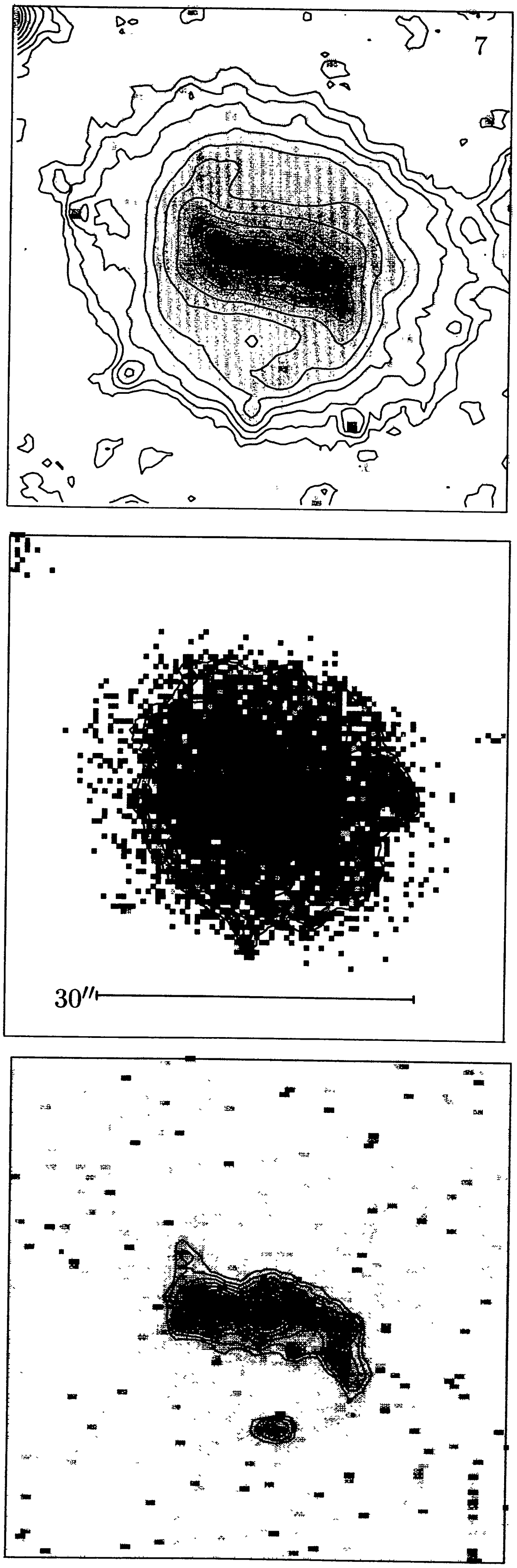

FIGURE 17. Field I: No. 7. B(top): 25.0(0.5)20.0; $B-R$(middle): 0.8(0.2)1.6; Hα(bottom): $-18.5(0.2)-16.7$

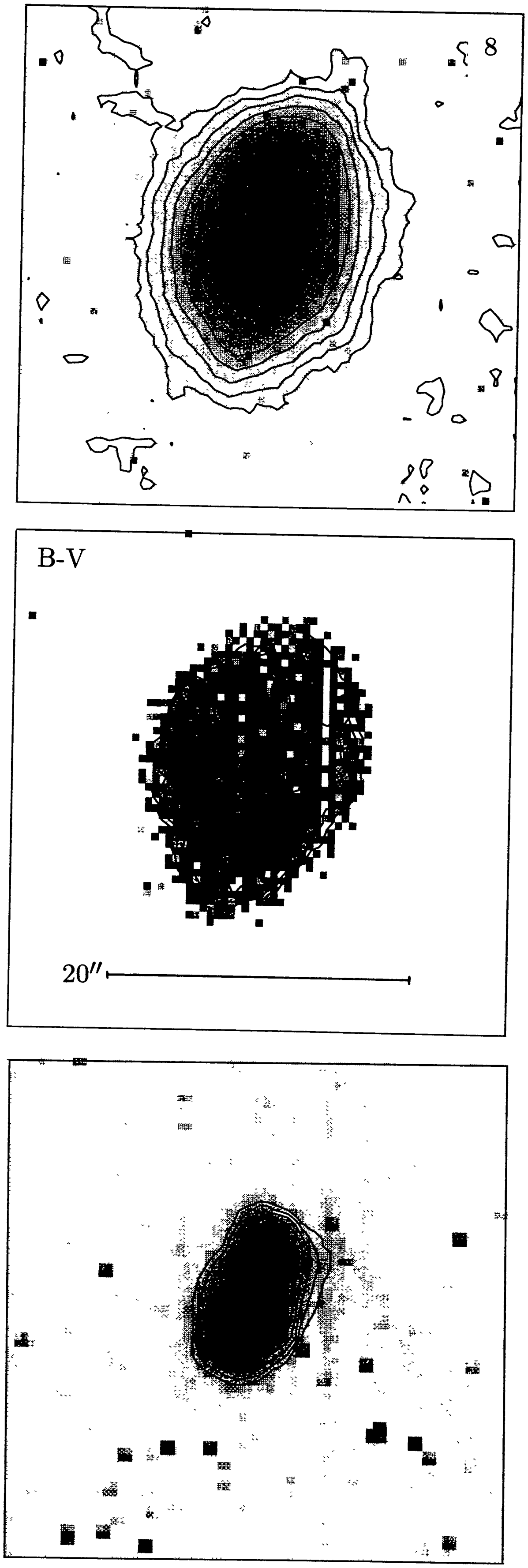

FIGURE 18. Field I: No. 8. B(top): 25.0(0.5)20.0; $B-V$ (middle): 0.5(0.1)0.8; Hα(bottom): $-18.35(0.2)-17.15$

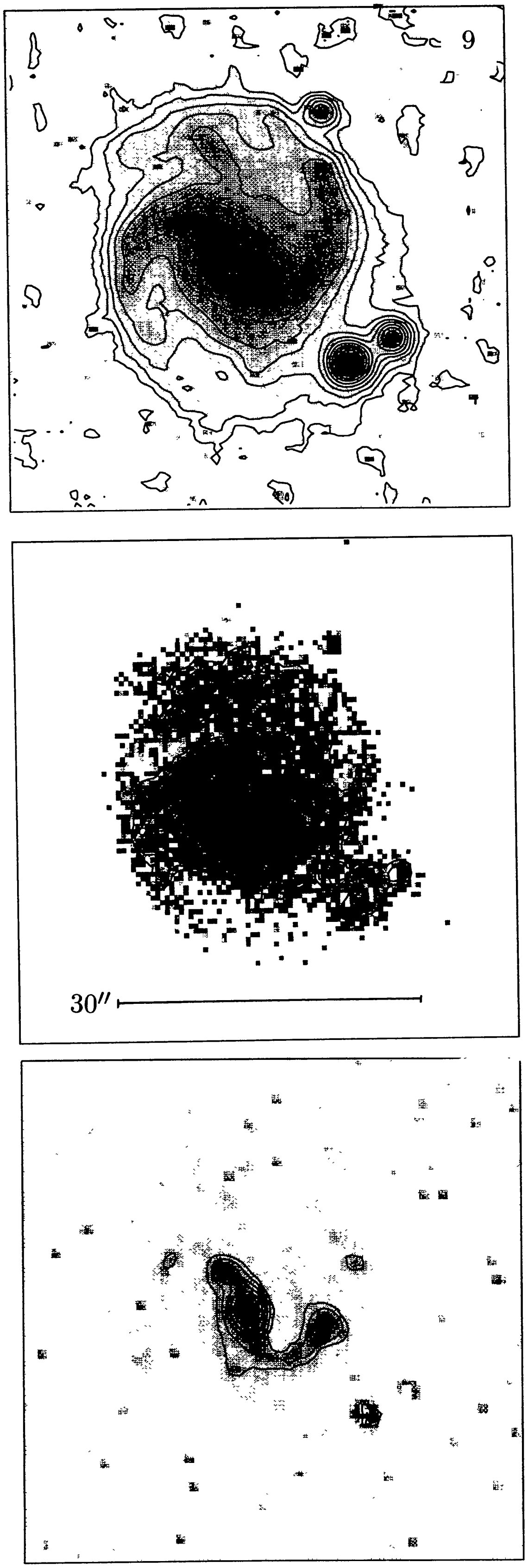

FIGURE 19. Field I: No. 9. B(top): 24.8(0.5)19.8; $B-R$(middle): 1.0(0.1)1.3; Hα(bottom): $-18.4(0.2)-17.2$

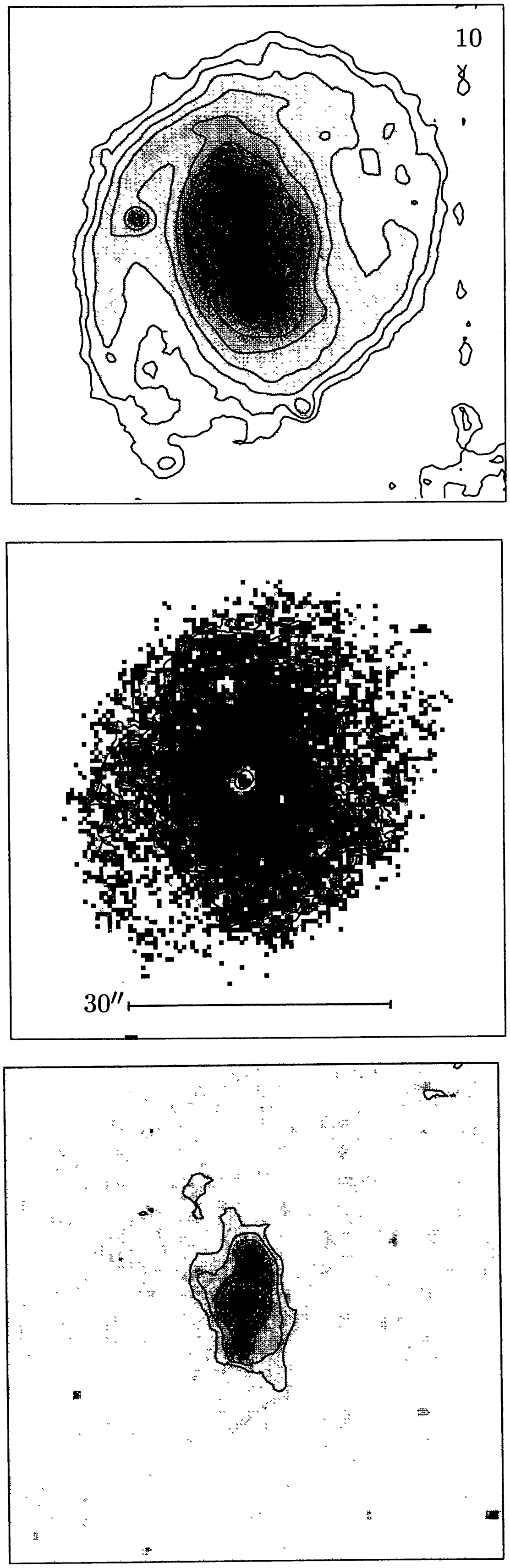

FIGURE 20. Field I: No. 10. B(top): 25.0(0.5)19.5; $B-R$(middle): 1.0(0.1)1.3; Hα(bottom): $-18.5(0.3)-16.4$

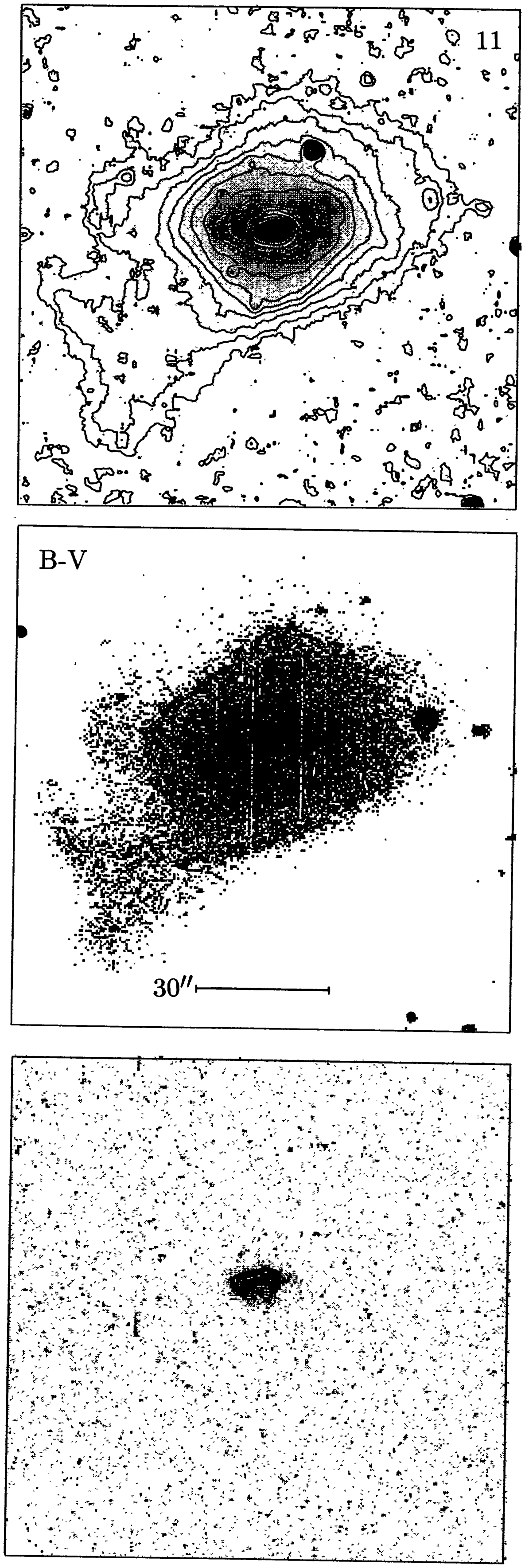

FIGURE 21. Field I: No. 11. B(top): 25.0(0.5)18.5; $B-V$ (middle): 0.5(0.1)0.8; Hα(bottom): $-17.3(0.2)-16.5$

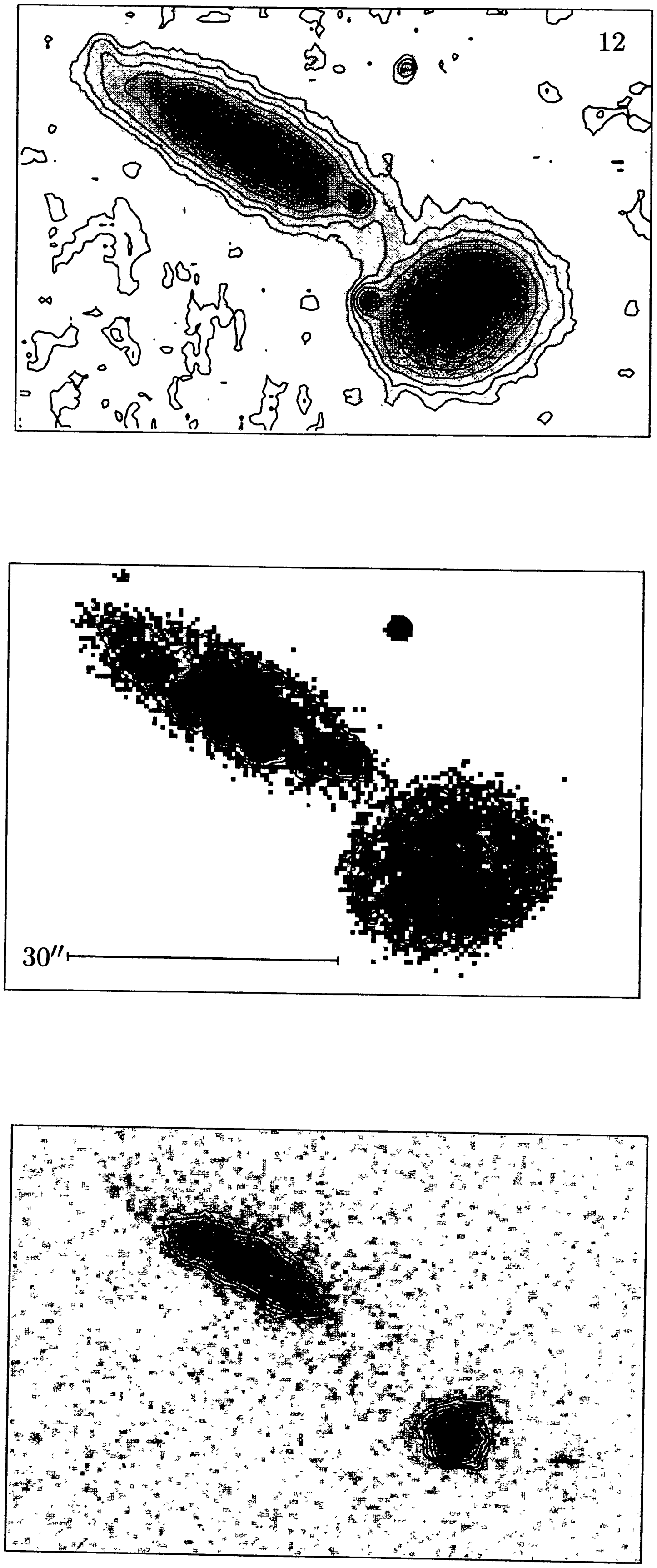

FIGURE 22. Field I: No. 12. B(top): 25.0(0.5)20.5; $B-R$ (middle): 1.2(0.2)2.0; Hα(bottom): $-18.65(0.2)-17.65$

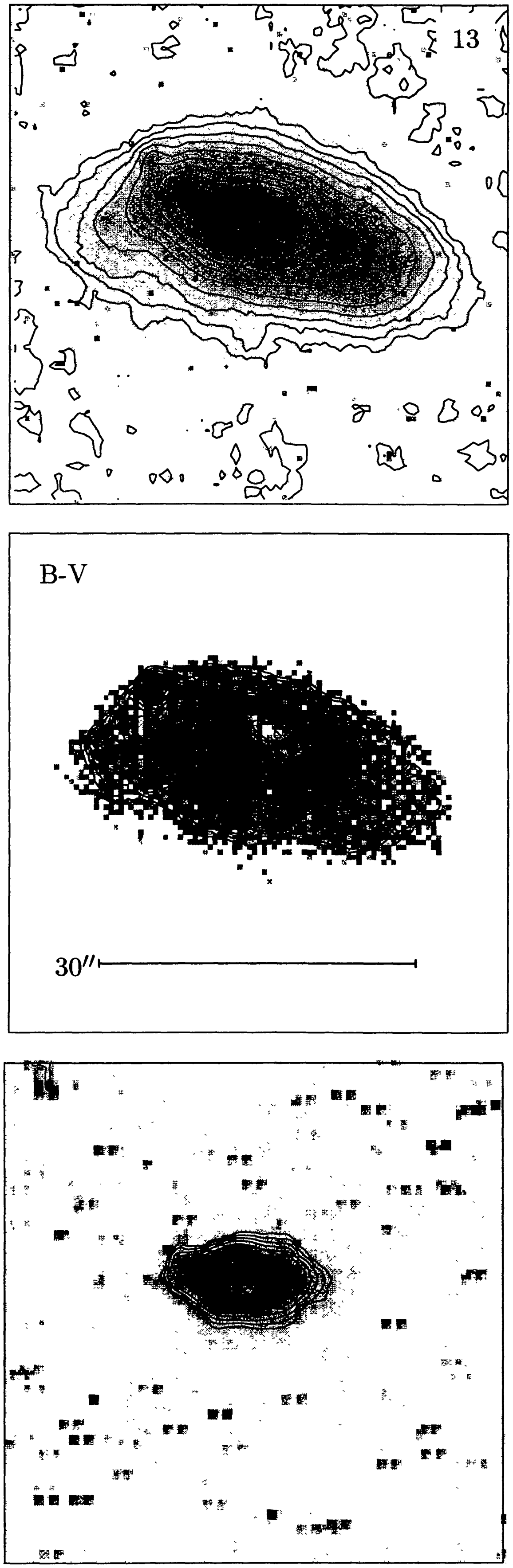

FIGURE 23. Field I: No. 13. B(top): 25.0(0.5)20.0; $B-V$ (middle): 0.5(0.1)0.9; Hα(bottom): $-18.5(0.2)-17.3$

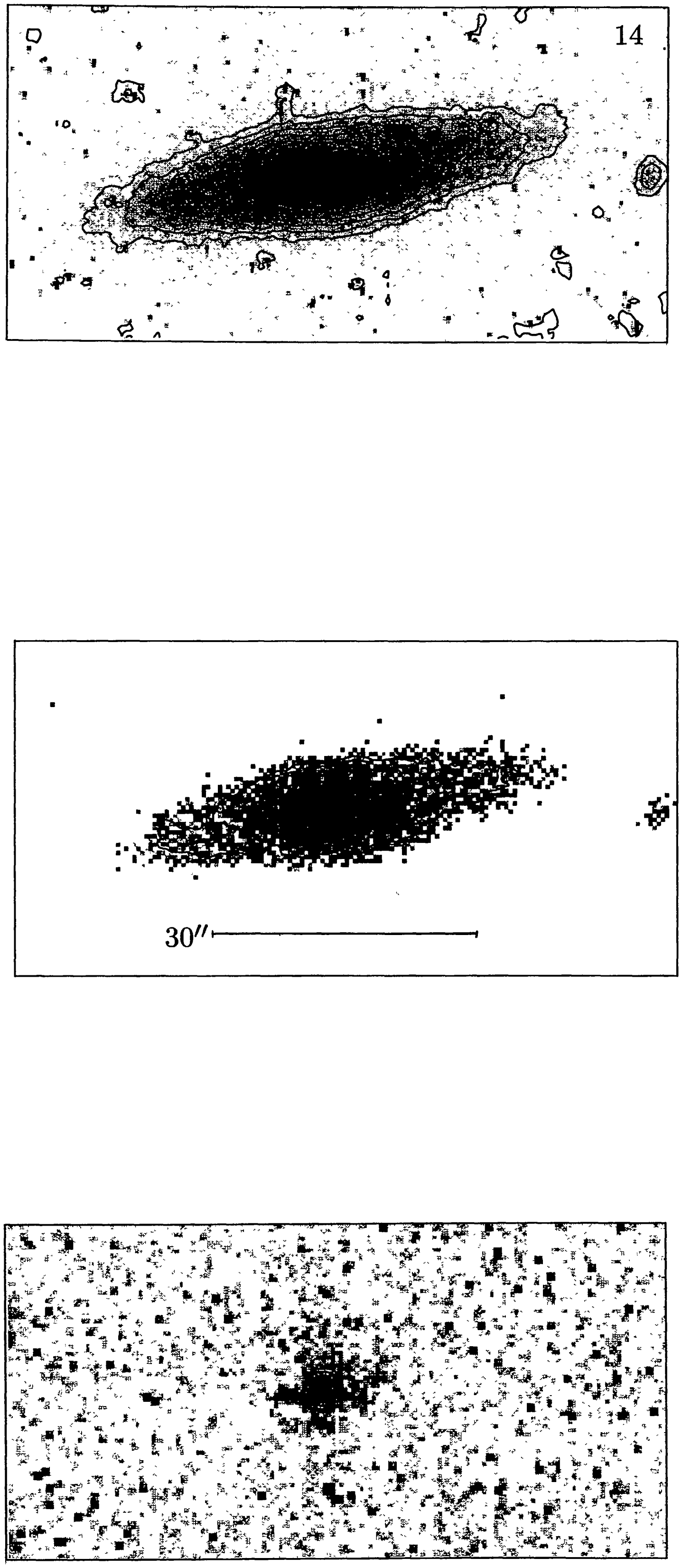

FIGURE 24. Field I: No. 14. B(top): 25.0(0.5)21.5; $B-R$(middle): 2.1(0.2)2.1; Hα(bottom): $-18.5(0.2)-17.9$

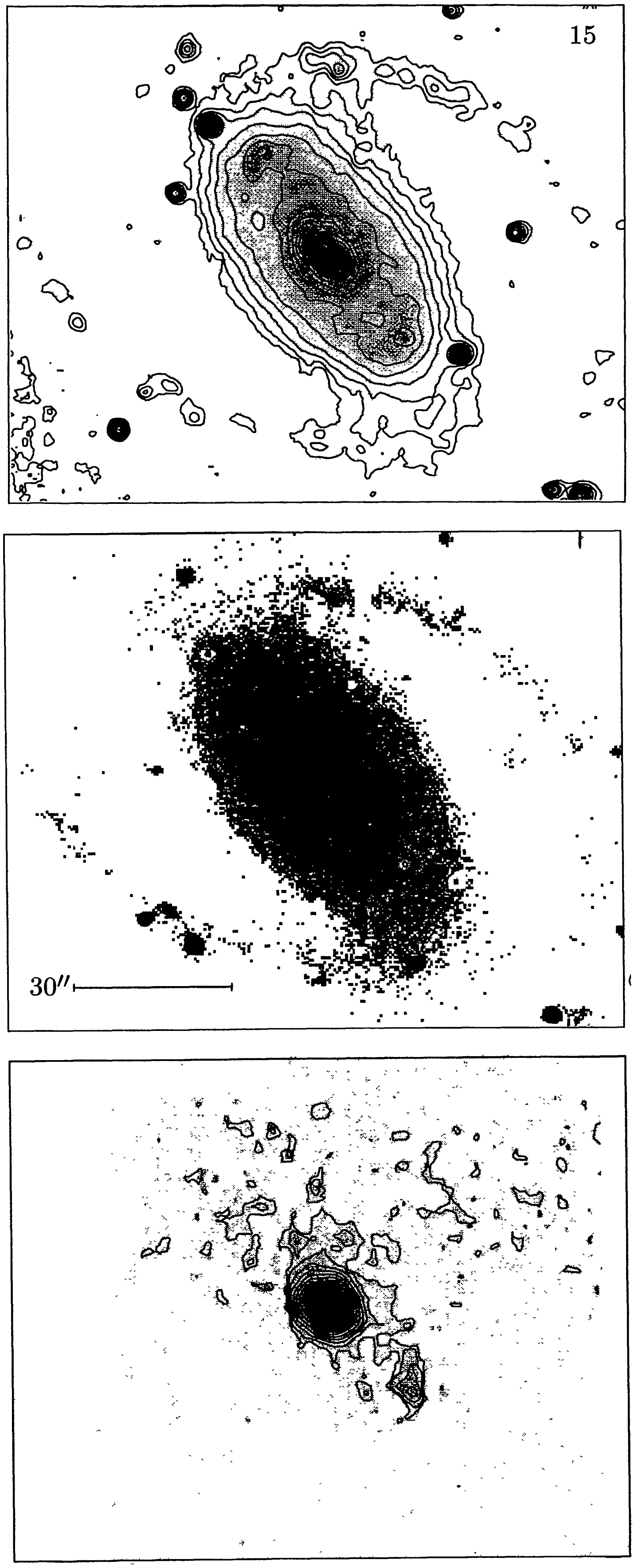

FIGURE 25. Field I: No. 15. B(top): 25.0(0.5)19.5; $B-R$(middle): 1.2(0.2)2.0; Hα(bottom): $-18.5(0.2)-16.9$

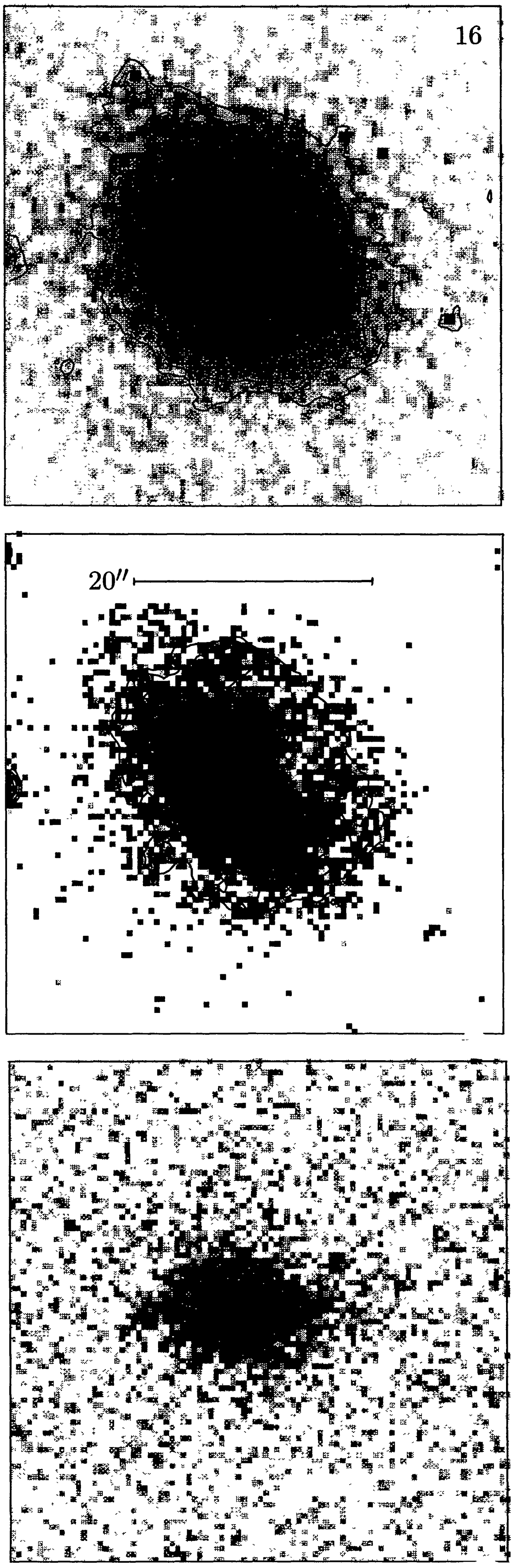

FIGURE 26. Field I: No. 16. B(top): 25.0(0.5)22.0; $B-R$(middle): 1.2(0.2)2.0; Hα(bottom): $-18.5(0.2)-17.9$

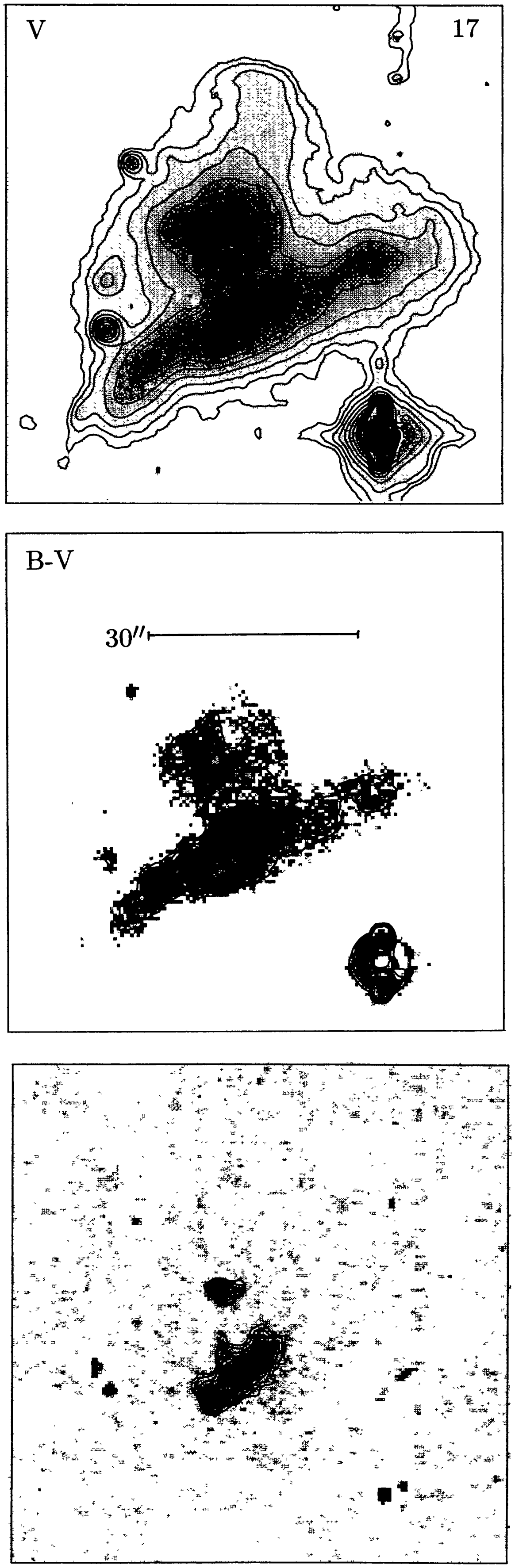

FIGURE 27. Field I: No. 17. V(top): 24.5(0.5)19.5; $B-V$(middle): 0.5(0.2)1.3; Hα(bottom): $-18.5(0.2)-17.5$

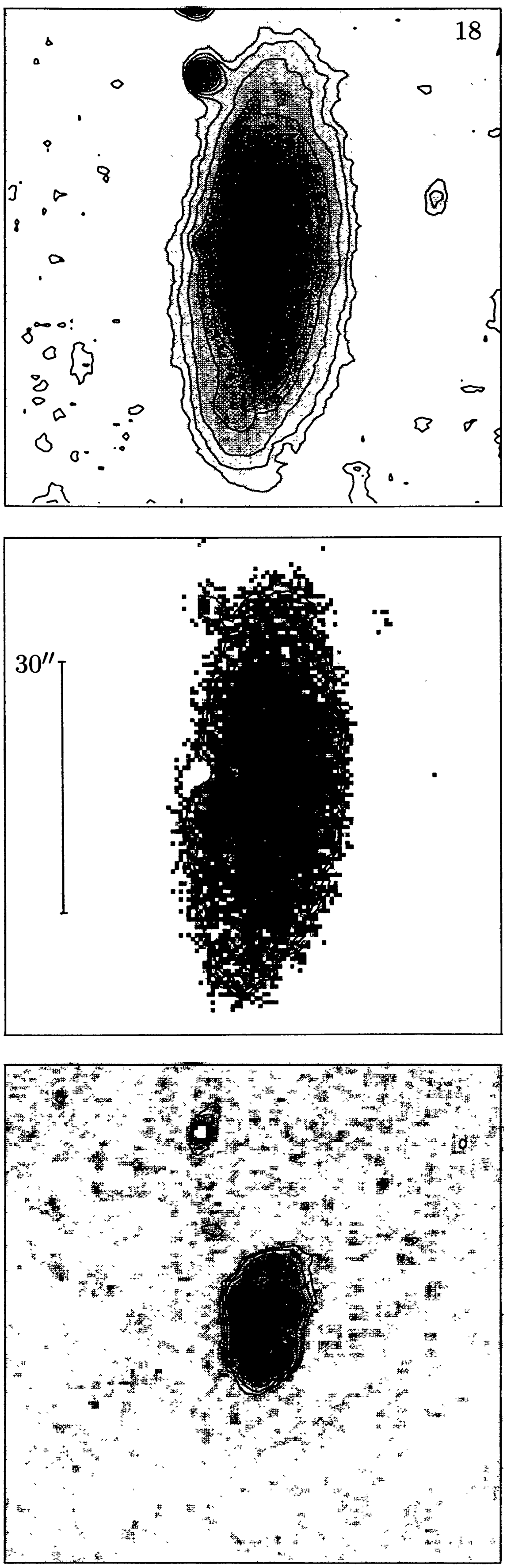

FIGURE 28. Field I: No. 18. B(top): 25.0(0.5)21.0; $B-R$(middle): 1.2(0.2)2.0; Hα(bottom): $-18.5(0.2)-17.3$

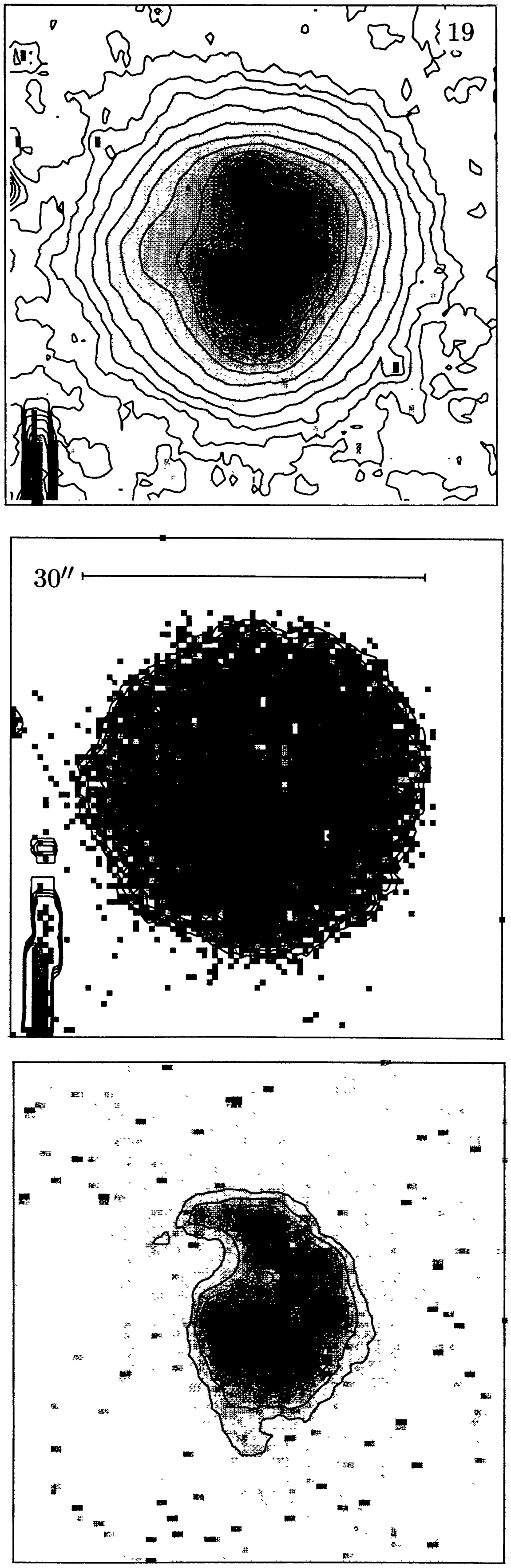

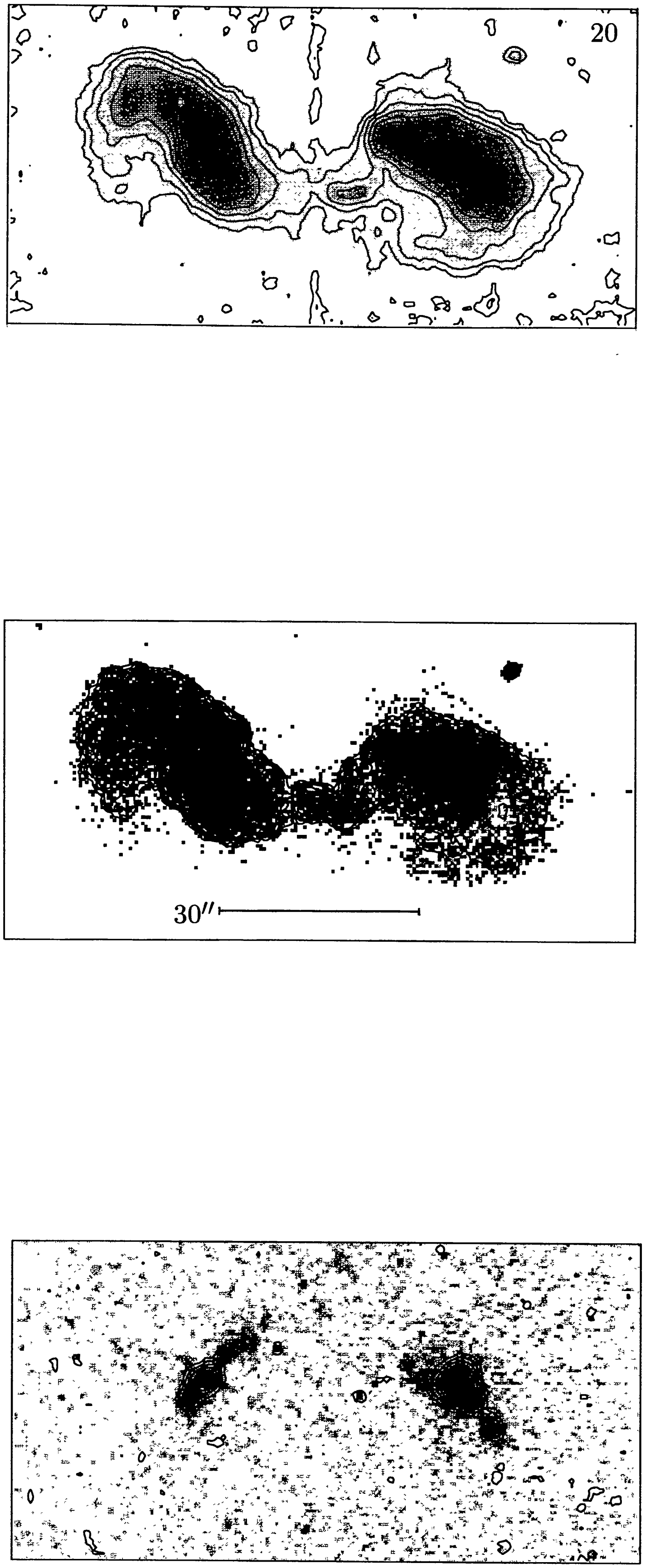

FIGURE 29. Field I: No. 19. B(top): 25.0(0.5)18.5; $B-R$(middle): 0.6(0.2)1.2; Hα(bottom): $-18.5(0.3)-17.0$

FIGURE 30. Field I: No. 20. B(top): 25.0(0.5)19.5; $B-R$(middle): 0.7(0.2)2.1; Hα(bottom): $-18.5(0.2)-17.3$

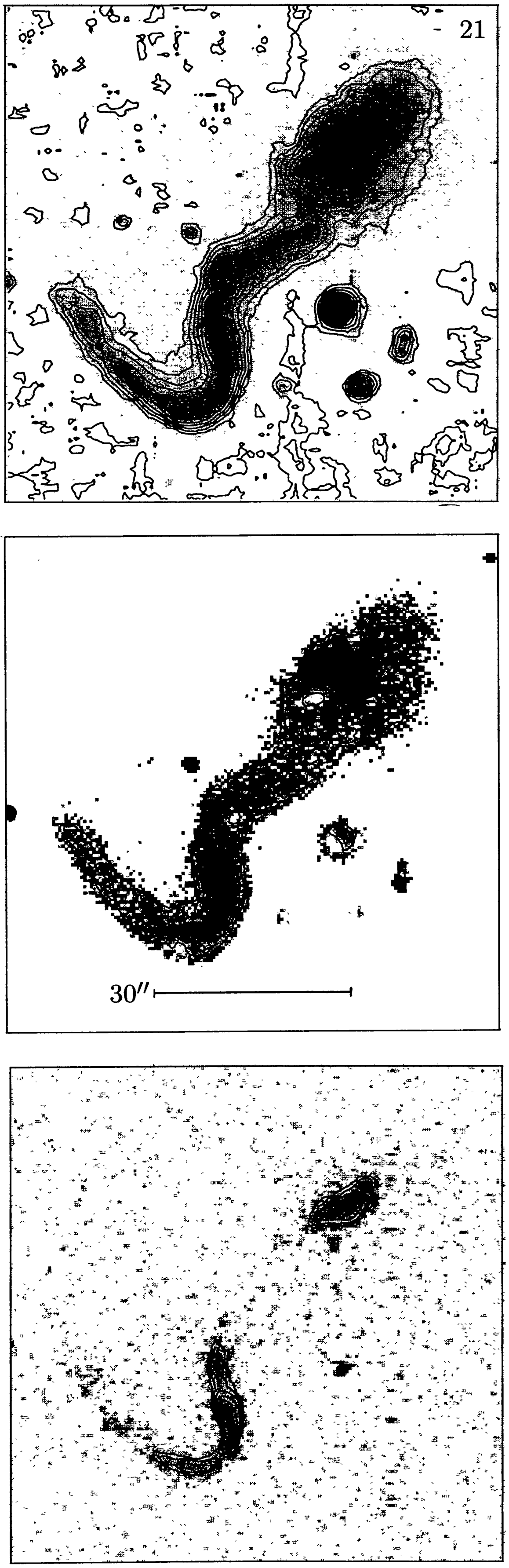

FIGURE 31. Field I: No. 21. B(top): 25.0(0.5)22.0; $B-R$(middle): 1.2(0.2)2.0; Hα(bottom): $-18.65(0.2)-17.65$

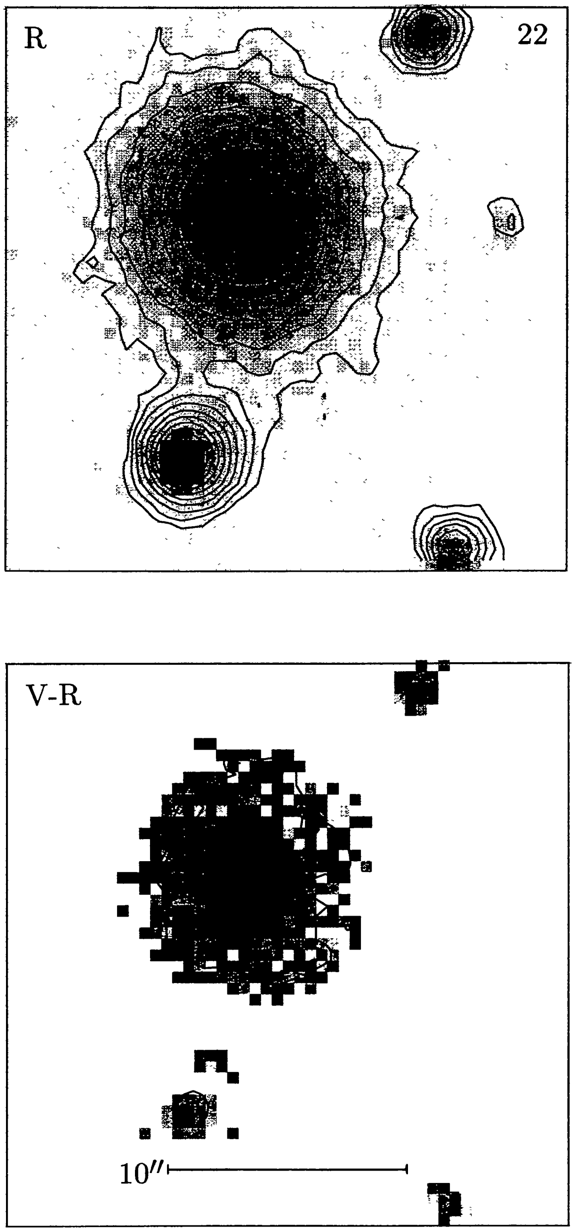

FIGURE 32. Field I: No. 22. R(upper): 24.0(0.5)20.0; $V-R$(lower): 0.5(0.1)0.7;No Hα image available.

FIGURE 33. Field I: No. 23. B(top): 25.0(0.5)19.5; $B-R$(middle): 0.9(0.2)1.7; Hα(bottom): $-18.5(0.2)-16.9$

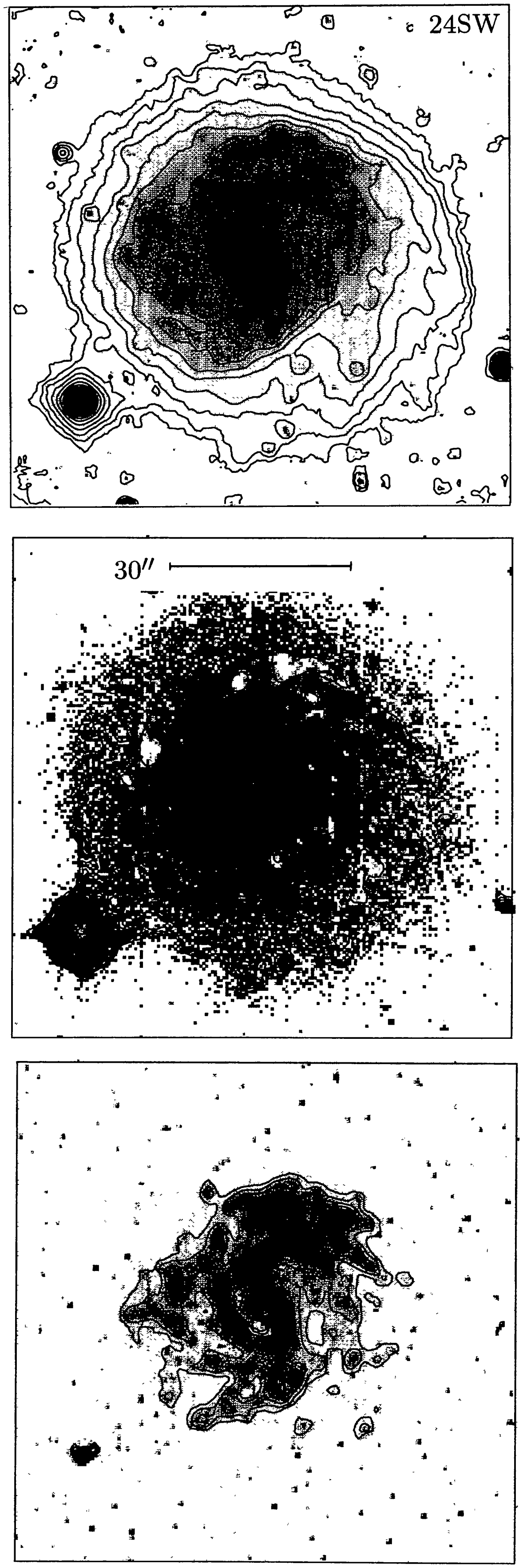

FIGURE 34. Field I: No. 24. south-western galaxy B(top): 25.0(0.5) 18.5; $B-R$(middle): 0.8(0.2)1.4; Hα(bottom): $-18.5(0.3)-16.4$

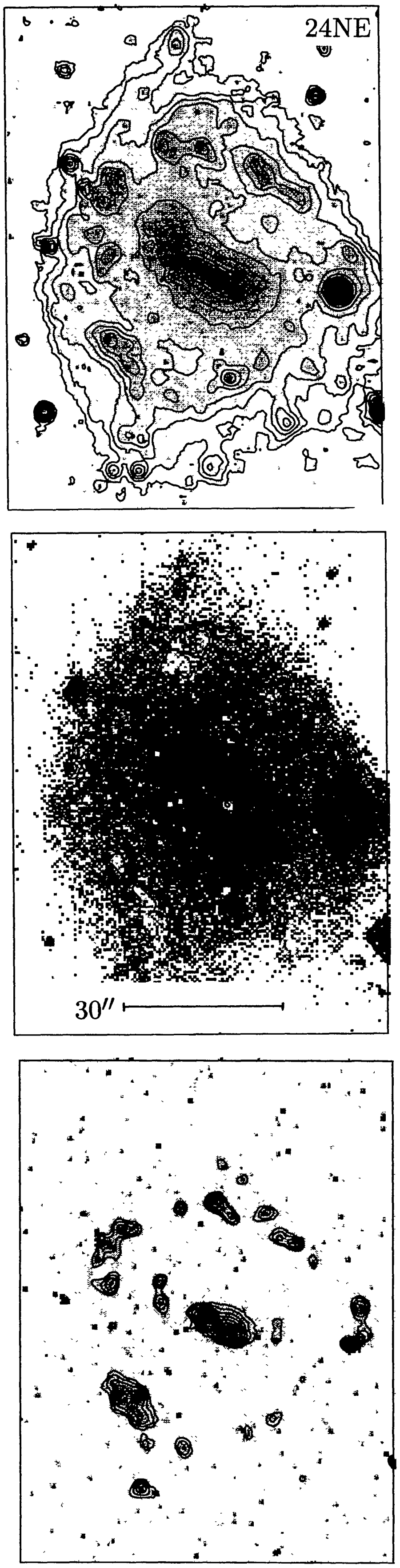

FIGURE 35. Field I: No. 24, north-eastern galaxy B(top): 25.0(0.5) 20.5; $B-R$(middle): 0.8(0.2)1.4; $H\alpha$(bottom): −18.5(0.2)−17.3

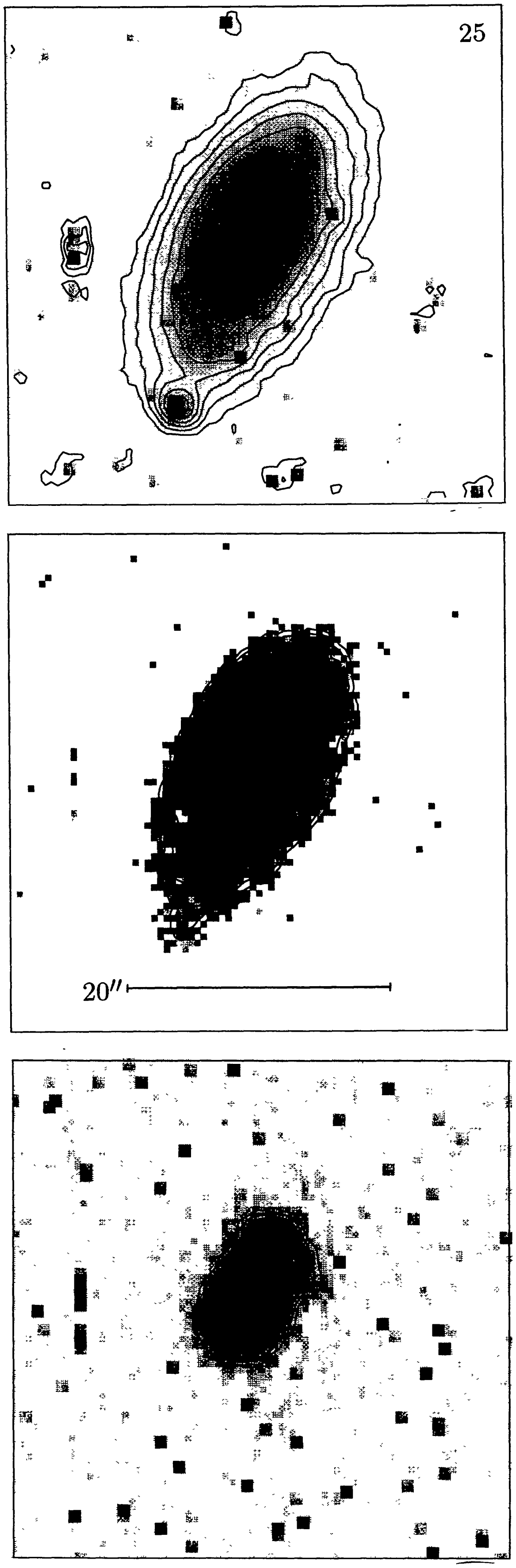

FIGURE 36. Field I: No. 25. B(top): 25.0(0.5)20.5; $B-R$(middle): 0.8(0.2)1.6; $H\alpha$(bottom): −18.5(0.2)−17.5

1991A&AS...91...61V

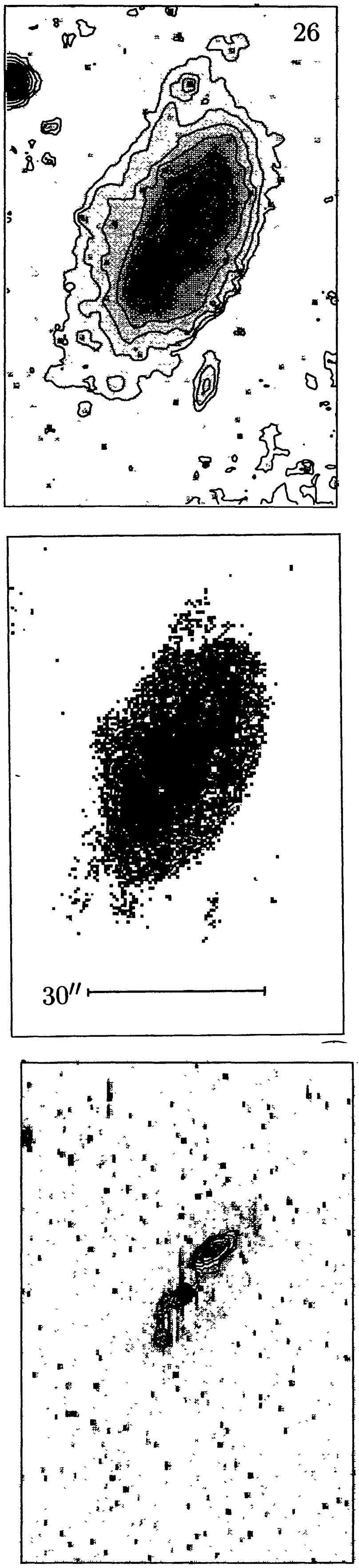

FIGURE 37. Field I: No. 26. B(top): 25.0(0.5)20.5; $B-R$(middle): 1.2(0.2)1.8; Hα(bottom): $-18.5(0.2)-17.5$

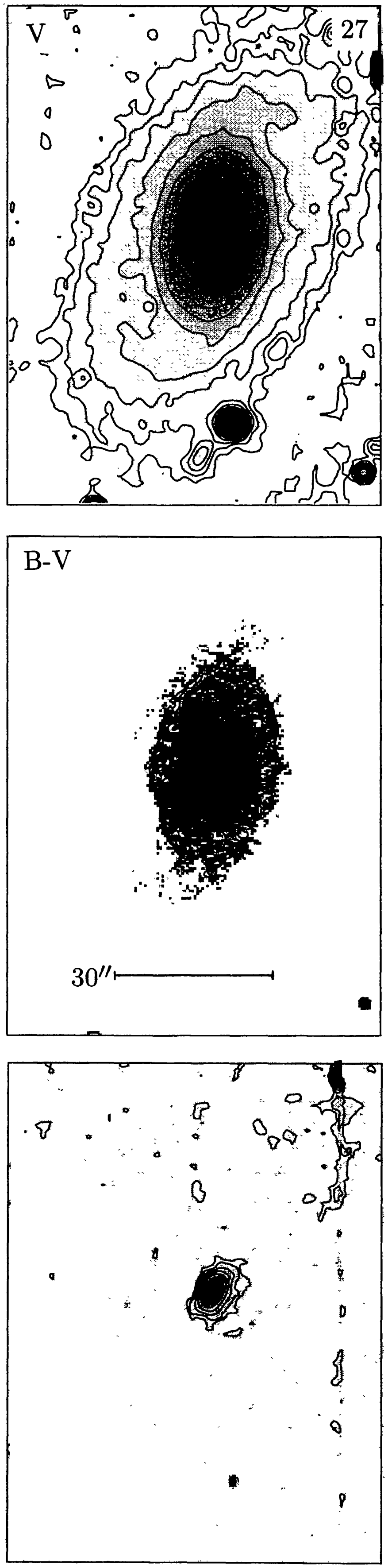

FIGURE 38. Field I: No. 27. V(top): 24.5(0.5)17.5; $B-V$(middle): 0.7(0.1)1.1; Hα(bottom): $-18.5(0.3)-16.7$

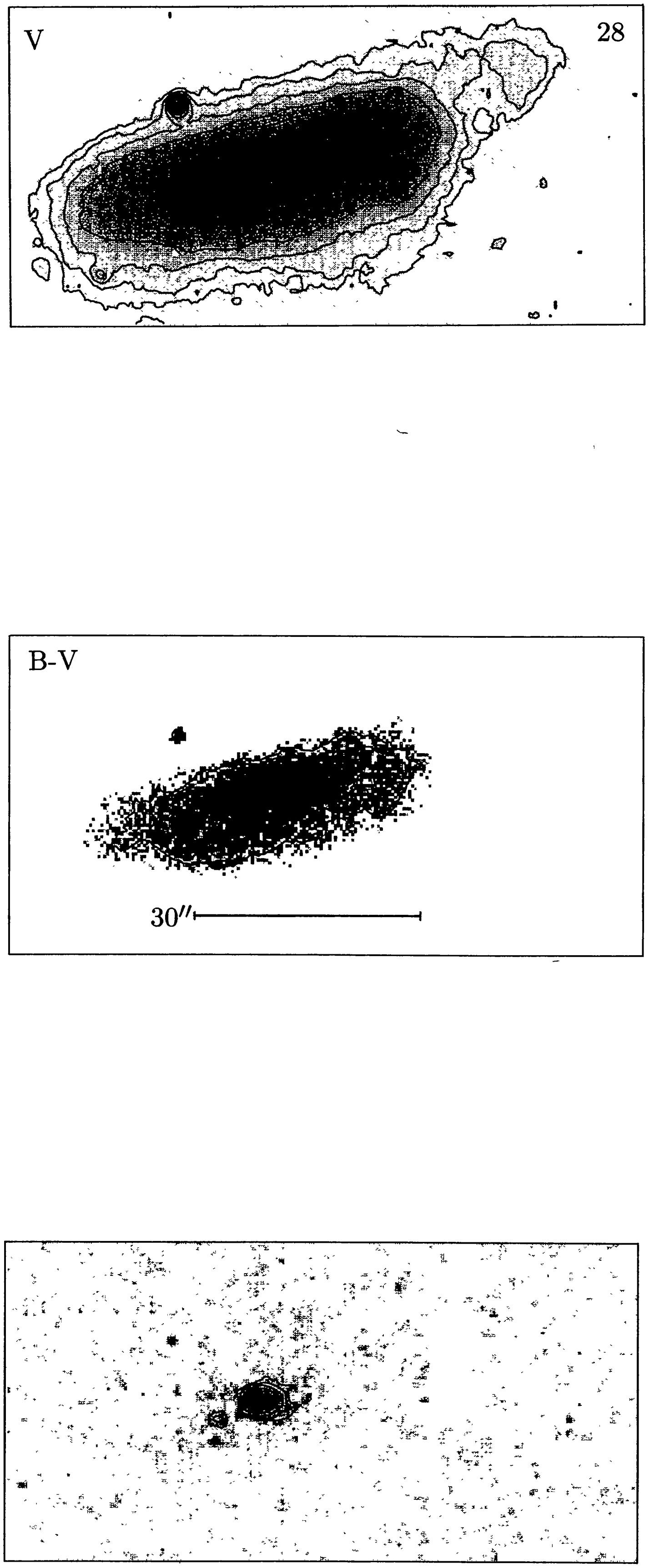

FIGURE 39. Field I: No. 28. V(top): 24.5(0.5)20.5; $B-V$(middle): 0.7(0.2)1.3; Hα(bottom): $-18.5(0.2)-17.5$

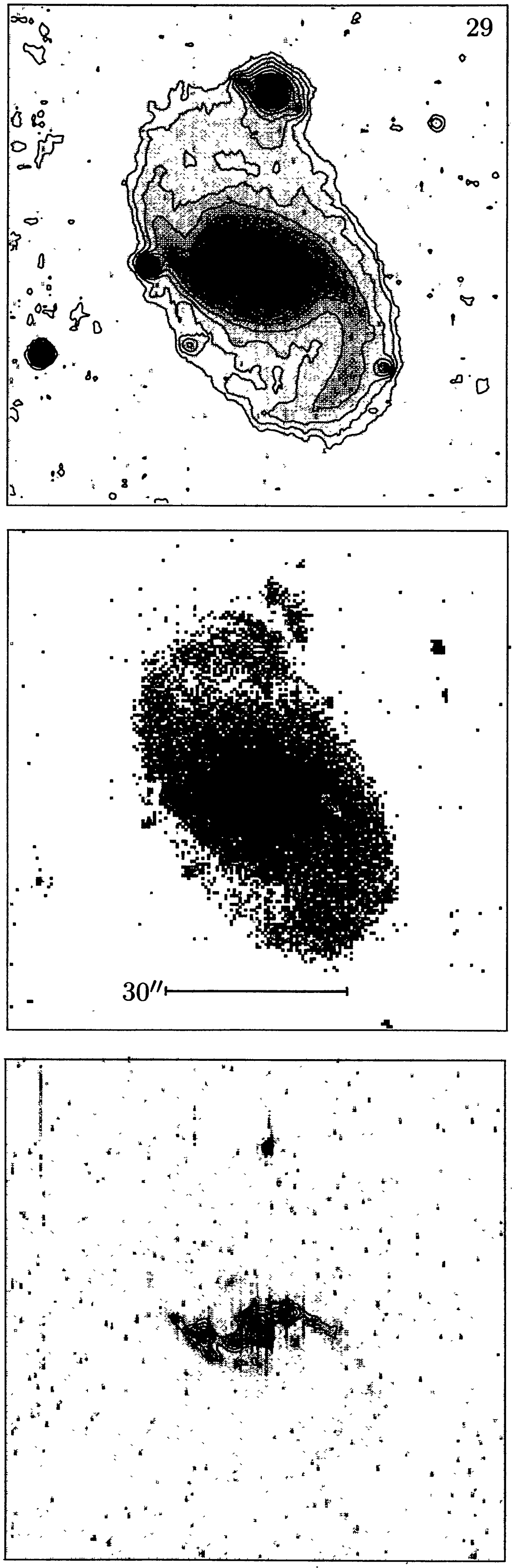

FIGURE 40. Field I: No. 29. B(top): 25.0(0.5)20.5; $B-R$(middle): 1.1(0.2)1.7; Hα(bottom): $-18.5(0.2)-17.3$

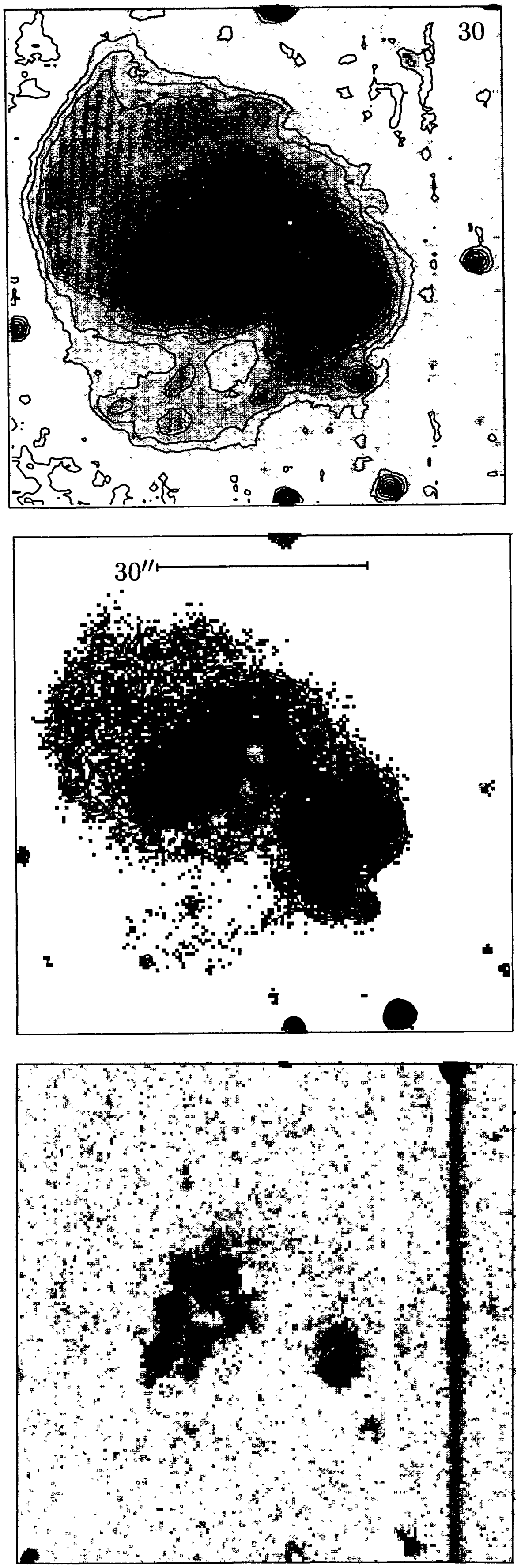

FIGURE 41. Field I: No. 30. B(top): 25.0(0.5)20.5; $B-R$(middle): 0.7(0.2)2.1; Hα(bottom): −18.5(0.15)−17.35

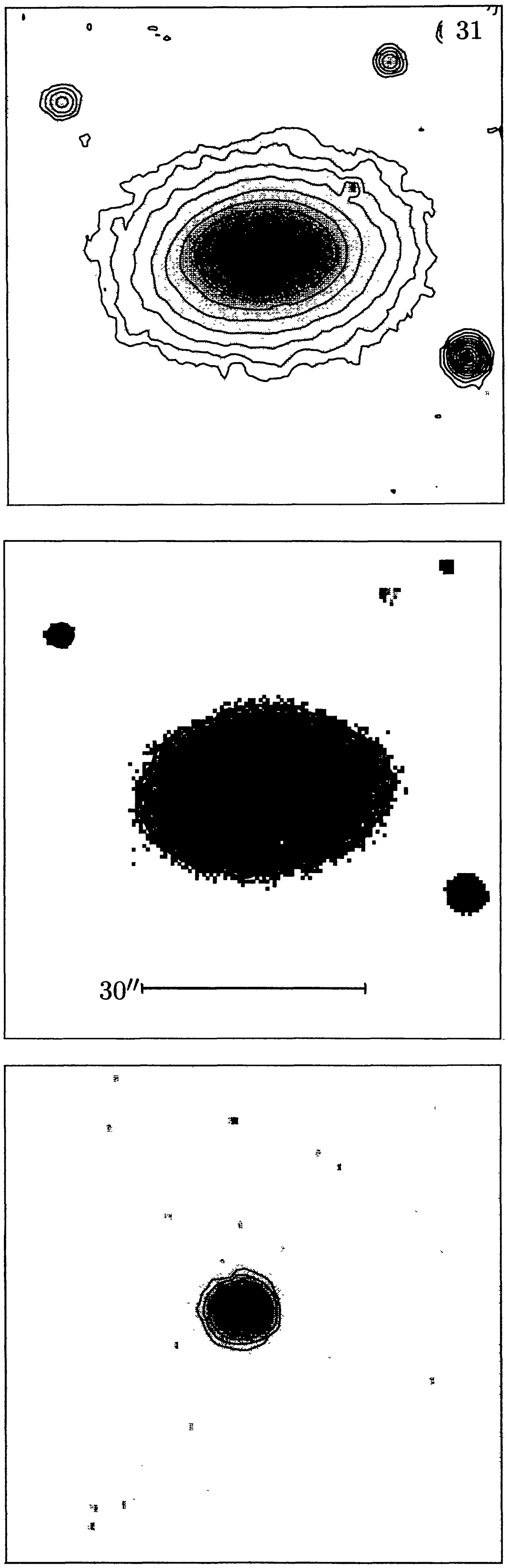

FIGURE 42. Field I: No. 31. B(top): 25.0(0.5)19.0; $B-R$(middle): 1.0(0.1)1.4; Hα(bottom): −18.5(0.3)−17.0

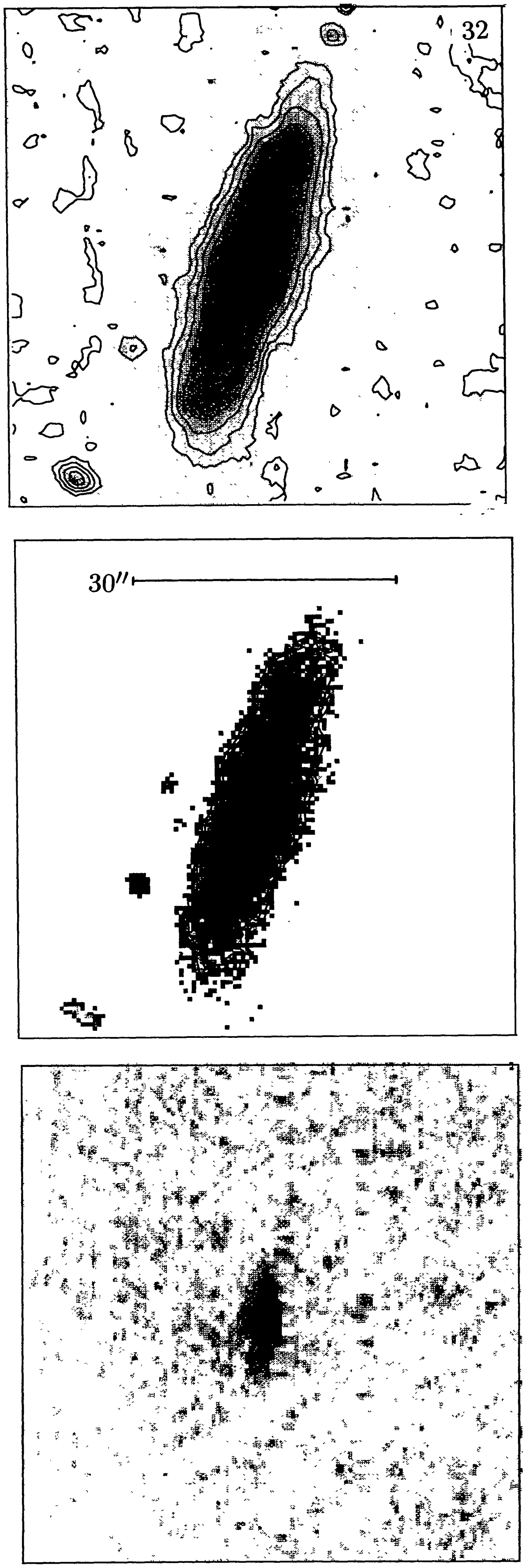

FIGURE 43. Field I: No. 32. B(top): 25.0(0.5)20.5; $B-R$(middle): 1.1(0.2)1.7; Hα(bottom): $-17.95(0.2)-17.3$

FIGURE 44. Field I: No. 33. R(top): 24.0(0.5)19.5; $B-R$(middle): 0.8(0.2)1.8; Hα(bottom): $-18.5(0.2)-17.5$

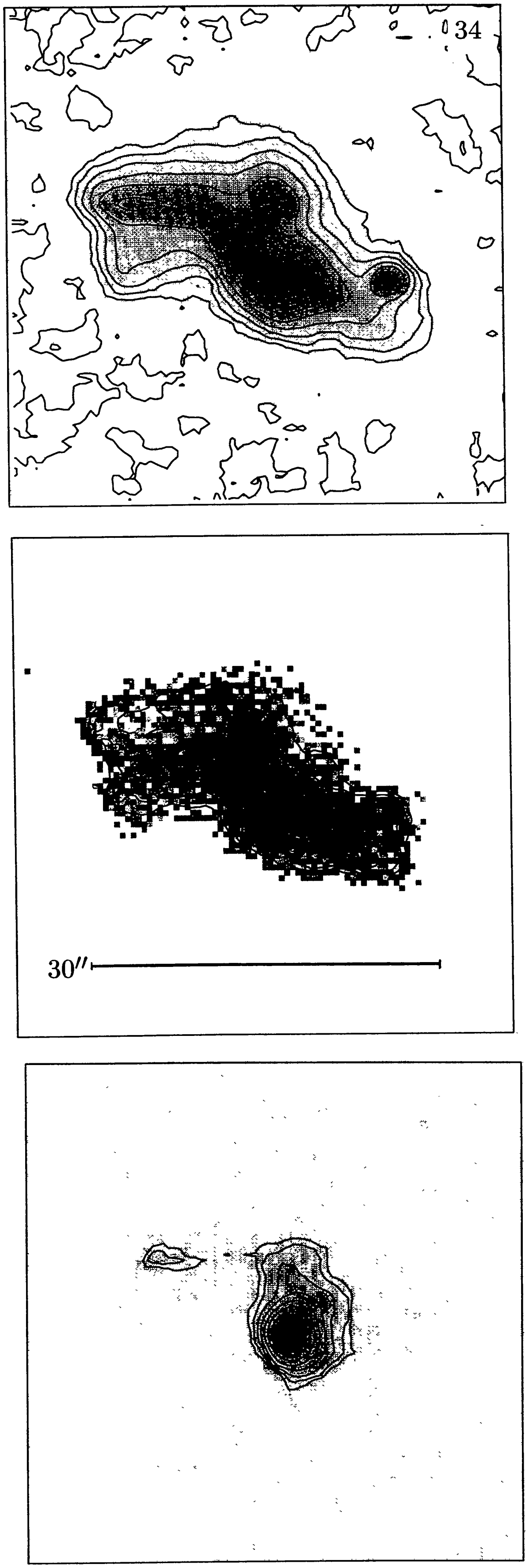

FIGURE 45. Field I: No. 34. *B*(top): 25.0(0.5)20.5; *B* – *R*(middle): 0.9(0.2)1.5; Hα(bottom): –18.65(0.2)–17.05

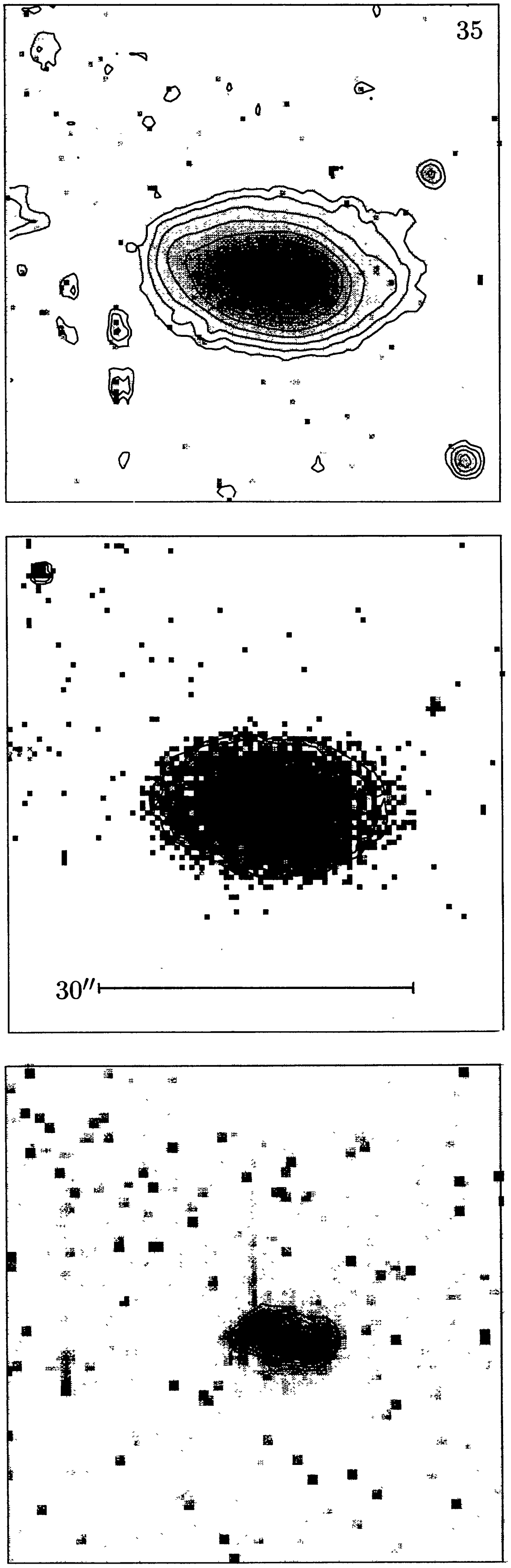

FIGURE 46. Field I: No. 35. *B*(top): 25.0(0.5)20.5; *B* – *R*(middle): 0.8(0.2)1.6; Hα(bottom): –18.5(0.2)–17.3

1991A&AS...91...61V

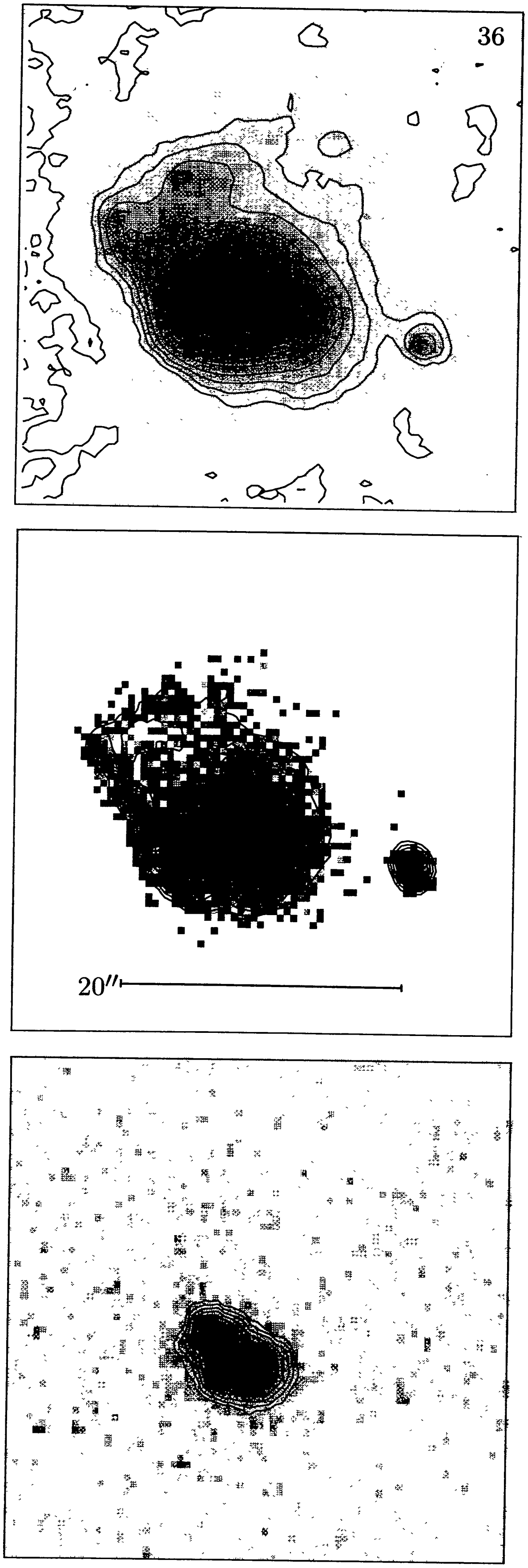

FIGURE 47. Field I: No. 36. B(top): 24.0(0.5)21.0; $B-R$(middle): 0.7(0.2)1.3; Hα(bottom): $-18.5(0.2)-17.3$

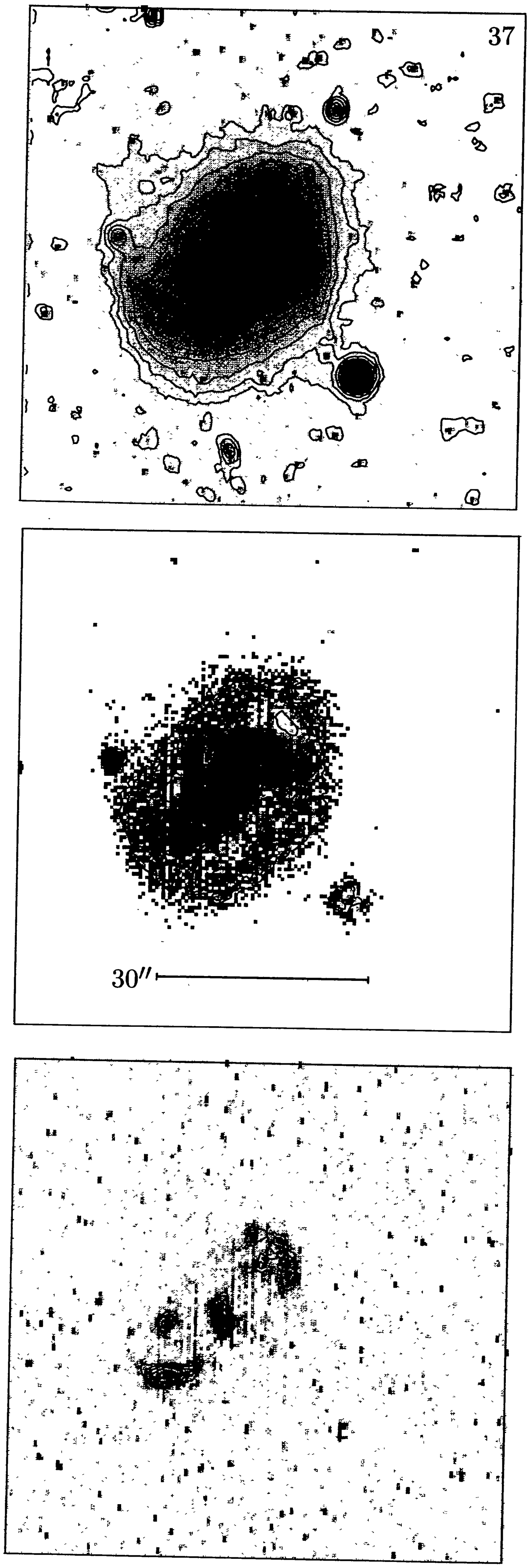

FIGURE 48. Field I: No. 37. B(top): 25.0(0.5)21.0; $B-R$(middle): 1.1(0.2)1.9; Hα(bottom): $-18.5(0.2)-17.5$

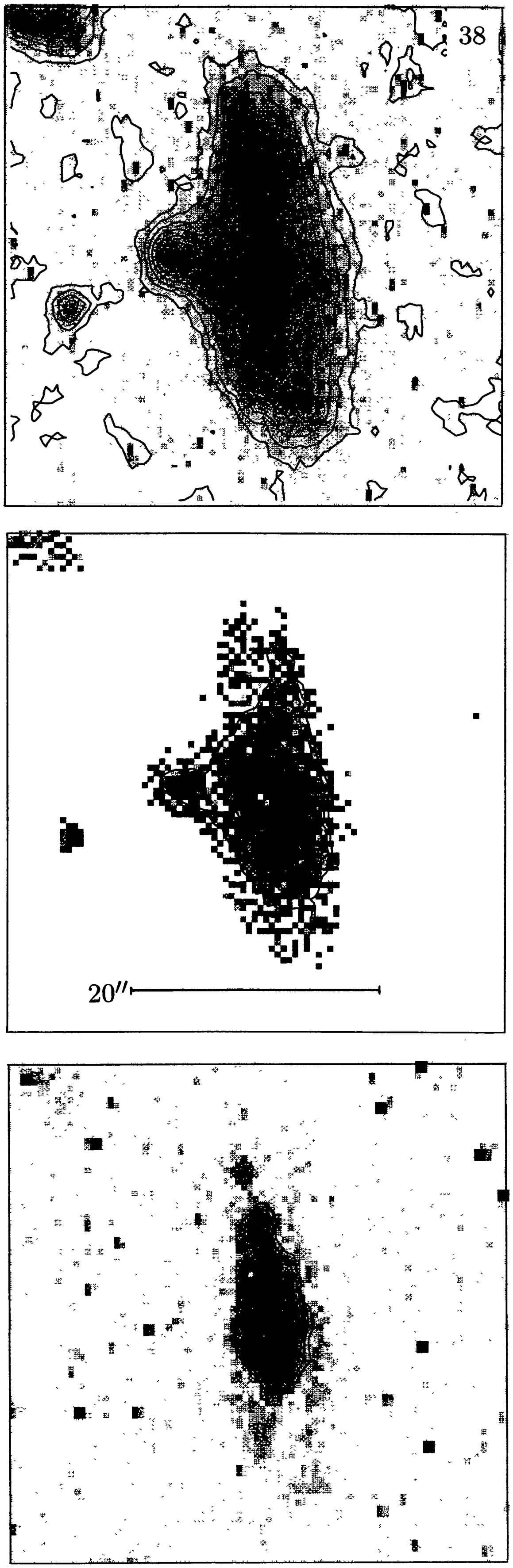

FIGURE 49. Field I: No. 38. B(top): 25.0(0.5)21.5; $B-R$(middle): 1.1(0.2)1.9; Hα(bottom): $-18.5(0.2)-17.5$

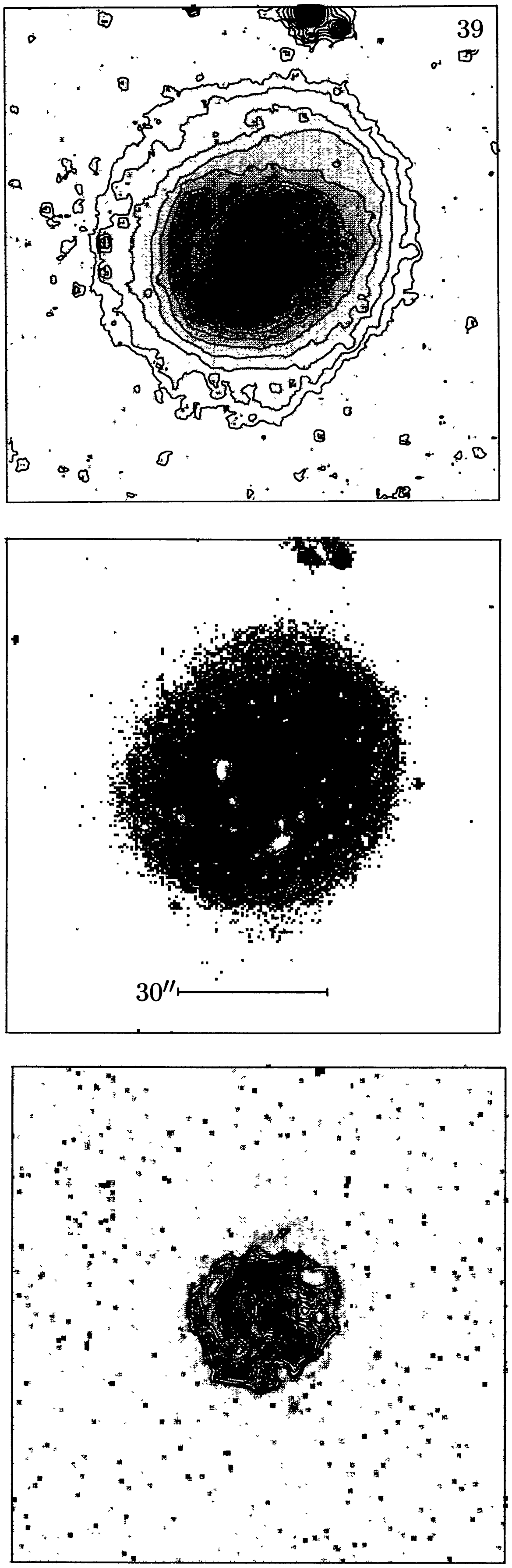

FIGURE 50. Field I: No. 39. B(top): 25.0(0.5)20.0; $B-R$(middle): 1.1(0.2)1.7; Hα(bottom): $-18.5(0.2)-17.3$

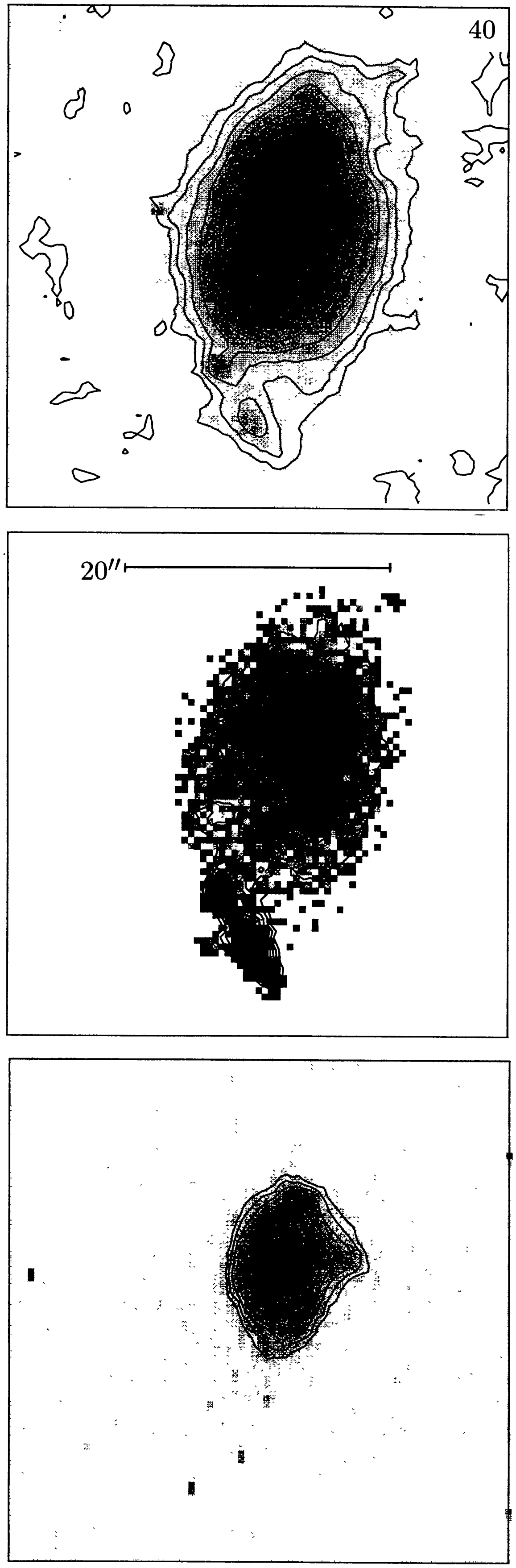

FIGURE 51. Field I: No. 40. B(top): 25.0(0.5)20.5; $B-R$(middle): 1.0(0.2)1.8; Hα(bottom): $-18.5(0.2)-17.1$

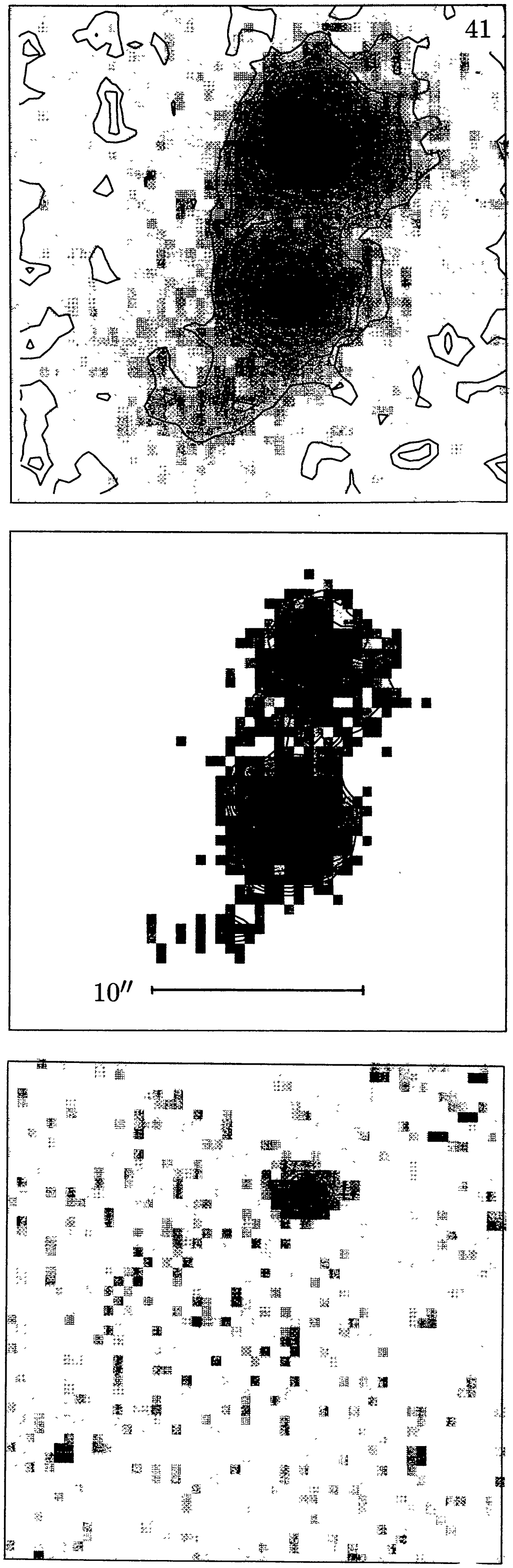

FIGURE 52. Field I: No. 41. B(top): 25.0(0.5)22.0; $B-R$(middle): 1.3(0.2)2.1; Hα(bottom): $-18.5(0.2)-17.9$

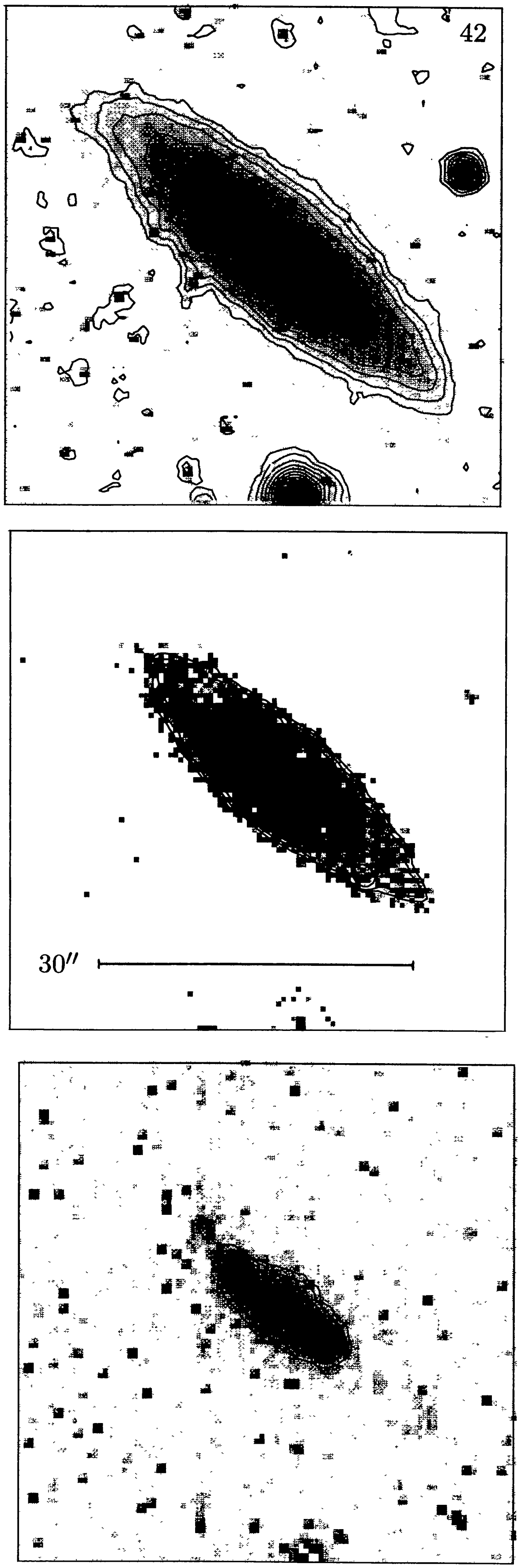

FIGURE 53. Field I: No. 42. B(top): 25.0(0.5)21.0; $B-R$(middle): 0.9(0.2)1.9; Hα(bottom): $-18.5(0.2)-17.5$

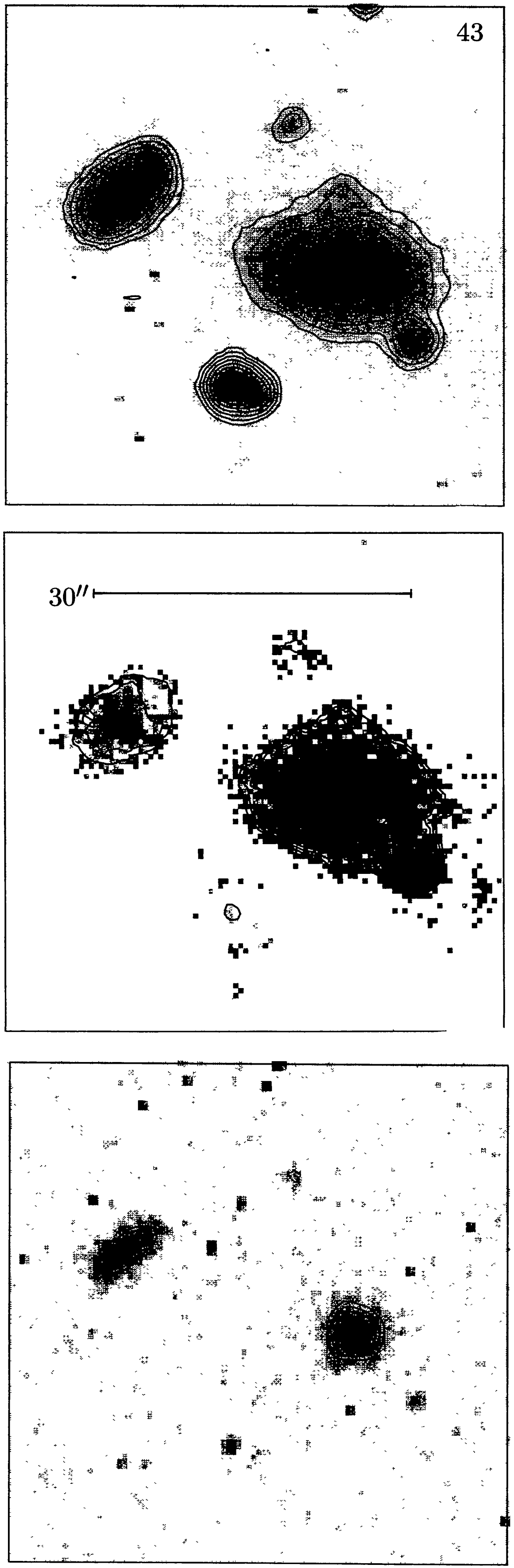

FIGURE 54. Field II: No. 43. B(top): 24.5(0.5)22.0; $B-R$(middle): 1.2(0.2)2.0; Hα(bottom): $-18.5(0.2)-17.7$

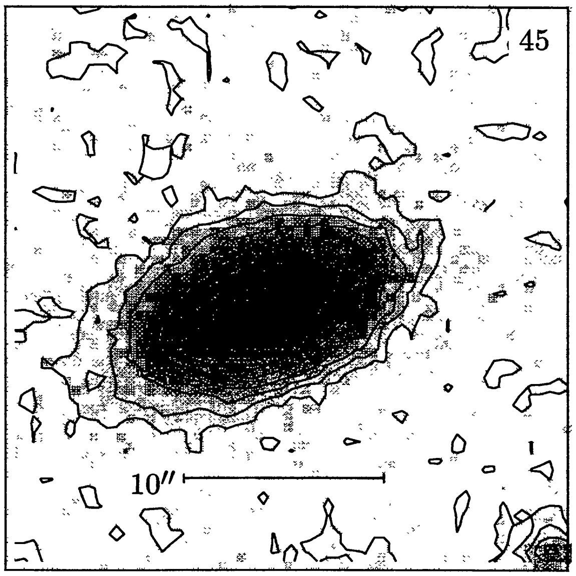

FIGURE 55. Field II: No. 45. B: 25.0(0.5)21.0 Only $B-$band image available.

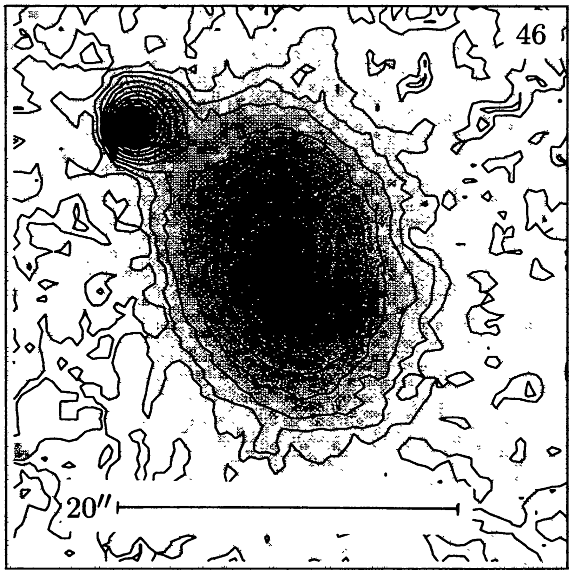

FIGURE 56. Field II: No. 46. B: 25.0(0.5)21.0 Only $B-$band image available.

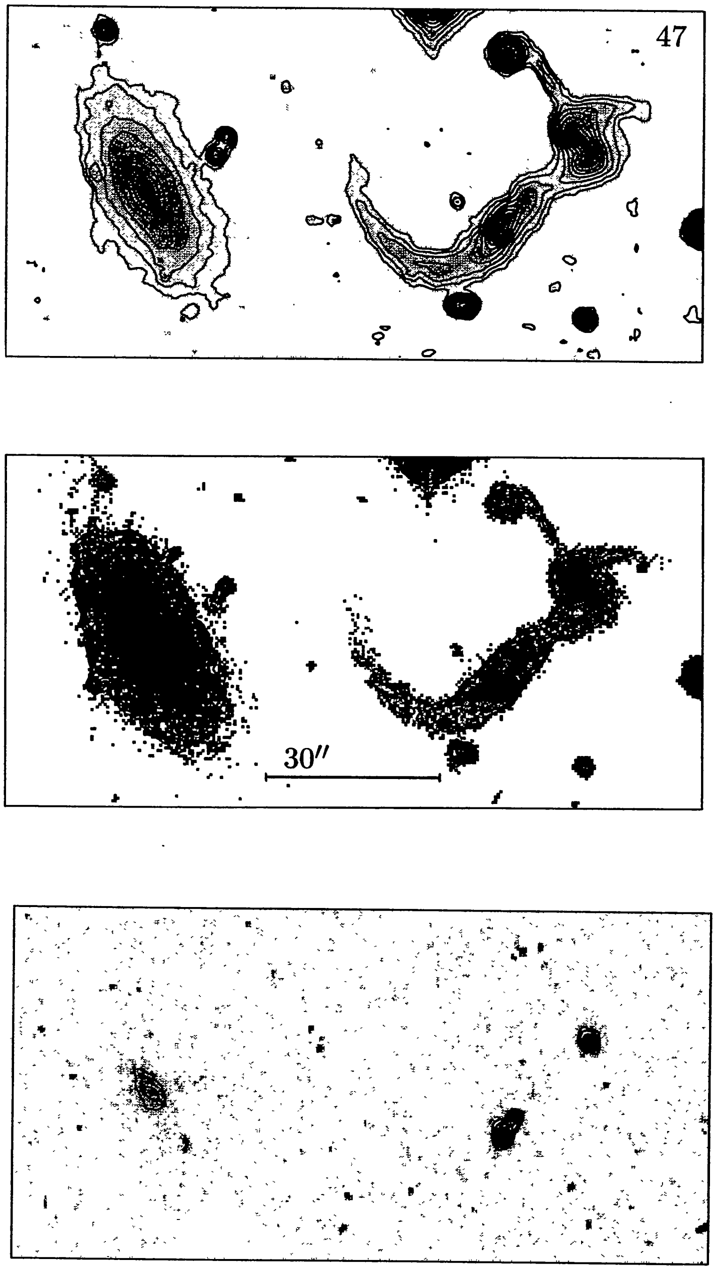

FIGURE 57. Field II: No. 47. B(top): 25.0(0.5)21.0; $B-R$(middle): 0.9(0.2)1.9; Hα(bottom): $-18.5(0.3)-17.6$

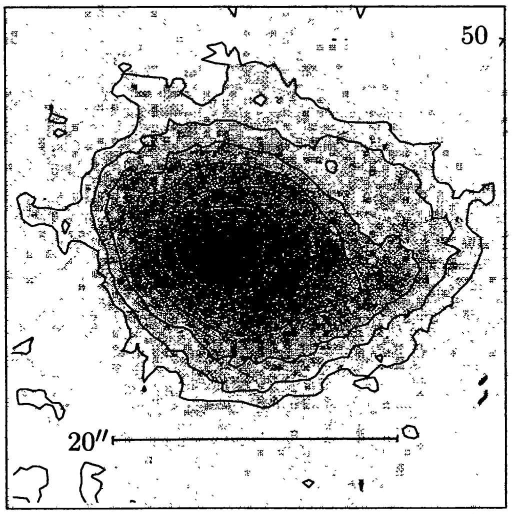

FIGURE 58. Field II: No. 50. B: 24.5(0.5)21.5 Only $B-$band image available.

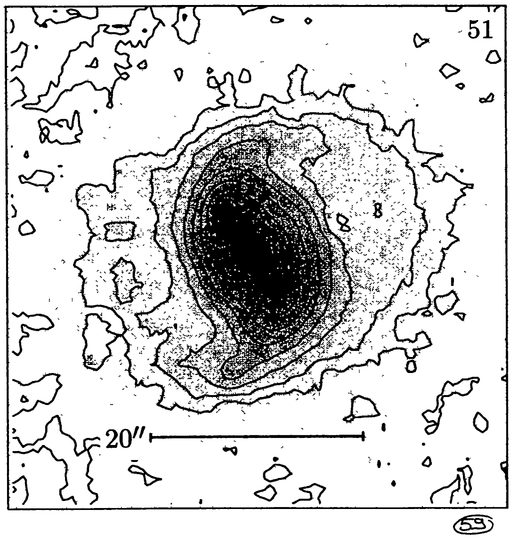

FIGURE 59. Field II: No. 51. B: 25.0(0.5)20.0 Only $B-$band image available.

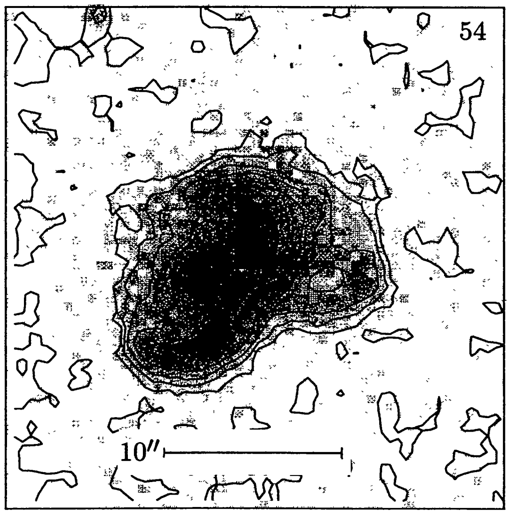

FIGURE 60. Field II: No. 54. B: 24.5(0.5)21.5 Only $B-$band image available.

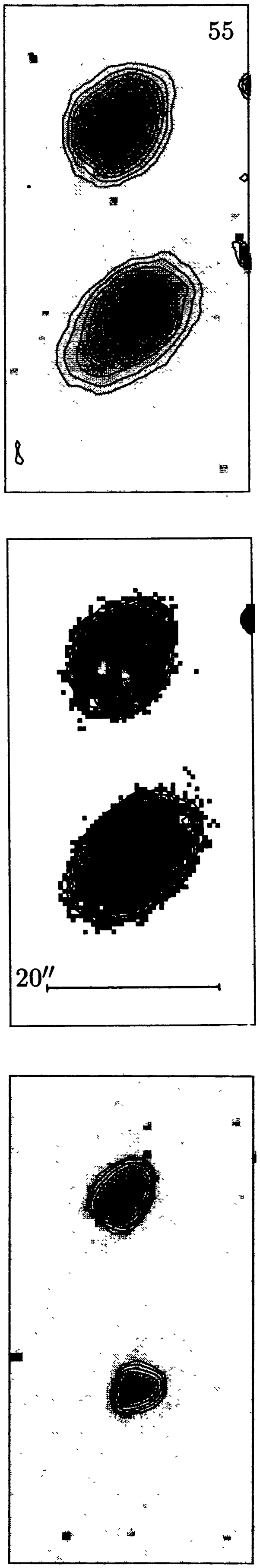

FIGURE 61. Field II: No. 55. B(top): 25.0(0.5)21.0; $B-R$(middle): 1.0(0.2)1.8; Hα(bottom): −18.5(0.2)−17.3

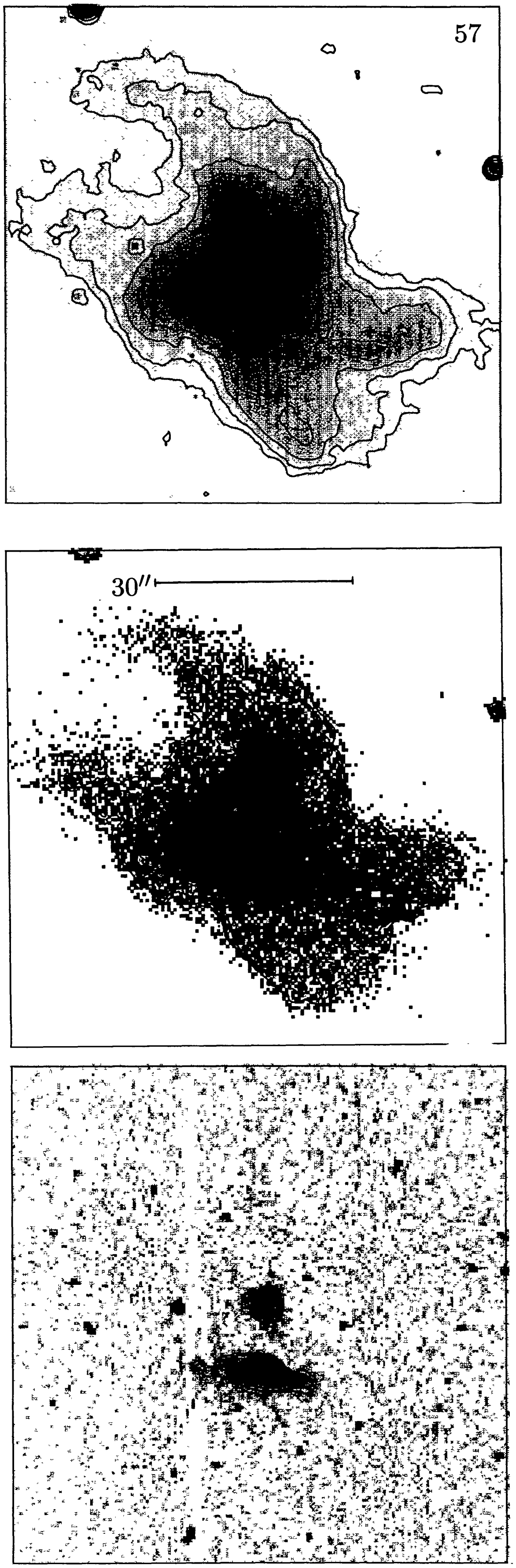

FIGURE 62. Field II: No. 57. B(top): 25.0(0.5)21.0; $B-R$(middle): 0.8(0.2)1.6; Hα(bottom): $-18.5(0.2)-17.5$

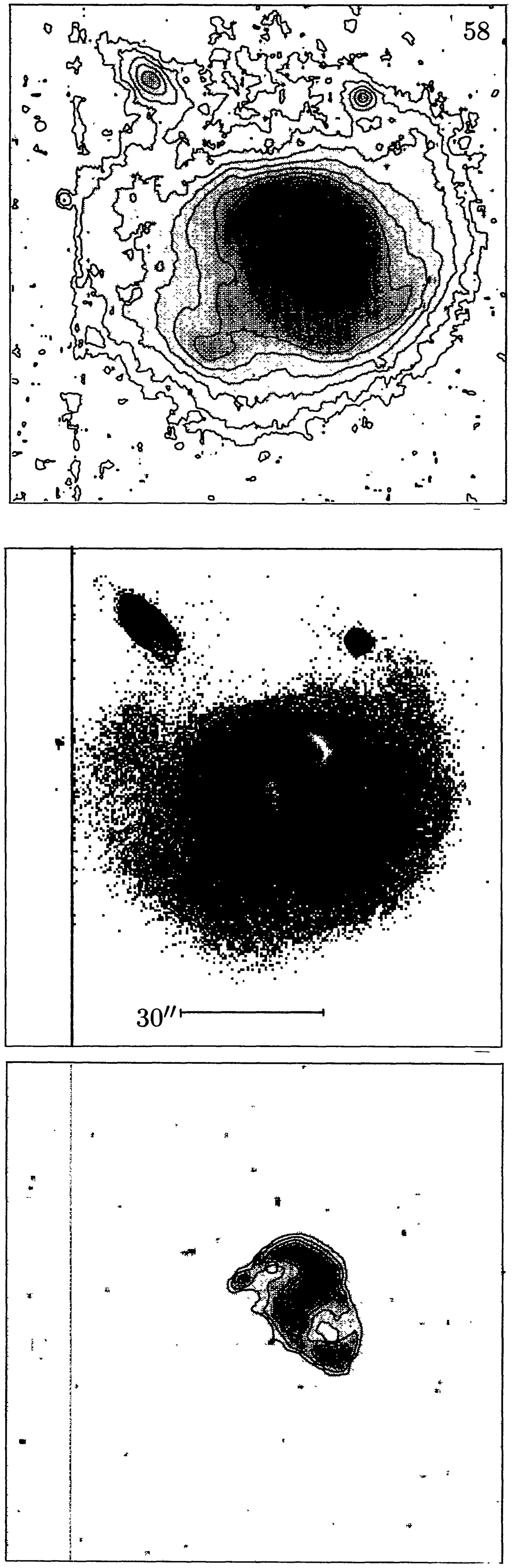

FIGURE 63. Field II: No. 58. B(top): 25.0(0.5)18.5; $B-R$(middle): 0.8(0.2)1.8; Hα(bottom): $-18.5(0.3)-16.4$

1991A&AS...91...61V

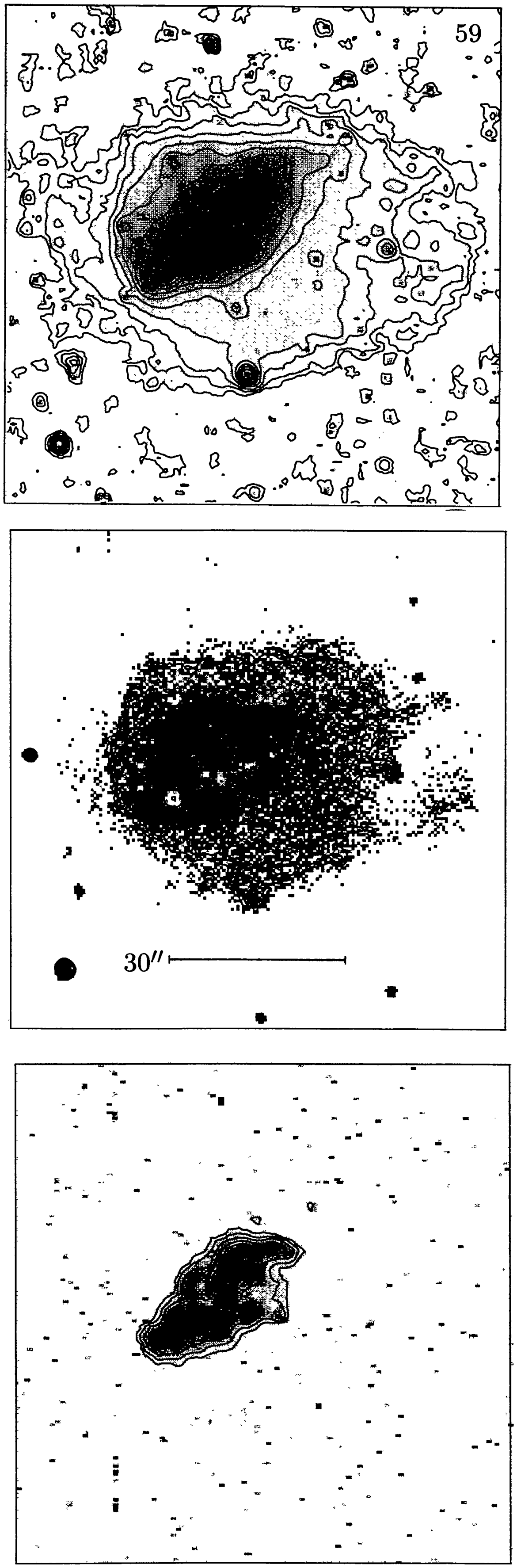

FIGURE 64. Miscellaneous: No. 59. B(top): 25.0(0.5)18.5; $B-R$ (middle): 0.7(0.15)1.0; Hα(bottom): $-18.5(0.3)-17.0$

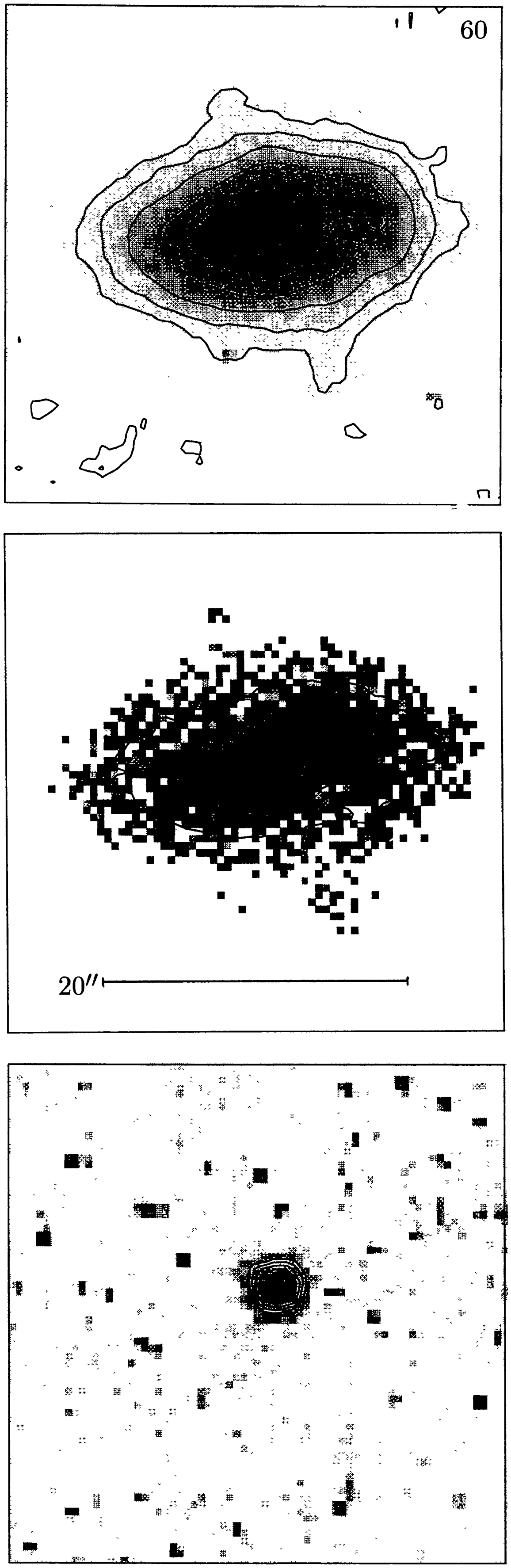

FIGURE 65. Miscellaneous: No. 60. B(top): 25.0(0.5)21.0; $B-R$(middle): 1.6(0.2)2.2; Hα(bottom): $-18.5(0.2)-17.7$

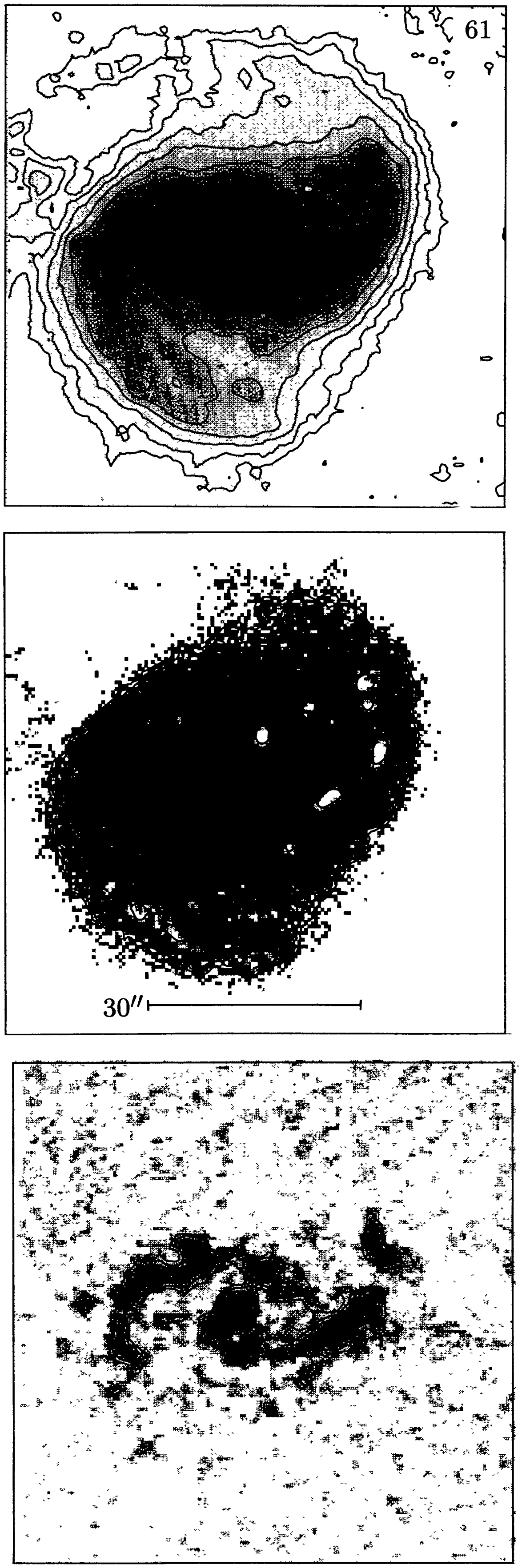

FIGURE 66. Miscellaneous: No. 61. B(top): 25.0(0.5)19.5; $B-R$(middle): 0.8(0.2)1.6; Hα(bottom): $-18.5(0.2)-17.5$

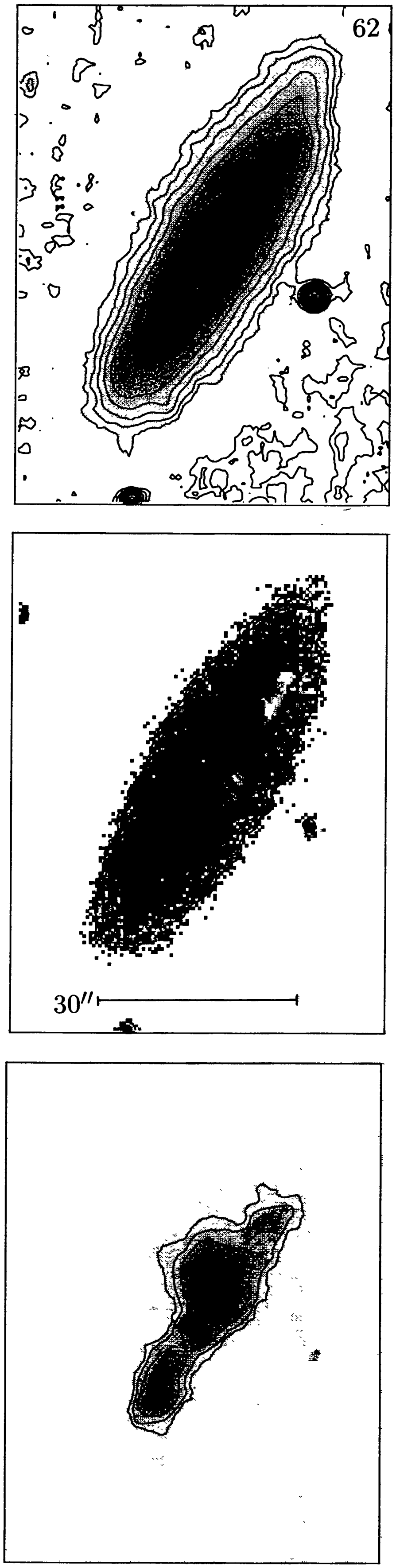

FIGURE 67. Miscellaneous: No. 62. B(top): 25.0(0.5)20.0; $B-R$(middle): 0.8(0.2)1.6; Hα(bottom): $-18.5(0.3)-16.4$